Epitaxial graphene nanodevices and their applications for electronic and magnetic sensing

Vishal Panchal

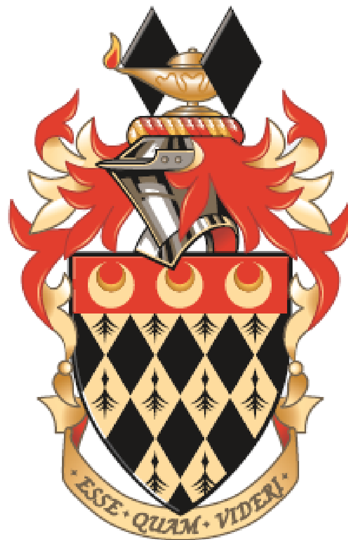

Department of Physics

Royal Holloway, University of London

A thesis for the degree of Doctor of Philosophy

04th March 2014

Declaration of Authorship

I Vishal Panchal hereby declare that this thesis and the work presented in it is entirely my own. Where I have consulted the work of others, this is always clearly stated.

Signed: ....

Date: ....

Abstract

Epitaxial graphene (EG) on SiC is readily compatible with CMOS processes and holds great potential for wafer scale production of devices. My aim is to understand the electronic properties of EG using bulk transport and nanoscale mapping techniques.

It is shown that miniaturisation of single-layer graphene (1LG) devices even down to $100\,nm$ does not significantly change the superior electronic properties of the material. However, unoptimised device geometry results in an increase of $1/f$ noise, significantly affecting the magnetic field sensitivity of devices. Detection of small magnetic moment reveals that EG devices still outperform conventional semiconductor devices.

To study the nanoscale properties of EG, a comparison of amplitude- and frequency-modulated Kelvin probe force microscopy and electrostatic force spectroscopy is carried out. The most accurate of these techniques are used for non-contact measurements of the various properties of EG. In addition, the local electrical and magnetic gating effects are also investigated using scanning gate microscopy (SGM). Work function measurements reveal that patches of double-layer graphene (2LG) exhibit a significantly higher carrier density, affecting the conductivity and sensitivity of devices. Furthermore, electric field screening is measured in 2LG devices using SGM. A carrier inversion is observed at lithographically defined edges of devices, which could be further enhanced with lateral gates. Resists and chemicals used throughout the fabrication process are shown to affect the carrier type in the most extreme cases and was used to create a unique planar p-n junction. Changes in the ambient air can lead to further doping effects, which are reversed in vacuum.

Novelty of this work is in the combination of bulk transport and local nanoscale work function mapping techniques, which led to a deeper understanding of the unique electronic properties of EG.

Table of Contents

Acknowledgements **7**

List of Publications **8**

List of Figures **10**

List of Tables **14**

List of Abbreviations **15**

List of Symbols **17**

1 Introduction **19**

2 Graphene: theory, growth and characterisation **23**

2.1 Band structure 23

2.1.1 Single-layer graphene 23

2.1.2 Double-layer graphene 26

2.2 Mechanical exfoliation 27

2.3 Chemical vapour deposition 28

2.4 Epitaxial growth on SiC 28

2.4.1 Growth of graphene on SiC(0001) 29

2.4.2 Effect of wafer miscut angle 30

2.4.3 Layer uniformity 31

2.4.4 Influence of environmental conditions 32

2.4.5 Advantages and disadvantages 32

2.5 Raman spectroscopy 33

2.5.1 Phonon dispersion . . . 33
2.5.2 Raman spectra of graphene . . . 34
2.5.2.1 Exfoliated graphene . . . 34
2.5.2.2 Epitaxial graphene on SiC . . . 35
2.5.3 Raman mapping . . . 37
2.6 Surface potential mapping . . . 38
2.6.1 Identifying graphene thickness domains . . . 38
2.6.2 Contact resistance . . . 40
2.7 Summary . . . 41

3 Bulk electronic properties of Hall sensors 42
3.1 Classical Hall effect . . . 43
3.2 Transport properties of nominally 1LG devices . . . 43
3.3 Noise mechanisms . . . 47
3.4 A comparison with semiconductor devices . . . 50
3.5 Single magnetic bead detection . . . 51
3.5.1 Placement of a single Dynal bead . . . 52
3.5.2 Experimental method . . . 53
3.5.3 Bead detection . . . 53
3.6 Summary . . . 55

4 Scanning probe microscopy techniques for nanoscale investigations 57
4.1 Atomic force microscopy . . . 58
4.2 Electrostatic force microscopy . . . 59
4.3 Surface potential measurements . . . 60
4.3.1 Electrostatic force spectroscopy . . . 60
4.3.2 Amplitude-modulated Kelvin probe force microscopy . . . 62
4.3.3 Frequency-modulated Kelvin probe force microscopy . . . 64
4.4 Electrical and magnetic scanning gate techniques . . . 65

5 Nanoscale mapping of devices 67
5.1 Nanoscale mapping with SPM techniques . . . 67
5.2 Accuracy of the surface potential measurements . . . 71

5.3 Contactless resistance measurements 72
5.4 Effects of environmental doping on 1LG 74
5.4.1 UV exposed photochemicals 75
5.4.2 Controlled environment 77
5.5 Work function of 1LG and 2LG 80
5.6 Effects of 2LG islands on transport properties 82
5.7 Edge effects 83
5.8 Summary 85

6 Electrical and magnetic gating 88

6.1 Electrical lateral gates 89
6.1.1 Nanoscale visualisation of the gating effect 89
6.1.2 Gating effect quantified on nanoscale 91
6.1.3 Gating effect on bulk electronic properties 92
6.1.4 Leakage current 93
6.2 Electrical scanning gate 94
6.2.1 Electrostatic effects in uniform 1LG and 2LG devices 95
6.2.2 Electrostatic effects of 2LG islands on 1LG device 97
6.2.2.1 Effects on channel resistance 97
6.2.2.2 Effects on transverse voltage 100
6.3 Magnetic scanning gate 102
6.3.1 Elimination of electrostatic effects 102
6.3.2 Magnetic response of uniform 1LG device 104
6.4 Summary 106

7 Conclusion and future outlook 109

Appendix A - Fabrication 115

Appendix B - Bead-sensor coupling 117

Appendix C - Atomic force microscopy cleaning 118

Bibliography 119

Acknowledgements

I first want to give a *Vishal* thanks to Olga and James, who have been absolute delight supervisors, knowing exactly how to bring out the best in me. Olga will continue to inspire me with her admirable work ethics and James with his enthusiasm for getting things done on time.

I also want to give a *Grand* thanks to Alexander Tzalenchuk, John Gallop, Tim Burnett, Cristina Giusca, Ruth Pierce, Malcolm Connolly and Masaya Kataoka, for all their scientific help. Without them, I would still be glued to Wikipedia pages, trying to make sense of the physics.

I also want to give a *Huge* thanks to Jon Fletcher, Sergiy Rozhko, David Cox, Andrés Muñiz Piniella, Steve Giblin, Patrick See and Patrick Josephs-Franks, for their technical help with experimental techniques, instrumentation and devices. Without them, I would still be locked in the lab, trying to make sense of the experiments.

I also want to give a *Big* thanks to Sergey Kubatkin, Karin Cedergren, Arseniy Lartsev, Thomas Yager and Samuel Lara-Avila, for their help with fabrication. Without them, I would still be in the cleanroom endlessly spinning PMMA and ZEP.

I also want to give a *General* thanks to my fellow students Jon, Ravish, Viktoria, Tom, Hector and Ilana for their discussions and distractions.

I also want to give a *Unique* thanks to Armin van Buuren, for putting me in A State of Trance, allowing me to write this entire thesis.

I also want to give a *Special* thanks to my cousin Janki Mistry, for making me her biggest role model and pushing me far beyond my limits.

I finally want to give a *Loving* thanks to Bharat and Sangita, for bringing me into this very interesting universe, giving me the ethics, the foundation, the tools and most importantly the love to succeed in life. Without them, I simply wouldn't be here.

List of Publications

First author

1. **Small epitaxial graphene devices for magnetosensing applications.** V. Panchal, K. Cedergren, R. Yakimova, A. Tzalenchuk, S. Kubatkin, O. Kazakova. *Journal of Applied Physics*, 111, 07E509, 2012. DOI:10.1063/1.3677769

2. **Surface potential variations in epitaxial graphene devices investigated by Electrostatic Force Spectroscopy.** V. Panchal, T. L. Burnett, R. Pearce, K. Cedergren, R. Yakimova, A. Tzalenchuk, O. Kazakova. *12th IEEE Conference on Nanotechnology (IEEE-NANO)*, 1–5, 2012. DOI:10.1109/NANO.2012.6322049

3. **Epitaxial graphene sensors for detection of small magnetic moments.** V. Panchal, D. Cox, R. Yakimova, O. Kazakova. *IEEE Transactions on Magnetics*, 49, 1, 2013. DOI:10.1109/TMAG.2012.2218277

4. **Magnetic scanning probe calibration using graphene Hall sensor.** V. Panchal, Ó. Iglesias-Freire, A. Lartsev, R. Yakimova, A. Asenjo, O. Kazakova. *IEEE Transactions on Magnetics*, 49, 7, 2013. DOI:10.1109/TMAG.2013.2243127

5. **Standardization of surface potential measurements of graphene domains.** V. Panchal, R. Pearce, R. Yakimova, A. Tzalenchuk, O. Kazakova. *Scientific Reports*, 3, 2597, 2013. DOI:10.1038/srep02597

6. **Local electric field screening in bi-layer graphene devices.** V. Panchal, C. E. Giusca, A. Lartsev, R. Yakimova and O. Kazakova. *Frontiers in Physics*, 2, 3, 2014. DOI:10.3389/fphy.2014.00003

7. **Visualization of edge effects in graphene nanodevices.** V. Panchal, T. L. Burnett, A. Lartsev, A. Manzin, R. Yakimova, A. Tzalenchuk and O. Kazakova. To be submitted, 2014.

Co-author

1. **Epitaxial graphene and graphene-based devices studied by electrical scanning probe microscopy.** O. Kazakova, V. Panchal, T. L. Burnett. *Crystals*, 3(1), 191-233, 2013. DOI:10.3390/cryst3010191

2. **Express optical analysis of epitaxial graphene on SiC: impact of morphology on quantum transport.** T. Yager, A. Lartsev, S. Mahashabde, S. Charpentier, D. Davidovikj, A. Danilov, R. Yakimova, V. Panchal, O. Kazakova, A. Tzalenchuk, S. Lara-Avila, S. Kubatkin. *Nano Letters*, 13, 4217-4223, 2013. DOI:10.1021/nl402347g

3. **Magnetic scanning gate microscopy of graphene Hall devices.** R. K. Rajkumar, A. Asenjo, V. Panchal, A. Manzin, Ó. Iglesias-Freire, O. Kazakova. *Journal of Applied Physics*, In press, 2014.

List of Figures

2.1 Graphene lattice structure and the Brillouin zone in the momentum space. 24

2.2 The full electronic dispersion of single-layer graphene. 25

2.3 Stacking and electronic dispersion of double-layer graphene near the Dirac point. 26

2.4 Schematic structure for single- and double-layer epitaxial graphene. . . 29

2.5 A schematic showing a $4H$-SiC substrate that is on-axis and with a miscut. 30

2.6 A schematic showing continuous graphene over terrace step edges. . . . 31

2.7 Phonon dispersion of graphene from density functional theory calculations. 34

2.8 Raman spectra for single-layer and folded single-layer graphene. 34

2.9 Raman spectra for epitaxial graphene on SiC. 35

2.10 Raman spectra for epitaxially grown graphene on SiC that was transferred to Si/SiO_2. 36

2.11 Raman mapping of a few-layer graphene flake. 38

2.12 Topography image of few graphene layers on Si/SiO_2 and surface potential mapping of epitaxial graphene on $6H$-SiC(0001). 39

2.13 Work function of single- and double-layer graphene as a function of back gate voltage 40

2.14 Surface potential mapping to determine the contact resistance between graphene and metal electrode 40

3.1 Images of the transport properties measurement setup, magnetic field dependence of the Hall voltage and cross size dependence of the Hall coefficient. 44

3.2 Plot showing cross size dependences of sheet resistance and carrier mobility. 45

3.3 Plot showing the relation of the carrier density against carrier mobility and cross size dependence of the mean free path. 46
3.4 Plot showing the frequency dependence of the noise spectral density and cross size dependence of the voltage lead resistance, white noise, $1/f$ corner and minimum detectable field. 48
3.5 Device geometry optimisation for lower $1/f$ noise. 49
3.6 Compilation of carrier density and carrier mobility for epitaxial graphene, InSb and GaAs devices. 51
3.7 Scanning electron micrograph of a puddles of Dynal MyOne beads and device with a bead placed on a Hall cross. 52
3.8 Bead detection experimental setup. 53
3.9 Phase sensitive AC/DC measurement showing the detection of a single Dynal bead. 54

4.1 Plot showing the phase shift and amplitude of the cantilever relative to the drive signal 58
4.2 A schematic of the electrostatic force microscopy experimental setup . . 59
4.3 A schematic of the probe-sample electrostatic force 60
4.4 Energy level scheme for the sample and PFQNE-AL probe, a typical electrostatic force spectroscopy curve and binding energy curve for Au. 61
4.5 A schematic of the amplitude-modulated Kelvin probe force microscopy experimental setup. 63
4.6 A schematic of the frequency-modulated Kelvin probe force microscopy experimental setup. 64
4.7 A schematic of the scanning gate microscopy experimental setup operating with field and field gradient. 66

5.1 AFM, EFM, AM-KPFM and FM-KPFM mapping of a $4.8\mu m$ wide epitaxial graphene device. 68
5.2 Surface potential measurement of single- and double-layer graphene with electrostatic force microscopy and spectroscopy. 69

5.3 Surface potential measurement of single- and double-layer graphene with AM-KPFM and FM-KPFM. 70
5.4 Line profiles of the surface potential measured along a current biased epitaxial graphene device using EFS, AM-KPFM and FM-KPFM. . . . 72
5.5 Normalised line profiles of the surface potential measured along an operating epitaxial graphene device and I-V_{ch} curve to determine the resistance of graphene channel and Au-graphene contacts. 73
5.6 Topography of a device showing thickness of resist residues and schematic of 1LG band structure showing the doping levels. 75
5.7 Electron-beam irradiation effects on resist residue doping. 77
5.8 Topography, surface potential and work function of a planar p-n junction. 78
5.9 Carrier density of graphene in different environments. 79
5.10 Work function measurements of single- and double-layer graphene. . . . 81
5.11 Schematic structure for single- and double-layer epitaxial graphene showing doping and interlayer interactions. 82
5.12 Plot showing the dependence of 4-terminal resistance and carrier density on the percentage of double-layer graphene present on single-layer graphene devices. 82
5.13 Topography and surface potential maps showing edge effects. 83
5.14 EFS measurements performed at the centre and edge of lithographically defined graphene to investigate edge effects. 84

6.1 Topography and surface potential images of a 910 nm wide device. . . . 90
6.2 Lateral gating effect on the work function and carrier density. 91
6.3 Lateral gating effect on channel resistance and conductance. 92
6.4 Lateral gating effect on carrier density. 93
6.5 The dependence of the leakage current on the lateral gate voltage. . . . 94
6.6 Electric field gradient scanning gate microscopy on uniform 1LG and 2LG devices. 95
6.7 Electrical field gradient scanning gate microscopy on non-uniform EG device. 97
6.8 Electrical field scanning gate microscopy on non-uniform EG device. . . 99

6.9 Electric field gradient scanning gate microscopy on non-uniform EG device. 100
6.10 Schematics of the current distribution in locally gated Hall sensors. . . 101
6.11 Line profiles of the electric field gradient scanning gate microscopy and EFM image of non-uniform EG device. 101
6.12 Topography, surface potential and transverse voltage response of a 1LG device to electric and magnetic stray fields. 103
6.13 A schematic of the magnetic field gradient measurement setup. 104
6.14 Transverse voltage response of a device to magnetic field gradient. . . . 105

A.1 Optical images of an EG sample. 116
B.1 Scanning electron micrograph of a device with a bead placed on a Hall cross. 117
C.1 Contact-mode AFM Cleaning. 118

List of Tables

3.1 A summary of data for EG, InSb and CVD graphene devices. 50

4.1 A summary of the SPM probes used throughout the thesis. 57

5.1 A summary of the effects of resist residues, substrate and environmental doping on epitaxial graphene. 76

5.2 A summary of the transport properties for p-n junction. 78

5.3 A summary of the work function differences between single- and double-layer graphene. 81

6.1 A summary of measurements obtained with electric field and electric field gradient SGS techniques. 98

6.2 A summary of the maximum transverse voltage response to MESP and MESP-HM probes. 106

A.1 A summary of EG devices used throughout the thesis. 116

List of Abbreviations

1LG	Single-Layer Graphene
2LG	Double-Layer Graphene
3LG	Triple-Layer Graphene
AC	Alternating Current
AFM	Atomic Force Microscope
AM	Amplitude-Modulated
BZ	Brillouin Zone
CM	Contact-Mode
CPD	Contact Potential Difference
CVD	Chemical Vapour Deposition
DC	Direct Current
EBL	Electron Beam Lithography
EFM	Electrostatic Force Microscopy
EFS	Electrostatic Force Spectroscopy
EG	Epitaxial Graphene
FIB	Focused Ion Beam
FM	Frequency-Modulated
FWHM	Full Width at Half-Maximum
GR	Generation-Recombination
HOPG	Highly Ordered Pyrolytic Graphite
IFL	InterFacial-Layer
IPA	IsoPropyl Alcohol
KPFM	Kelvin Probe Force Microscopy
MFM	Magnetic Force Microscopy
MMA	Methyl MethAcryllate

PMMA	Poly(Methyl MethAcrylate)
ppb	parts-per-billion
PSD	Position Sensitive Detector
QHE	Quantum Hall Effect
SGM	Scanning Gate Microscopy
SGS	Scanning Gate Spectroscopy
SP	Surface Potential
SPM	Scanning Probe Microscopy
TLM	Transmission Line Method
UHV	Ultra-High Vacuum
UPS	Ultraviolet Photoelectron Spectroscopy
UV	UltraViolet

List of Symbols

A_{osc}	Cantilever oscillation amplitude
B_{AC} (B_{DC})	AC (DC) magnetic field
B_{min}	Minimum detectable magnetic field
B_{probe}	Magnetic probe stray field
C	Capacitance
c	Bead-sensor coupling
E	Electric field
E_F	Fermi energy
e	Electronic charge
F	Electrostatic force
f	Frequency
G	Conductance
I	Current
I_{bias}	Device bias current
L	Inductance
m	Magnetisation
n_e (n_h)	Electron (hole) carrier density
R_2 (R_4)	2- (4-) terminal resistance
R_H	Hall coefficient (+ for n-type, − for p-type)
R_s	Sheet resistance
S_{VT}	Johnson-Nyquist noise
V_{ch}	DC channel bias voltage
V_{CPD}	Contact potential difference
V_g	Lateral gate voltage
V_{mod}	Probe AC probe voltage

V_{probe}	Probe DC bias voltage
V_{xx}	Longitudinal voltage
V_{xy} (V_H)	Transverse (Hall) voltage
V^{AC}	AC voltage
V_x^{AC} (V_y^{AC})	In-phase (out-of-phase) component of AC voltage
λ	Mean free path
μ_B	Bohr magneton
μ_e (μ_h)	Electron (hole) carrier mobility
ν_F	Fermi velocity
Φ	Work function
φ	Cantilever phase
χ	Magnetic susceptibility

Chapter 1

Introduction

In the fast evolving modern world, the need for ever faster, cheaper and more energy efficient consumer electronics has pushed scientists and industry to invest vast amount of resources forming the semiconductor industry. Moore's Law has been closely followed since 1971. Inevitably, it will soon breakdown as manufacturers continue to push the limits of fabrication producing ever smaller devices. This has lead scientists and industry worldwide to find an alternative material that can outperform silicon and breaking away from the silicon age.

Sir Andre Geim and Sir Konstantin Novoselov were awarded The Nobel Prize in Physics 2010 "*for groundbreaking experiments regarding the two-dimensional material graphene*" [1]. Their electric field effect experiments in atomically thin carbon films [2] (now known as graphene) revealed to the world, that graphene has potential applications for metallic transistors that are smaller, more energy efficient and operate at higher frequencies. Graphene offers ballistic transport, linear current-voltage characteristics and excellent conductivity ($> 10^8\ A/cm$) [2]. In addition to these extraordinary transport properties, graphene is a truly 2D material, where each carbon atom is covalently bonded to three other carbon atoms to produce an atomically flat honeycomb crystal lattice. Although graphene was only recently discovered, the band structure and Brillouin zone of graphene was theorised in the late 1940's by P. R Wallace using the tight-binding approximation [3].

The Manchester group demonstrated amazing transport properties in graphene flakes obtained from highly ordered pyrolytic graphite (HOPG) via mechanical ex-

foliation using Scotch tape [4]. Although this technique still produces graphene of the highest quality, it is not the most viable technique for large scale production to kick-start the graphene age. Graphene grown by chemical vapour deposition (CVD) on transition metal films is of high quality. However, it must be transferred onto an insulating substrate, requiring chemical and mechanical processes that can potentially damage the film. Epitaxial graphene (EG) on Silicon Carbide (SiC) substrate can be patterned in its as grown state due to the insulating nature of the substrate. However, growth on the Si-face of SiC(0001) tends to be patchy with islands of multiple graphene layers and is closely following the complex topography of the substrate. Moreover, graphene on SiC(0001) is subject to heavy n-doping from a carbon layer that is covalently bonded to the substrate, typically referred to as the buffer- or interfacial-layer (IFL). The growth mechanism of graphene on the C-face of SiC(000-1) is not subject to the IFL, however graphene forms quickly and wildly, making it extremely difficult for controlled uniform growth. In order for graphene to be commercially viable, the electronic properties of single- and double-layer graphene (1LG and 2LG, respectively) need to be fully understood. The primary focus of this thesis is to correlate bulk transport with local electronic properties of EG nanodevices, using various scanning probe microscopy (SPM) techniques, to obtain a full understanding and to demonstrate their potential for electronic and magnetic sensing applications.

Chapter 2 provides a literature review on the theory of 1LG and 2LG band structure. As the primary focus of this thesis is on EG, a review has been provided for the SiC(0001) growth process, common characteristics of EG, the influence of environmental doping and the advantages and disadvantages of EG. A review of Raman spectroscopy is equally important as it is widely regarded as the definitive method of identifying the graphene layer thicknesses. The use of electrical force microscopies in studies of electronic properties of graphene is increasingly becoming common due to its ease of access and nanometre scale spatial resolution. Review on layer identification, work function and contact resistance measurements on devices using SPM techniques are also provided.

Chapter 3 discusses the investigations of miniaturising Hall devices from 0.1-19.6μm fabricated out of nominally 1LG on $4H$-SiC(0001). The effects of fabrication induced de-

fects and miniaturisation have been studied by investigating the carrier density (n), carrier mobility (μ), Hall coefficient (R_H) and minimum detectable magnetic field (B_{min}) at room temperature, in ambient air, using transport and noise spectrum measurements. The performance of these devices are compared to that of devices fabricated out of state-of-the-art semiconductor and CVD graphene. Furthermore, the stray magnetic field emanating from a single $1\,\mu m$ diameter magnetic particle was detected using AC/DC Hall magnetometry. The result of this experiment was also compared to findings from identical measurements carried out on InSb epilayer devices of similar size and geometry, providing a clear demonstration of the advantages of graphene.

While transport measurements provide a measure of the bulk electronic properties, SPM techniques provide a map of nanoscale electronic properties. Chapter 4 discusses the atomic force microscopy (AFM) based mapping techniques used throughout this thesis to study the nanoscale electronic properties of EG devices. These include mapping of the topography, surface potential, and device response to a local electrical/magnetic scanning gate. Chapter 5 discusses the nanoscale mapping of the electronic properties of EG devices. The three most widely used surface potential measurement techniques are electrostatic force spectroscopy (EFS), amplitude-modulated (AM-) and frequency-modulated (FM-) Kelvin probe force microscopy (KPFM). However, each technique can provide contradicting results, therefore a comprehensive review has been carried out on a representative EG device to determine the most accurate technique. Using the most appropriate technique(s), various aspects of EG devices were studied. For example, FM-KPFM was used to study the potential drop from Au-graphene contact lead, revealing a non-Ohmic component in the contact resistance. EFS was used to study the work function of 1LG and 2LG, p-doping nature of photochemicals and n-doping nature of the IFL. The work function studies also revealed hole conduction at edges of devices that were lithographically defined using oxygen plasma etching. The effects of 2LG islands on bulk transport properties of devices were also investigated by accurately locating their positions with FM-KPFM. In most cases, the nanoscale investigations were complimented with bulk transport measurements to obtain a more detailed insight into the electronic properties of EG devices.

Chapter 6 discusses the effects of lateral electrical gates and scanning local electrical

and magnetic gates. For example, the effects of lateral gates on the surface potential distribution of the channel were studied using FM-KPFM and quantified with work function measurements. The effects of local electrical top gate on uniform and non-uniform EG devices were studied using scanning gate microscopy (SGM) and scanning gate spectroscopy (SGS). These investigations are useful in studying the electric field screening properties of isolated 2LG islands in non-uniform EG devices. The effects of local magnetic top gate on a uniform 1LG device were also investigated. Such effects can prove to be difficult to observe due to a substantial contribution from electrostatic effects. However, FM-KPFM was used *in situ* with SGM to apply a compensating voltage to the probe, such that the parasitic electric field was eliminated. This method proved extremely effective for study of the magnetic field response of EG devices.

The ultimate goal is to apply bulk and nanoscale electrical measurement techniques to EG nanodevices to obtain a more comprehensive understanding of non-uniform layer thickness devices, effects of fabrication processes, environmental doping, electrical and magnetic gating and electric field screening by 2LG. This will aid in exploiting the unique electrical properties of graphene and improve the performance of devices for electronic and magnetic sensing applications.

Chapter 2

Graphene: theory, growth and characterisation

This chapter provides a literature review on the theory of linear dispersion of 1LG and parabolic dispersion of 2LG. The chapter also discusses the three most common graphene production methods: mechanical exfoliation, chemical vapour deposition and epitaxial growth. However, as the work has been carried out on devices fabricated out of $4H$-SiC(0001), a greater emphasis has been put on epitaxially grown graphene. The literature review also covers previous studies of Raman spectroscopy and functional electrical microscopy techniques to investigate differences in the electronic properties of different layer thicknesses of graphene.

2.1 Band structure

2.1.1 Single-layer graphene

The sp^2 carbon atoms are arranged in a hexagonal (honeycomb) structure, which can be regarded as two triangular sub-lattices with each lattice consisting of two atoms per unit cell (Fig. 2.1). The 2D lattice and reciprocal-lattice vectors can be written as

$$a_1 = \frac{a}{2}\left(3, \sqrt{3}\right), \quad a_2 = \frac{a}{2}\left(3, -\sqrt{3}\right) \tag{2.1}$$

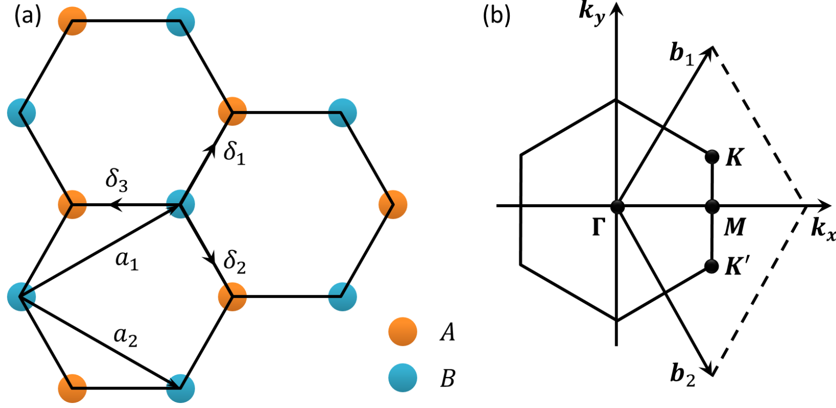

Figure 2.1: (a) Graphene honeycomb lattice structure showing the two interpenetrating triangular sublattices, where $\boldsymbol{a}_1$ and $\boldsymbol{a}_2$ are the lattice unit vectors, $\boldsymbol{\delta}_1 = \frac{a}{2}(1, \sqrt{3})$, $\boldsymbol{\delta}_2 = \frac{a}{2}(1, -\sqrt{3})$ and $\boldsymbol{\delta}_3 = -a(1, 0)$ are the three real space nearest-neighbour vectors and $\delta_1' = \pm\boldsymbol{a}_1$, $\delta_2' = \pm\boldsymbol{a}_2$ and $\delta_3' = \pm(\boldsymbol{a}_2 - \boldsymbol{a}_1)$ are the six second-nearest neighbours. The carbon atoms relating to the A and B sublattices is show using two different colours [5]. (b) Graphene Brillouin zone in the momentum space, where the Dirac cones are located in the k-space as indicated by $\boldsymbol{K}$ and $\boldsymbol{K'}$. Adapted from Ref. [5].

and

$$b_1 = \frac{2\pi}{3a}\left(1, \sqrt{3}\right), \quad b_2 = \frac{2\pi}{3a}\left(1, -\sqrt{3}\right), \tag{2.2}$$

respectively, where $a \approx 1.42$ $\mathring{A}$ is the carbon-carbon distance. Using the tight-binding approximation, P. R. Wallace realised the linear E-k relation at low energies near the corners of the Brillouin zone (BZ) at each carbon site [3]. The $\boldsymbol{K}$ and $\boldsymbol{K'}$ points of the graphene BZ in the momentum space are the points at which the cones of the electron-hole energy dispersion touch (Fig. 2.2). These positions referred to as the Dirac points, given by

$$\boldsymbol{K} = \left(\frac{2\pi}{3a}, \frac{2\pi}{3\sqrt{3}a}\right) \quad \text{and} \quad \boldsymbol{K'} = \left(\frac{2\pi}{3a}, -\frac{2\pi}{3\sqrt{3}a}\right), \tag{2.3}$$

are of significant importance in the transport properties of graphene. Wallace calculated the band structure of graphene using the tight-binding Hamiltonian for electrons in graphene hopping between the nearest-neighbour (AB) and next-nearest-neighbour (AA or BB) carbon atoms [3], which has been summarised by Neto *et al.* [5] and Das Sarma *et al.* [6]. Following from the full electronic dispersion (Fig. 2.2), the approxi-

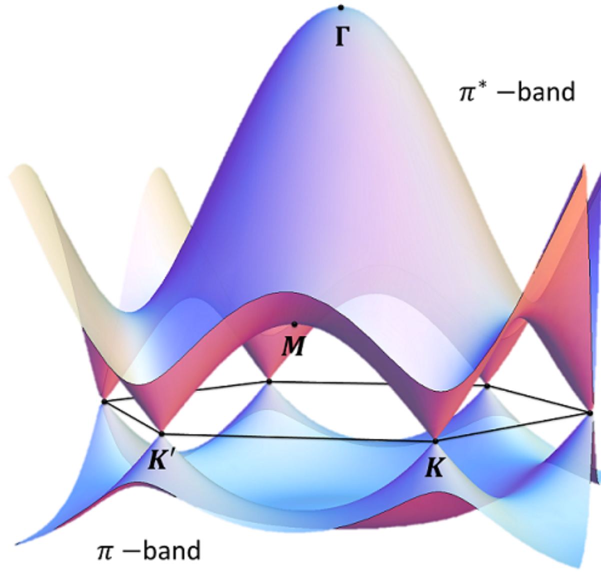

Figure 2.2: The full electronic dispersion of 1LG showing the $\boldsymbol{K}$, $\boldsymbol{K'}$, $\boldsymbol{M}$ and $\boldsymbol{\Gamma}$ points, is given by $E_{\pm}(\boldsymbol{k}) = \pm t\sqrt{3+f(\boldsymbol{k})} - t' f(\boldsymbol{k})$, where $f(\boldsymbol{k}) = 2\cos(\sqrt{3}k_y a) + 4\cos(\sqrt{3}k_y a/2)\cos(3k_x a/2)$. Adapted from Ref. [5].

mate energy for the conduction (upper, +, π^*) and valence (lower, −, π) band is given by [6]

$$E_{\pm}(q) \approx 3t' \pm \hbar\upsilon_F|\boldsymbol{q}| - \left(\frac{9t'a^2}{4} \pm \frac{3ta^2}{8}\sin 3\theta_{\boldsymbol{q}}\right)|\boldsymbol{q}|^2, \tag{2.4}$$

where $t(\approx 2.7\ eV)$ is the nearest-neighbour (*interlayer*) hopping energy, $t'(\approx -0.2t)$ is the next-nearest-neighbour (*intralayer*) hopping energy, $\upsilon_F = 3ta/2$ is the Fermi velocity, $\theta_{\boldsymbol{q}} = \arctan[q_x/q_y]$ is the angle in the momentum space and $\boldsymbol{q}$ is the momentum relative to the Dirac points. However, the position of the Dirac point is shifted due to the presence of t', thus breaking the electron-hole symmetry. At long wavelengths ($t' = 0$), the graphene band dispersion for small $\boldsymbol{q}$ is given by [6]

$$E_{\pm}(q) = \pm\hbar\upsilon_F|\boldsymbol{q}| + \mathcal{O}(q/K)^2. \tag{2.5}$$

Most of the work with graphene presented in literature is in the low carrier density regime, *i.e.*, linear energy dispersion with the conduction and valence bands intersecting at $q = 0$ with no energy gap, making it a zero band-gap semiconductor. Therefore the Fermi energy for 1LG is described by $E_F = \nu_F\hbar\sqrt{n\pi}$. The electrons and holes in graphene mimic relativistic particles due to a zero effective mass, which can be described by the Dirac's (relativistic) equation for fermions [7, 8].

2.1.2 Double-layer graphene

Double-layer graphene is a stack of two 1LG that are weakly coupled by interlayer hopping. The hopping is dependent on the specific stacking, *i.e.*, AA (Fig. 2.3a) or AB (Fig. 2.3b), and must be taken into account when extending the tight-binding approximation to 2LG [9]. In the case of AB stacked 2LG, the band energy is given by [6]

$$E_{\pm}^2(q) = V^2 + (\hbar\upsilon_F q)^2 + t_\perp^2/2 \pm \sqrt{4(V\hbar\upsilon_F q)^2 + (t_\perp\hbar\upsilon_F q)^2 + t_\perp^4/4}, \qquad (2.6)$$

where $t_\perp$ is the effective interlayer hopping energy and V is the externally applied electric field perpendicular to the layers (*i.e.*, the field between top and bottom layer). However, the band energy can be expanded for small momentum and $V \ll t$, such that [6]

$$E_{\pm}(q) = \pm\left[V - \frac{2V\,(\hbar\nu_F q)^2}{t_\perp} + \frac{(\hbar\nu_F q)^4}{2t_\perp^2 V}\right]. \qquad (2.7)$$

The electrochemical potential between the graphene layers results in a shift in the 2LG dispersion, thus, opening a small band-gap of $\Delta = 2V - 4V^3/t_\perp^2$at $q = \sqrt{2}V/\hbar\nu_F$, near the Dirac Point ($V \neq 0$, Fig. 2.3c) [6], which has been experimentally observed [10–13]. In the absence of a perpendicular electric field ($V = 0$, Fig. 2.3c), 2LG is a gapless

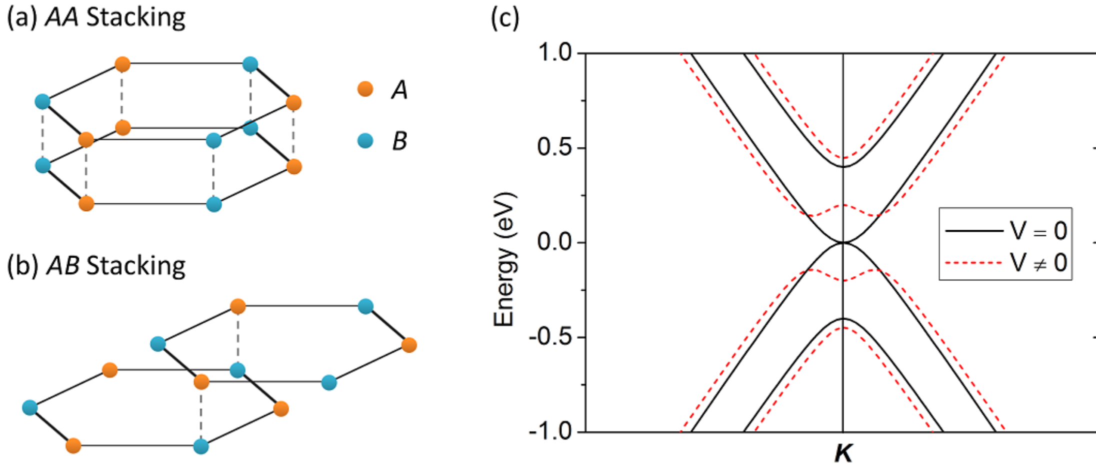

Figure 2.3: (a) AA and (b) AB stacked 2LG. (c) The electronic dispersion of 2LG near the $\boldsymbol{K}$ Dirac point. Adapted from Ref. [9].

semiconductor with parabolic energy dispersion [6]

$$E_{\pm}(q) \approx \frac{(\hbar\nu_F q)^2}{t_\perp} = \frac{\hbar^2 q^2}{2m}, \tag{2.8}$$

where $m = t_\perp/2\nu_F^2$ for small q . However, the parabolic dispersion for $V = 0$ is only valid for small q satisfying $\hbar\nu_F q \ll t_\perp$, whereas, a linear dispersion with $E_{\pm}(q) \approx \pm\hbar\nu_F$ is satisfied when $\hbar\nu_F q \gg t_\perp$, as with 1LG [6]. The crossover from quadratic to linear dispersion is easily understood when rewriting the 2LG band dispersion for $V = 0$ in the hyperbolic form [6]:

$$E_{2LG} = \mp m\nu_F^2 \pm m\nu_F^2[1 + (k/k_0)^2]^{1/2}, \tag{2.9}$$

where $k_0 = t_\perp/(2\hbar\nu_F)$ is a characteristic wave vector. For the effective 2LG band dispersion with $k \ll k_0$, $E_{2LG} \to k^2$ when $k \to 0$, *i.e.*, parabolic, whereas with $k \gg k_0$, $E_{2LG} \to k$ when $k \to \infty$, *i.e.*, linear.

2.2 Mechanical exfoliation

Nearly a decade on, the firstly discovered form of graphene, *i.e.*, with mechanical exfoliation [2], has yet to be outclassed in terms of the quality [2, 7, 14–17]. This simple yet effective method of mechanically exfoliating graphene flakes from HOPG with Scotch tape and transferring them onto Si/SiO_2 substrate can produced 1LG flakes that are now up to a millimetre wide [18]. These flakes exhibit tunable electron/hole concentrations in the range of $n = 10^9$-$10^{13}\ cm^{-2}$ using bottom gating [2, 19, 20] and carrier mobilities reaching $\mu \sim 20,000\ cm^2/Vs$ at room-temperature [2, 7, 20]. The mobility is generally limited by Coulomb and resonant scattering and mechanical defects such as ripples, however, suspending the graphene flake can dramatically increase the mobility to $\mu \sim 10^5\ (10^6)\ cm^2/Vs$ at room (low) temperature [19–23]. In graphene, carriers have been known to travel at mean free paths of $\sim 0.4\mu m$ without scattering [2]. These carriers travel at velocities of $\sim 10^6\ m/s$ denoted as the Fermi velocity (ν_F), behaving like massless Dirac fermions [7,14,16]. One example of a quantum mechanical phenomenon that occurs in 2D materials is the quantum Hall effect (QHE) [24], which is

typically observed at liquid helium temperatures ($\sim 4\,K$), however, the QHE can occur at room-temperature in graphene [16]. Although mechanically exfoliated graphene is still the best in terms of quality, the technique is not suitable for large scale production required for commercialisation of graphene electronics.

2.3 Chemical vapour deposition

One of the heavily researched areas of large scale graphene production is by the CVD method. The growth process involves using thin film metals such as Cu [25,26] or Ni [27,28] as a catalyst and exposing the heated surface (up to $1000°C$) to a hydrocarbon gas [25,29,30]. This method typically produces 1-10 layer thick graphene [29], which then has to be transferred onto an insulating substrate such as Si/SiO_2 with the use of mechanical and chemical treatments, for electrical measurements [30,31]. CVD graphene typically exhibits defects such as grain boundaries and wrinkles induced by the original grain boundaries and mismatched thermal expansion of the catalyst [31,32]. Without due care, further defects such as cracks can easily be induced from the transfer process [31]. The room (low) temperature mobilities of such films are on the order of $\mu \sim 2000$ (3700) cm^2/Vs [29,30,32]. Moreover, as with exfoliated graphene, CVD graphene transferred onto Si/SiO_2 also benefits from tunable carrier densities using bottom gating.

2.4 Epitaxial growth on SiC

SiC has been hailed as one of the most promising routes for industrialised graphene devices [33]. Early attempts of growing EG resulted in non-uniform formation of graphite [34–36]. More recently, groups have demonstrated reproducible 1-2 layer growth by carefully tuning parameters such as growth time, annealing temperature, atmospheric pressure and SiC crystalline form ($3C$, $4H$ and $6H$) [37–39].

2.4.1 Growth of graphene on SiC(0001)

The ideology of using SiC is such that it is a material with a comparable hexagonal structure to graphene, with the added benefit of layer by layer sublimation of Si from the surface during high-temperature annealing, leaving behind carbon that rearranges to forms the graphene honeycomb lattice. Moreover, the insulating nature of SiC means graphene grown in this manner can be instantly used without the need for damaging and unreliable process of transferring onto insulating substrates. The formation of graphene on a particular face of SiC, *i.e.*, Si- or C-face, is extremely important for controlled growth [40]. On C-face, *i.e.*, SiC(000-1), graphene grows quickly and wildly, producing islands of multiple graphene layer thickness [41]. On Si-face, *i.e.*, SiC(0001), graphene grows much slower, where optimised parameters can produce uniform 1LG coverage (Fig. 2.4a), with only a few percentage of 2LG (Fig. 2.4b) coverage [43].

The annealing of SiC(0001) leads to the modification of the surface starting from a Si-rich (33) structure [37, 44, 45], through to an intermediate (1×1) [46] and $(\sqrt{3} \times \sqrt{3})$ reconstruction [39, 44, 47], to the C-rich $(6\sqrt{3} \times 6\sqrt{3})R30^{o}$ structure (*i.e.*, buffer or interfacial layer, IFL) composed of the sp^3 carbon atoms bonded to the substrate Si layer [42, 48, 49], and finally the desired hexagonal lattice of graphene (Fig. 2.4) [50].

Attempts of growing EG in ultra-high vacuum (UHV) resulted in non-uniform graphene formation [44, 51–54]. However, introducing Ar suppresses the rate of sublimation of Si, producing graphene with better uniformity [40, 51]. The sublimation rate of Si and subsequently graphene formation are also sensitive to annealing temperature, requiring furnaces with inductive heaters offering precise temperature control and uniform coverage across the area of a 2-inch wafer [37, 38]. The Linköping group typically prefers higher temperature and argon gas pressure of $2000\,^{o}C$ and $760\,Torr$,

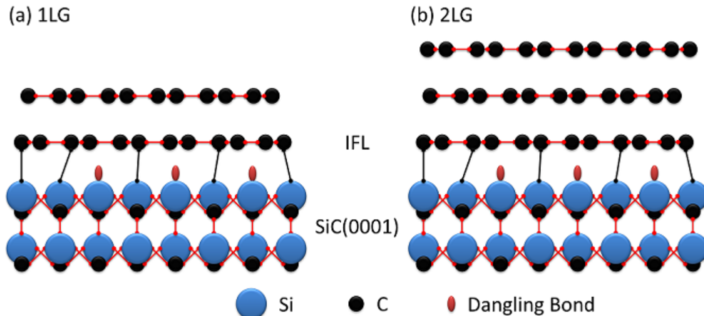

Figure 2.4: Schematic structure for (a) single-layer (1LG) and (b) double-layer (2LG) epitaxial graphene on interfacial-layer (IFL) and SiC(0001) substrate. Adapted from Ref. [42].

respectively [37, 55], while the IBM group prefers much lower settings of 1450 ^{o}C and $3.5 \times 10^{-4}\, Torr$, respectively [38]. The higher annealing temperature does result in a faster and more uncontrolled graphene formation, thus requiring complementary higher Ar pressure to further suppress the Si sublimation rate [37,51]. In either growth philosophy, highly uniform 1LG on a 2-inch $4H$ and/or $6H$-SiC wafer can be obtained with carrier mobilities in the range of μ = 1000-4000 cm^2/Vs at temperatures ranging from room temperature down to 4 K [33, 38, 39, 54, 56–58].

2.4.2 Effect of wafer miscut angle

Commercially available SiC wafers that are specified as nominally "on-axis" are typically characterised by the unintentional miscut angle, *i.e.*, angle from the axis of the SiC lattice to the surface of the wafer, of up to 0.5^{o}, giving rise to straight SiC terraces (Fig. 2.5) [59]. However, the terrace edges enhance the Si desorption, acting as nucleation sites for graphene growth, therefore playing a vital role in the graphene formation [44, 48]. The terrace edges initially start as relatively straight, however, the graphitisation significantly changes the surface topography, making them wavy [44,48,60,61]. The latter is more apparent in substrates with small miscut angles, where typically the terraces are wider [59]. Moreover, substrates with miscut angle below 0.1^{o} are more prone to the formation of deep pits as a result of the buffer layer domains pinning the decomposing surface step, where a new source of carbon is required for further graphitisation [44, 59].

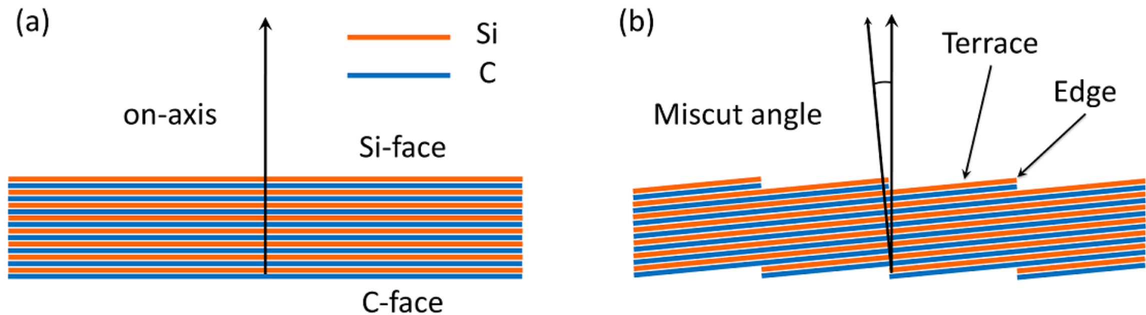

Figure 2.5: A simple schematic showing a $4H$-SiC substrate that is (a) on-axis and (b) miscut.

2.4.3 Layer uniformity

Despite the SiC steps in integers heights of 0.25 nm [62, 63], graphene grows over the steps continuously (Fig. 2.6a) [36, 64–66], which has been observed by imaging cross-sections of terrace steps using tunnelling electron microscopy [68–70]. As previously mentioned, the terrace edges act as nucleation sites for graphitisation and are often found to have additional graphene layer emanating (Fig. 2.6b), *i.e.*, on a sample with 1LG coverage, 2LG islands can be typically found emanating at the terrace step edges [62, 67, 68]. The electronic properties of graphene passing over the abrupt terrace edges were thought to be affected as a result of the strong curvature of graphene; nonetheless, theoretical calculations show little effect to the resistance of graphene [66]. However, Ji *et al.* experimentally measured a significant potential drop across terrace step edge related to a resistivity of 6.9 ± 2.9, 14.9 ± 3.9 and $24.7 \pm 4.3\,\Omega\mu m$ for 1LG crossing a single, double and triple substrate steps, respectively [71]. The change in resistivity of the graphene film over the terrace step edge is almost entirely attributed to the de-lamination of the film (Fig. 2.6a), significantly affecting the doping from the substrate [66, 71], which will be further discussed in Section 2.4.4.

Puckers (or otherwise known as folds, ridges, ripples or wrinkles) in EG are common defects [40, 52, 72–74]. The high temperature annealing process causes the substrate to expand and upon cooling the graphitised film experiences a compressive strain due to a difference in the thermal contraction [40, 72]. Inevitably, the graphene film buckles upwards under the immense stress [40, 72, 75, 76], forming puckers that are up to 30 nm in height [75].

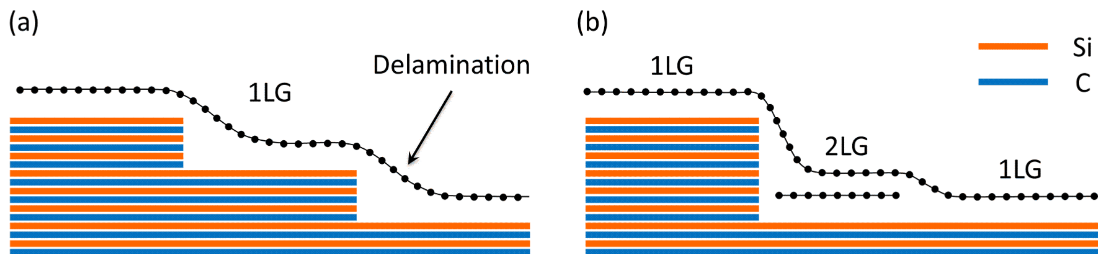

Figure 2.6: A simple schematic showing (a) continuous 1LG over terrace step edges and (b) additional graphene layer emanating at a terrace step edge of a $4H$-SiC substrate. Adapted from Ref. [67].

2.4.4 Influence of environmental conditions

Graphene, being a single atomic layer thick lattice, has the top of each carbon atom exposed to the environment. This unique property of graphene adds an extra complication in that the electronic properties of graphene can be severely affected by changes to the environment, such as gases [77–79] and humidity [80, 81], thus affecting the operation of devices.

Pearce *et al.* studied the effect on transport properties of n-type 1LG grown on $4H$-SiC(0001) to exposing gases such as O_2, NO_2 and N_2 [82]. Exposing the sample to low parts-per-billion (ppb) concentrations of NO_2 in N_2/O_2 (synthetic air of 4:1 ratio) background for 1 hour increased the resistance of the sample from ~ 700 to $\sim 840\,\Omega$ with an estimated recovery time of over 10 hours. The introduction of NO_2 shows a clear decrease in the electron carrier density of graphene due to the introduction of holes [78], nevertheless, the total combined effect of the NO_2 and the substrate is still n-type. However, exposing the samples to higher concentrations of NO_2 revealed n-p transition, indicating the doping was significant enough for holes to become the majority carriers. It was reported that NO_2 preferentially adsorbs at defects by transferring one electron from graphene to NO_2 [79, 83].

Similarly, water also affects the transport properties of graphene acting as a p-dopant [80, 81, 84]. Kazakova *et al.* used SPM techniques to study the effect of humidity on 1-3LG on $4H$-SiC(0001). Tapping phase AFM revealed preferential droplet-size adsorption of water on 2-3LG only at room temperature. Heating the sample to $50\,°C$ forced the water nanodroplets to move around and coalesce into larger sizes but only on 3LG. Further heating of the sample to $80\,°C$ evaporated all the water from 2-3LG. Cooling the sample back down to room temperature allowed the water to re-condense preferentially on 2-3LG.

2.4.5 Advantages and disadvantages

Epitaxially grown graphene on SiC has one of the greatest potentials for commercialisation, as readily available SiC wafers are ideal for 1LG growth on wafers up to 2-inch diameter in present time [33, 37, 38]. The highly insulating nature of SiC also adds an extra benefit in that graphene can be patterned without the need to transferred

onto an alternative substrate, as is the case with, for example, CVD graphene grown on metal substrates that need to be transferred to Si/SiO_2 substrate. EG is highly compatible with existing silicon processing technologies, potentially saving the industry from using up vast amounts of valuable resources on new equipment. Regardless of all the advantages to EG, there are a few disadvantages which has the possibility of hindering its development. The most immediate problem being the significantly higher cost of a single SiC wafer ($\sim$ 2000 USD for a 4-inch wafer [85]), making it economically non-viable at this stage. There are currently other more fundamental issues with EG; no group has been able to grow perfectly uniform defect-free 1LG or 2LG, albeit some have come as close as 97% uniform 1LG coverage with significantly reduced lattice defects, grain boundaries, nucleation sites and impurities.

2.5 Raman spectroscopy

Raman spectroscopy is widely regarded as the definitive way of characterising the structures of graphitic materials and especially graphene [86, 87]. The method can be applied to determine the structure in various systems, such as free-standing exfoliated graphene [88–90], exfoliated graphene transferred on various substrates (such as Si/SiO_2) [91–94], epitaxially [92, 95, 96] and CVD grown graphene [26, 29, 97], all of which can have a shifted E_F via chemical doping [98–100] or electrical gating [101,102].

2.5.1 Phonon dispersion

Raman spectroscopy is a direct measurement of the phonon dispersion [103]. In graphite, there are three acoustic (A) and three optic (O) phonon dispersion bands related to the two (A and B) carbon atoms [87]. These consist of two phonon branches that are perpendicular to the graphene plane, *i.e.*, out-of-plane (o) and four phonon branches that are parallel to the graphene plane, *i.e.*, in-plane (i) [87]. The directions of the vibrations in graphene are generally considered with respect to the direction of the carbon-carbon (AB) atoms, categorising the parallel and perpendicular vibrations as longitudinal (L) and transverse (T), respectively [87], hence the high symmetry directions ($\mathbf{\Gamma K}$ and $\mathbf{\Gamma M}$). The curves of the six phonon dispersion modes are assigned

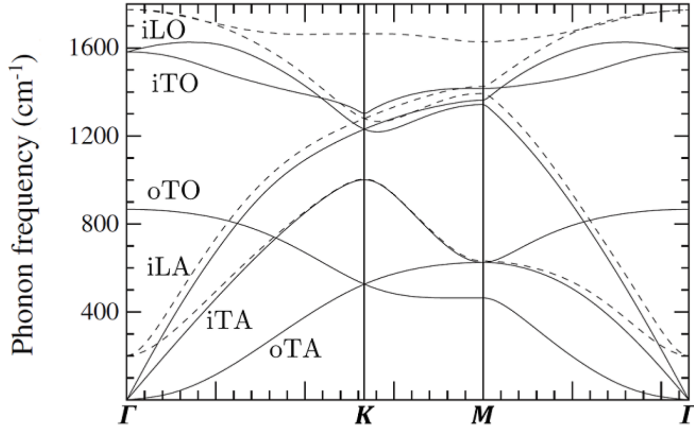

Figure 2.7: Phonon dispersion of graphene from density functional theory calculations showing the iLO, iTO, oTO, iLA, iTA and oTA phonon modes. Reprinted (adapted) with permission from Ref. [103]. Copyright 2008 by The American Physical Society.

iLO, iTO, oTO, iLA, iTA and oTA (Fig. 2.7) [87]. The iLO and iTO phonon modes are the active Raman modes in graphene, which are associated with the degenerate zone centre E_{2g} [87, 93, 104].

2.5.2 Raman spectra of graphene

2.5.2.1 Exfoliated graphene

The most intense features of the Raman spectra for exfoliated graphene on Si/SiO_2 (Fig. 2.8a) are the G- and G′-peaks ($\sim$ 1582 and $\sim$ 2700 cm^{-1}, respectively, using a 514 nm laser, Fig. 2.8b) [87, 93, 94]. Graphene samples containing a disordered crystalline lattice structure or at the terminating edge of graphene gives rise to the

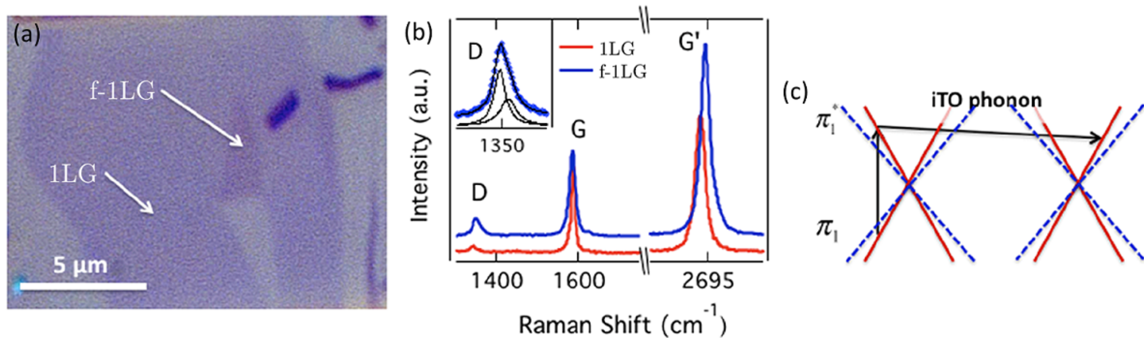

Figure 2.8: (a) Optical microscope image of 1LG and folded 1LG (f-1LG) on Si/SiO2 substrate. (b) Raman spectra for 1LG and f-1LG. The inset in (b) shows the magnified D-peak for f-1LG, fitted with two Lorentzians. (c) Band structure of 1LG near the Dirac point showing the transition of iTO phonon mode. Reprinted with permission from Ref. [94]. Copyright 2012 American Chemical Society.

D-peak ($\sim$ 1350 cm^{-1} using a 514 nm laser, Fig. 2.8b) [87, 104]. In the case of Fig. 2.8a, additional defects are introduced as the 1LG folds over (f-1LG), giving rise to a more intense D-peak (Fig. 2.8b inset). The G-peak is related to the doubly degenerate phonon modes (iLO and iTO) coming from the first-order Raman scattering process. The G′-peak (also referred to as the 2D-peak due to its $\sim$ 2 times larger phonon frequency compared to the D-peak) is related to the two iTO phonons near the $\boldsymbol{K}$ point coming from the second-order scattering process (Fig. 2.8c) [94]. The D-peak is also related to the second-order process involving a single iTO phonon.

2.5.2.2 Epitaxial graphene on SiC

Graphene grown on SiC(0001) consists of an additional IFL composing of sp^3 carbon atoms that are covalently bonded to the substrate Si. The IFL is an n-dopant due to electron charge transfer to the graphene [43, 56, 57, 105, 106], shifting the Fermi energy by up to $E_F = 400meV$ towards the conduction band in 1LG [105]. The IFL has similar structural properties to graphene, also producing peaks around 1300-1750 cm^{-1} (Fig. 2.9a) [92, 107, 108]. These peaks inevitably are superimposed on top of the graphene

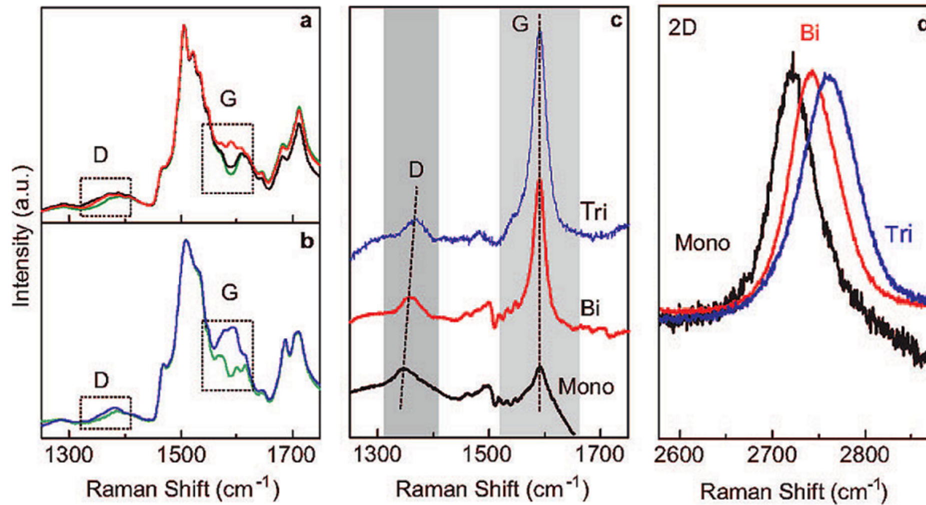

Figure 2.9: Raman spectra for (a) 1LG (Mono, black), 2LG (Bi, red), 6H-SiC(0001) reference (green), (b) 3LG (Tri, blue) and the 4H-SiC(0001) reference (green). The dotted boxes in (a) and (b) marks the region of graphene D- and G-peaks that are partly masked by the Raman signal from the SiC substrate. (c) Raman spectra for 1-3LG subtracted from their respective bare SiC reference. (d) Normalised Raman spectra near the G′-peak (2D) for epitaxial 1-3LG. Reprinted with permission from Ref. [92]. Copyright 2008 American Chemical Society.

G-peak [92, 107], adding an extra challenge towards precise analysis of the graphene Raman spectrum [96]. Furthermore, the IFL does not produce a G′-peak [109].

Raman studies on 1-2LG on 6H-SiC(0001) (Fig. 2.9a) and 3LG on 4H-SiC(0001) (Fig. 2.9b) using a 488 nm laser reveals D- and G-peaks, albeit superimposed on to the signal from their respective substrates, which makes it difficult for layer analysis from the raw data [92]. However, subtracting the reference SiC spectra reveals D-peaks ($\sim 1360\,cm^{-1}$) and G-peaks ($\sim 1591\,cm^{-1}$) for 1-3LG (Fig. 2.9c). When comparing the G-peak of exfoliated graphene ($\sim 1587\,cm^{-1}$) with EG [92], the compressive strain on graphene induced by the SiC(0001) substrate blue-shifts the peak by $\sim 4\,cm^{-1}$.

EG also exhibits a strong G′-peak, where 1LG, 2LG and 3LG peaks are located at ~ 2721, ~ 2743 and $\sim 2760\,cm^{-1}$ and the full width at half-maximum (FWHM) are ~ 46, ~ 64 and $\sim 74\,cm^{-1}$, respectively, showing a gradual progression of both the G′-peak and the FWHM from 1LG-2LG-3LG (Fig. 2.9d) [92]. In comparison to exfoliated graphene from HOPG, the FWHM for 1LG and 2LG is < 30 and $50\,cm^{-1}$, respectively [92]. While both exfoliated and epitaxial 1LG exhibits a G′-peak that can be fitted with a single Lorentzian, it is not as straightforward for 2LG. AB stacked 2LG typically requires four Lorentzians to fit the G′-peak due to an asymmetric shape of the peak with an added shoulder structure, whereas AA or any other stacking of 2LG can be fitted with a single Lorentzian [87]. This is because the electronic structure of non-AB stacked 2LG resembles the massless Dirac fermions in 1LG.

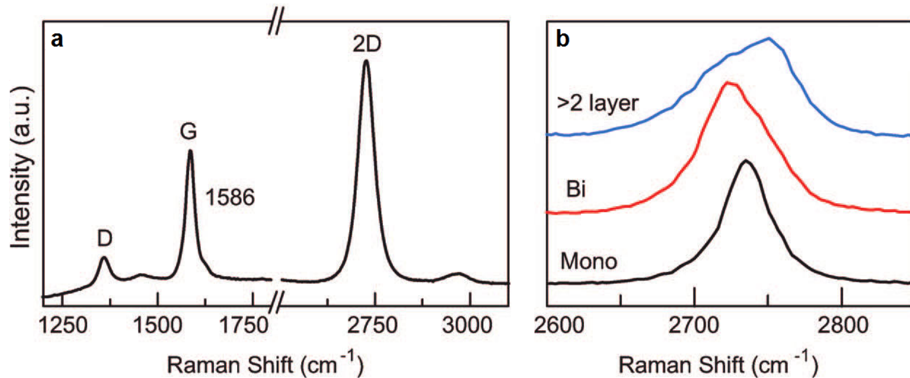

Figure 2.10: Raman spectra for epitaxially grown graphene on SiC, that was transferred to Si/SiO_2 substrate via mechanical exfoliation, showing the spectra for (a) 1LG and (b) G′-peak for 1LG, 2LG and >2LG. Reprinted with permission from Ref. [92]. Copyright 2008 American Chemical Society.

Lee *et al.* also obtained Raman spectra of epitaxial 1LG that was exfoliated from SiC and transferred to Si/SiO_2 substrate in order to investigate the effect of the IFL on epitaxially grown graphene. Transferred EG loses the forest of dominating peaks present in measurements for graphene on SiC and appears more like spectra for exfoliated graphene from HOPG, however with the presence of a small D-peak, related to the defects in epitaxially grown graphene (Fig. 2.10a). A more detailed analysis reveals a change in the shape of the G′-peak and especially with the spectra for 2LG or thicker, where accurate fitting requires multiple Lorentzians (Fig. 2.10b), thus resembling the spectra for exfoliated graphene from HOPG (Fig. 2.9d).

2.5.3 Raman mapping

Raman spectroscopy can also be performed over an area, mapping quantities such as the peak position, FWHM and relative intensities of the peaks, to build up 2-dimensional images [95,110]. The technique is relatively time consuming due to the slow acquisition time of the Raman spectroscopy at each point. However, the acquisition time can be decreased by using a more powerful laser to increase the signal or using a more sensitive detector. With increasing the laser power, one has to consider the heat dissipation in the sample, which can potentially lead to permanent damage [87]. The major disadvantage of Raman mapping is the low spatial resolution, which is generally limited by the spot size of the laser to $\sim$ 0.4-1 μm [95,110–114], making it two orders of magnitude lower than SPM techniques (10’s of nanometres).

The AFM topography image performed on mechanically exfoliated HOPG, transferred onto Si/SiO_2 substrate reveals different layer thickness of graphene, where “0” indicates the substrate and numbers 1-6 indicates the graphene layer thickness (Fig. 2.11a and Fig. 2.11b) [110]. The 2-dimensional mapping of the Raman spectra performed on the same region of the sample has been filtered to show the G-peak intensity integrated from 1537 to 1622 cm^{-1} (Fig. 2.11c and Fig. 2.11d) and the FWHM of the G′-peak (referred to as the D′-peak) (Fig. 2.11e and Fig. 2.11f) producing a false-colour image [110]. Comparing the line profiles of the integrated G-peak intensity to the topography revels good correlation and clearly distinguishing graphene domains of different thickness. However, the FWHM of the G′-peak can only be used to identify

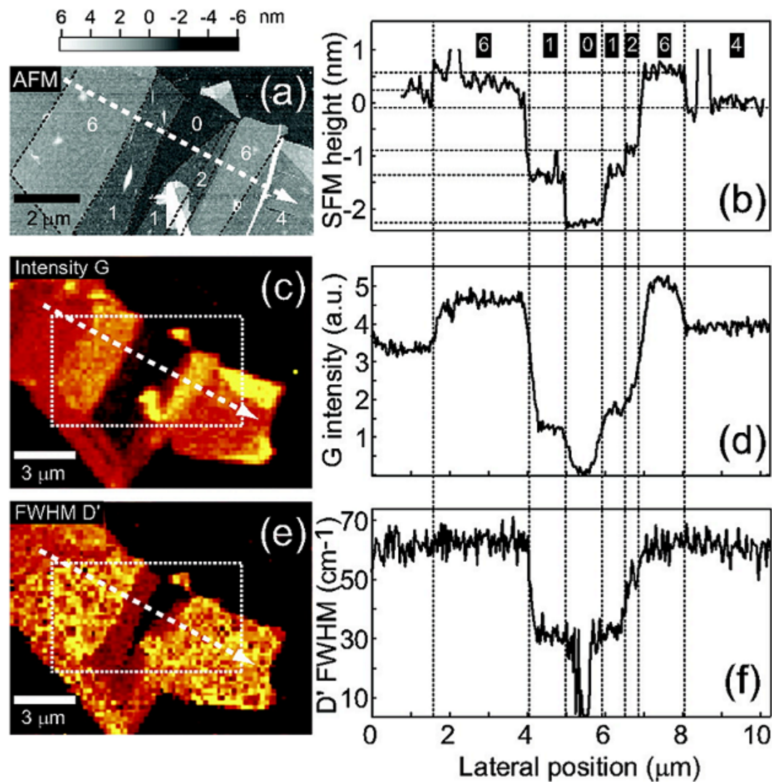

Figure 2.11: (a) Topography image of a few-layer graphene flake obtained using AFM. Raman mapping showing (c) the intensity of the G-peak and (e) the FWHM of the G′-peak (referred to as the D′-peak). (b), (d) and (f) are the cross-sectional plot along the white dashed arrows indicated in (a), (c) and (e), respectively. Dashed squares in (c) and (e) corresponds to the area in (a). Reprinted with permission from Ref. [110]. Copyright 2007 American Chemical Society.

domains of single- and few-layers of graphene.

2.6 Surface potential mapping

2.6.1 Identifying graphene thickness domains

AFM is a widely accessible tool used for straightforward topography measurements with atomic height resolution. This makes it an obvious choice for determining graphene layer thickness. The technique is successfully used for graphene on Si/SiO_2 substrate (Fig. 2.12a) [115–118], however, the same cannot be said for EG on SiC substrate due the complex nature of the topography of the substrate (Fig. 2.12b) [61, 62, 72, 119]. KPFM is an AFM based technique for imaging the surface contact potential difference (ΔV_{CPD}) between the probe and the sample [62, 116, 120–125]. Often when topography

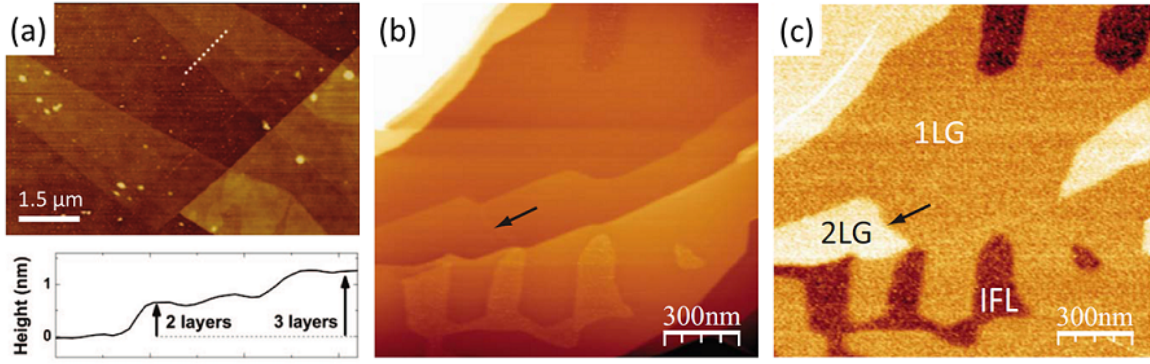

Figure 2.12: (a) Topography map of few graphene layers on Si/SiO_2 substrate. Inset in (a) shows a topography line profile along the indicated dotted line. (b) Topography and (c) V_{CPD} mapping of epitaxial graphene on 6H-SiC(0001). The arrows point to the boundary of 1-2LG. (a) is reprinted with permission from Ref. [115]. Copyright 2009 American Chemical Society. (b) and (c) are reprinted with permission from Ref. [62]. Copyright 2008 AIP Publishing LLC.

measurements are ineffective, KPFM has been used to map out graphene domains, where contrast arises due to differences in the electrical properties of each graphene layer thickness (Fig. 2.12c) [43, 62, 116, 123, 125].

Histogram analysis on Fig. 2.12c done by Filleter *et al.* revealed $135 \pm 9 meV$ decrease in work function from 2-1LG and a further decrease of $\sim 140\, meV$ from 1LG to IFL at room temperature, in UHV, carefully avoiding surface contaminants [62]. Uncontrolled levels of surface contaminations affect the ΔV_{CPD} of each graphene layer differently, producing relative contrasts that can be complex to interpret. Understanding the effect of substrate and environmental doping on the work function of graphene is a key step towards accurate interpretation of the exact number of layer thickness.

Yu *et al.* performed work functions measurements on exfoliated 1LG and 2LG on Si/SiO_2 contacted with Cr/Au electrodes (Fig. 2.13) [124]. Unlike EG on SiC, graphene on Si/SiO_2 substrate is intrinsically p-doped. However, using doped Si substrates together with the insulating SiO_2 layer has the added benefit of tunable carrier density of graphene by simply applying a voltage to the substrate, back gating the device. By using back gate, the E_F of graphene can be modulated to either side of the Dirac point, enabling one to counteract the effect of substrate and environmental doping. Using Au-coated probes with a known work function (Φ_{probe}), the work function of the sample (Φ_{sample}) can be determined: $\Phi_{sample} \approx \Phi_{probe} - e\Delta V_{CPD}$ [126]. The work function

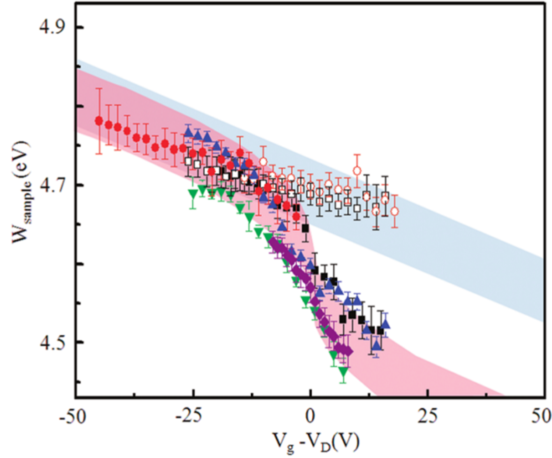

Figure 2.13: Work function of 1LG (filled symbols, shaded in red) and 2LG (open symbols, shaded in blue) as a function of applied gate voltage (V_g) minus the gate voltage at the Dirac point (V_D). The filled red, green and purple symbol data sets were obtained in air, while all other data sets were obtained in dry nitrogen environment. Reprinted with permission from Ref. [124]. Copyright 2009 American Chemical Society.

of 1LG and 2LG at the Dirac point were reported to be $\Phi_{1LG} = 4.57 \pm 0.05\, eV$ and $\Phi_{2LG} = 4.69 \pm 0.05\, eV$, respectively (Fig. 2.13) [124].

2.6.2 Contact resistance

In KPFM, the probe acts as a movable electrical contact making it an excellent tool for measuring the potential drop and subsequently the contact resistance between graphene and the electrode [124]. Fig. 2.14a shows such measurement performed on a graphene device with voltage (V_{SD}) applied across the source-drain electrodes. Within the channel, current-V_{SD} characteristics reveal a linear relation with the total circuit resistance ($3.44\, k\Omega$) provided by the slope. The KPFM line profiles reveal the potential

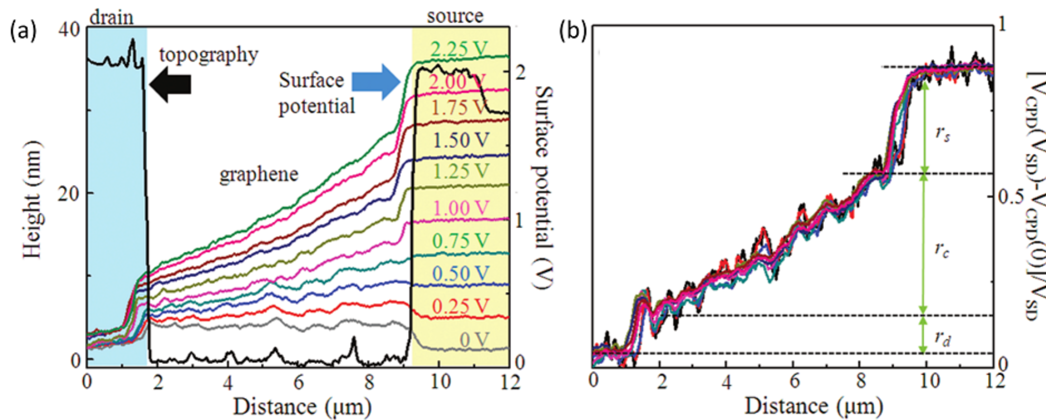

Figure 2.14: (a) Topography and V_{CPD} line profile along the device, *i.e.*, electrode-graphene-electrode, at voltages V_{SD} = 0-2.25 V applied across the source-drain electrodes. (b) V_{CPD} line profiles shown in (a) are referenced to the grounded drain electrode and normalised by V_{SD}. Reprinted with permission from Ref. [124]. Copyright 2009 American Chemical Society.

distribution across the source-drain electrodes at V_{SD} = 0-2.25V. Inspection of the surface potential drops of the normalised line profiles ($[V_{CPD}(V_{SD}) - V_{CPD}(V_{SD} = 0)]/V_{SD}$) provides an estimation of the contact resistance for source ($r_s = 1.24\,k\Omega$) and drain ($r_d = 0.5\,k\Omega$) electrodes and the graphene channel ($r_c = 1.7\,k\Omega$) (Fig. 2.14b).

2.7 Summary

In summary, graphene exhibits extraordinary electrical and mechanical properties with high hopes for future technological applications in many areas. However, for some of these applications to be a reality, wafer scale production of graphene with careful control of its unique properties are required. One of the most promising routes for wafer scale graphene is via epitaxial growth on SiC. While Raman spectroscopy is widely used to characterise graphene samples, surface potential mapping techniques are faster alternative way of obtaining nanometre scale characterisations. Surface potential mapping techniques applied to EG samples have shown significant inhomogeneities in the graphene layer thickness. The latter is possible as the subtle changes in electronic properties of different graphene layer thickness are described by unique band structures. While *bulk* transport properties provide only average statistics of these electronic properties, surface potential mapping techniques provide nanometre scale characterisations. Accurate characterisation of the transport properties is essential as industry pushes the limits of fabrication processes to produce ever smaller devices. My objective is to use bulk transport and noise measurements to study the effects of miniaturisation of Hall bar devices. In addition, SPM techniques are used in conjunction with bulk transport measurements to further understand various aspects such as fabrication processes, environmental doping, effects of 2LG on bulk transport, edge effects and electrical/magnetic gating on uniform and non-uniform submicron scale EG Hall bar devices.

Chapter 3

Bulk electronic properties of Hall sensors

This chapter provides bulk transport and noise measurements of micron to submicron scale Hall bar devices. The Hall bar geometry is ideal for characterising local variations in the electronic properties of the material. The devices were characterised at room temperature, in ambient conditions, using the classical Hall effect [127] and 4-terminal resistance measurements. These measurements were used to study the miniaturisation effects by characterising the carrier density, carrier mobility, Hall coefficient and mean free path. The performance of Hall bar devices were further studied using noise spectral density measurements by characterising the minimum detectable field. Miniaturisation of devices often results in an increase in resistance of the total measurement circuit, resulting in an increase in $1/f$ noise. The potential of graphene Hall bar devices for magnetic field sensing applications was also realised by sensing the stray field of a single 1 μm diameter magnetic bead. The detection was carried out using an AC/DC Hall magnetometry technique that was originally pioneered by Besse *et al.* [128]. The performance of EG devices was compared to that of well-established state-of-the-art semiconductor devices.

3.1 Classical Hall effect

The Hall effect is the generation of a transverse potential difference (V_{xy}) with respect to the directional flow of the electrical current (I_{bias}) within an applied magnetic field (B) perpendicular to the current [127]. The transverse voltage, typically referred to as the Hall voltage (V_H), is generated by the deflection of the current flow due to the charged carriers experiencing the Lorenz force. The sensitivity of the material to the generation of the V_H is characterised by the Hall coefficient:

$$R_H = \frac{V_H}{I_{bias}B} = \frac{1}{ent} \equiv \frac{1}{en_{2D}}, \tag{3.1}$$

where n is the carrier density, t is the material thickness and e is the electronic charge [129]. However, due to the two-dimensional nature of graphene, it is more convenient to use the 2D carrier density (n_{2D}), which will simply be referred to as n throughout the thesis. The sensitivity can be characterised by measuring V_H while sweeping B, yielding a linear relation that can be fitted with Eq. 3.1. The Hall coefficient is a direct measure of the material carrier density. In this form, Eq. 3.1 yields a positive (negative) value for the Hall coefficient of n-type (p-type) material.

3.2 Transport properties of nominally 1LG devices

Hall sensors with cross size ranging from 0.1-19.6 μm (sample #1) were fabricated out of nominally 1LG (Appendix A) and characterised at room temperature[1], in a dark environment (Fig. 3.1a), using a GMW 5403 water cooled copper coil electromagnet (powered by a TTi QPX1200) to generate an out-of-plane DC magnetic field (B_{DC}) (Fig. 3.1b). The devices were current biased, using a Howland current source, at $I_{bias} = 10\text{-}50\,\mu A$ and the V_H response was simultaneously measured for all three crosses using digital voltmeters (Agilent 34420A), while sweeping the B_{DC} from $0 \rightarrow 0.5 \rightarrow 0\,T$ (Fig. 3.1c). LabVIEW was used to control the instruments over GPIB and serial interfaces to automate the measurements. Electrical measurements were conducted

[1]Note: Recent investigations show that size of devices are smaller than originally designed, therefore the interpretation of results presented in Section 3.2 and 3.3 are somewhat different from those published in Panchal *et al.*, *Journal of Applied Physics*, 111, 07E509, 2012.

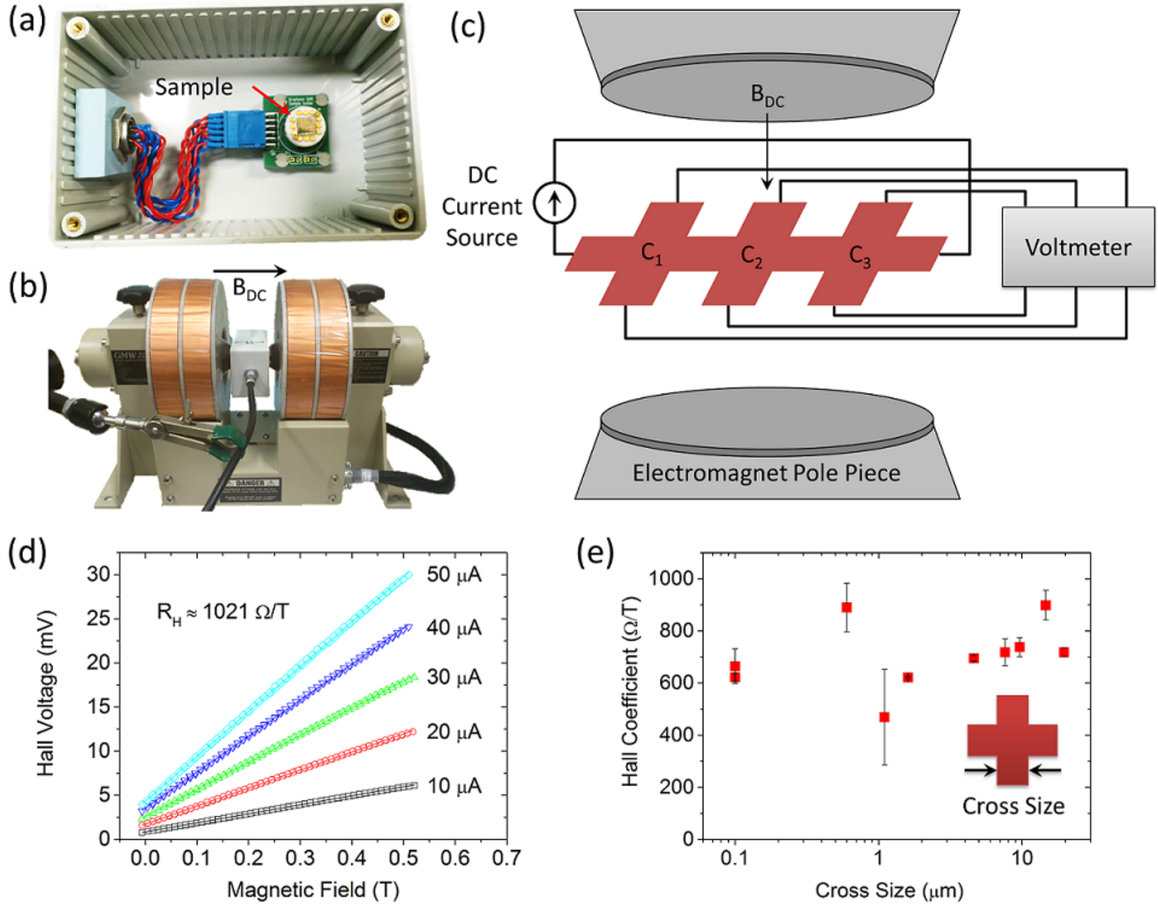

Figure 3.1: Images of (a) sample box placed between the pole pieces of (b) copper coil magnet. (c) A schematic of the Hall voltage measurement setup showing a triple cross device placed in out-of-plane DC magnetic field (B_{DC}). C_1, C_2 and C_3 represents crosses 1, 2 and 3, respectively. (d) Magnetic field dependence of the Hall voltage for a single cross of a 600 nm wide device at I_{bias} = 10-50 μA in increments of 10 μA. The R_H is extracted from each I_{bias}. (e) Cross size dependence of the R_H, where each data point represents a single device with the values of the three crosses averaged and plotted together with the standard deviation.

using shielded cables and die cast aluminium breakout boxes connected to a common ground, thus avoiding ground-loops, which can be a source of electrical noise from the environment. Fig. 3.1d shows the B_{DC} dependence of the linear V_H response for a single cross of a 600 nm wide device. The sweep was performed at I_{bias} = 10-50 μA in increments of 10 μA. $R_H \sim 1,020\ \Omega/T$ was determined by dividing the gradient of the slope (V_H/B_{DC}) by the respective I_{bias} and averaging the R_H for the five individual I_{bias}. This method was applied to all the sensors with each device producing three values of R_H, one for each cross, which has been averaged and plotted together with their standard deviation (Fig. 3.1e). The cross size dependence of the R_H shows no

clear trend in the magnetic field sensitivity with miniaturisation of the sensor within the sizes investigated here. On average, the sensors exhibit $R_H \sim 750\,\Omega/T$, the result of a low electron carrier density of $n_e \sim 8.3\times10^{11}\,cm^{-2}$ calculated using Eq. 3.1. The lowest carrier density measured from this particular sample was $n_e \sim 6.1 \times 10^{11}\ cm^{-2}$ (Fig. 3.1d), which is comparable to n_e at cryogenic-temperatures [56, 130, 131] and typically lower than the values at room-temperature [33, 38, 59] published by others in the field. While there is no clear cross size dependence of R_H, the 1.1 μm device does exhibit a relatively large R_H variation compared to the other devices (Fig. 3.1e). Although the devices were fabricated out of nominally 1LG, Section 5.6 demonstrates that islands of 2LG present on the device leads to an increase (decrease) in n_e (R_H).

Devices with multiple crosses are also ideal for measuring the sheet resistance (R_s) of the material (Fig. 3.2a) using a straightforward 4-terminal resistance (R_4) measurement technique that excludes contributions from electrical cables, wire bonding and contact resistance. R_4 was determined by applying I_{bias} across the channel and measuring the potential drop (V_{xx}) from C_1 to C_3 in zero field (Fig. 3.2a inset). The sheet resistance remain relatively unchanged at $R_s \sim 2.5\ k\Omega$, showing no clear dependence with device

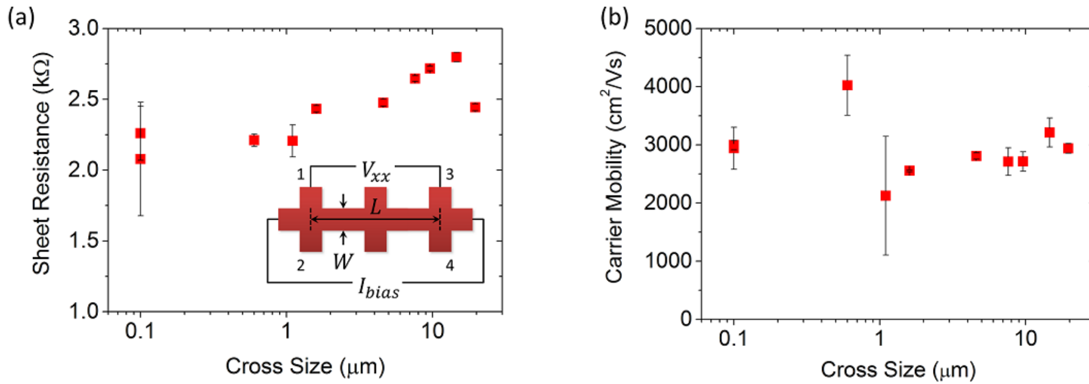

Figure 3.2: (a) Cross size dependence of the sheet resistance (R_s), which is a measure of only the channel resistance per unit square. Each data point represents a single device with the values from the four measurement combinations (1-3, 2-4, 1-4, 2-3) averaged and plotted together with the standard deviation. (b) Cross size dependence of the carrier mobility, where each data point represents a single device with the values of the three crosses averaged and plotted together with the standard deviation.

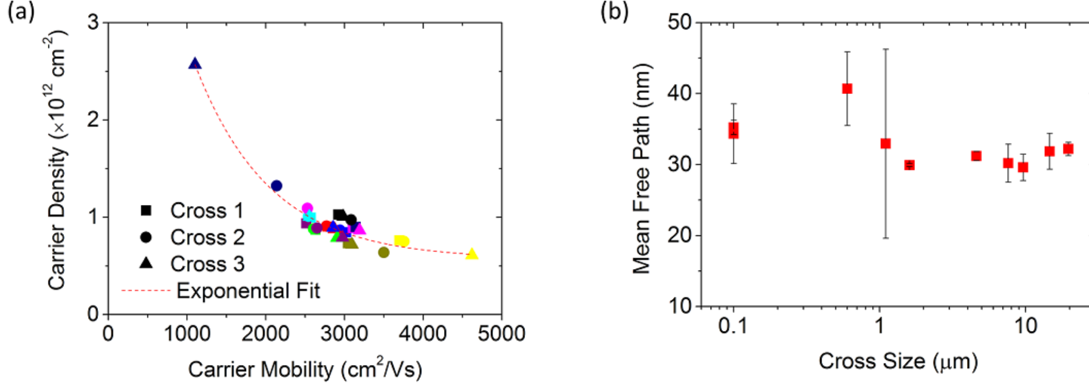

Figure 3.3: (a) The relation between the carrier density and carrier mobility. (b) Cross size dependence of the mean free path, where each data point represents a single device with the values of the three crosses averaged and plotted together with the standard deviation.

miniaturisation. The carrier mobility can also be calculated using

$$\mu = \frac{R_H}{R_4} \times no.\ of\ \square's = \frac{R_H}{R_s}. \tag{3.2}$$

R_s is given by ρ/t, where ρ and t are the sheet resistivity and thickness, respectively and hence $R_4 = R_s \times no.\ of\ \square's$, where the $no.\ of\ \square's$ is the ratio of channel length (L) to width (W) (Fig. 3.2a inset). The cross size dependence of μ is shown in Fig. 3.2b, where each data point represents a single device with the values of the three crosses averaged and plotted together with the standard deviation. The carrier mobility also remains relatively constant with miniaturisation at $\mu \sim 2900\, cm^2/Vs$, indicating there is no significant deterioration in the electronic properties of EG devices down to widths of 100 nm. The small variations in the carrier mobility are related to the variations in the carrier density. For example, Fig. 3.3a shows an exponential increase in carrier mobility with decreasing carrier density.

Electron-electron is the dominant scattering mechanism that dictates the inverse relation between the carrier density and mobility, however only at temperatures $< 40\, K$, where the phonons are frozen out. In the present case (Fig. 3.3), the measurements are conducted at room temperature, thus, electron-phonon interaction becomes the dominating scattering mechanism [131]. This results in the inverse relationship between the carrier density and mobility, which has been previously demonstrated theoretically [132] and experimentally [133] for the case of exfoliated graphene on SiO_2. The

electron-phonon scattering in epitaxial graphene is further enhanced due to effective coupling to the LO phonon mode ($104\,meV$) of $4H$-SiC [134]. These interactions can be characterised by the mean free path (λ), given by [22]

$$\lambda = \frac{h}{2e}\mu\left(\frac{n}{\pi}\right)^{1/2}, \tag{3.3}$$

where h is Plank's constant. With $\lambda \sim 30\,nm$ being smaller than the dimensions of all the devices described here (Fig. 3.3b), the electron transport at room temperature is strongly diffusive. While the lack of cross size dependence signifies the importance of intrinsic factors (*i.e.*, defects in the crystal structure of the graphene and SiC substrate, impurities, grain boundaries, non-uniform number of graphene layers and substrate doping), extrinsic factors (*i.e.*, environmental doping, unoptimised design of devices and fabrication processes) can also affect the performance of devices. In comparison to exfoliated graphene transferred to SiO_2 substrate with $n \sim 10^{12}\ cm^{-2}$ and $\mu \sim 10,000\,cm^2/Vs$, the mean free path can be as large as $\lambda \sim 100\,nm$ at room temperature and $\lambda \sim 1.2\,\mu m$ at $\sim 5\,K$ [22].

3.3 Noise mechanisms

The performance of the devices, *i.e.*, B_{min}, was investigated through noise spectral density measurements for each cross individually by directly connecting the V_H terminals to the input of a fast Fourier transform spectrum analyser (Stanford Research Systems SR780) in differential mode. The voltage noise (ν_N) can be represented by [135]

$$\nu_N = \left(\int_{f_1}^{f_2} S_{NV}(f)df\right)^{1/2}, \tag{3.4}$$

where $S_{NV}(f)$ is the spectral density function at given range of frequencies (f). For Hall sensors, the voltage (V) noise spectral density can be written as $S_{NV}(f) = S_{VT}(f) + S_{V\alpha}(f) + S_{VGR}(f)$, where S_{VT}, $S_{V\alpha}$ and S_{VGR} represents the Johnson-Nyquist (thermal), $1/f$ (flicker) and generation-recombination (GR) noise spectral densities, respectively.

Substituting the formula for the three different noise mechanisms gives [135]

$$S_{NV}(f) = \sqrt{4k_BTR\Delta f} + \frac{\alpha}{N}\frac{1}{f^{\gamma}}V^2 + \frac{A_{sens}}{1+(2\pi f\tau)^2}V^2, \tag{3.5}$$

where k_B, T and R are the Boltzmann's constant, absolute temperature and the total voltage lead resistance, respectively. α and N are the Hooge parameter and the number of charge carrier in the sensing area (A_{sens}), respectively. $\gamma \approx 1$ and $A_{sens} = 4\langle \Delta N^2 \rangle \frac{\tau}{N^2}$, where τ is the lifetime of the GR-centre.

The noise was measured for all the devices up to $f = 4.6\,kHz$ for $I_{bias} =$ 0-50 μA at 10 μA increments. Fig. 3.4a shows the raw noise spectra for a single 600 nm wide cross. At $I_{bias} = 0$, the noise reaches the Johnson-Nyquist noise floor limit at $S_{VT} \sim 30\,nV/\sqrt{Hz}$ for a cross with voltage lead resistance $R_2 \sim 60\,k\Omega$ at room temperature.

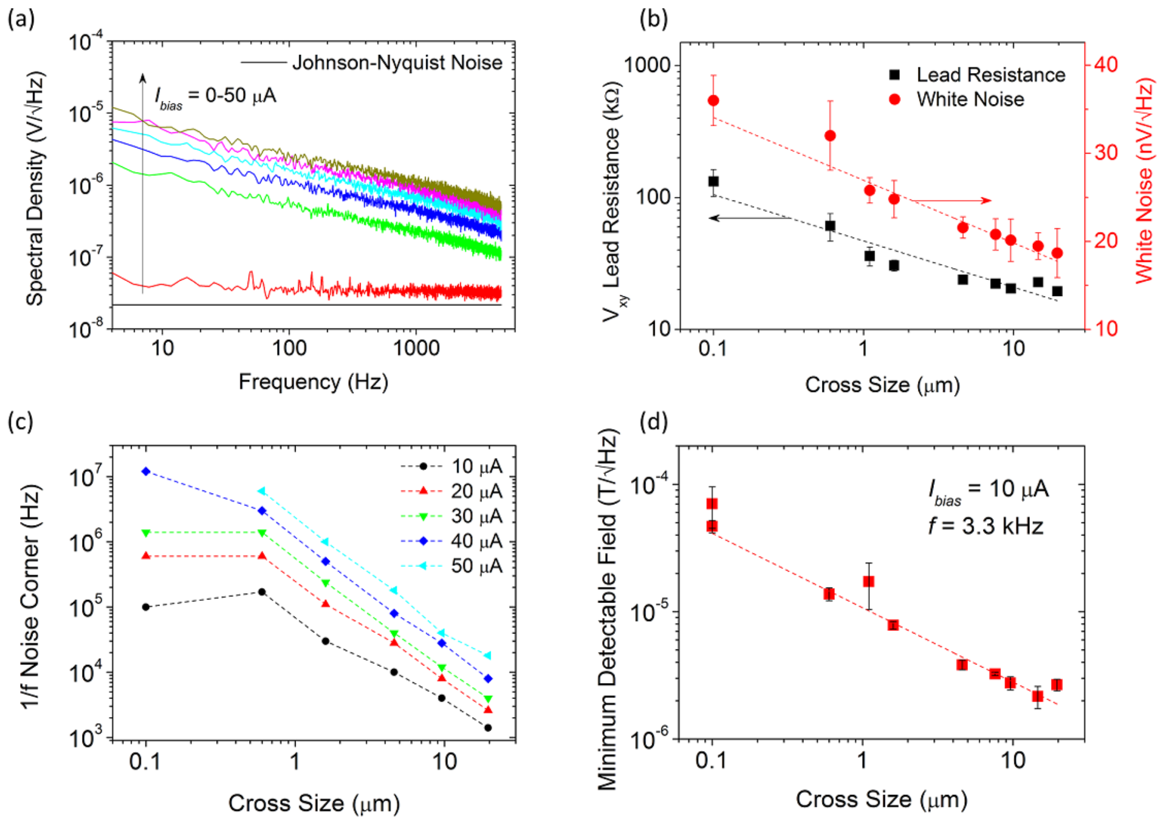

Figure 3.4: (a) The noise spectral density for a single 600 nm wide cross at $I_{bias} =$ 0-50 μA in increments of 10 μA. The cross size dependence of (b) the total voltage lead resistance and the white noise level at $f = 3.3\,kHz$, (c) $1/f$ noise corner frequency and (d) the minimum detectable field at $f = 3.3\,kHz$ and $I_{bias} = 10\,\mu A$. The dashed lines are a guide for the eye. Each data point in (b) and (d) represents a single device with the values of the three crosses averaged and plotted together with the standard deviation.

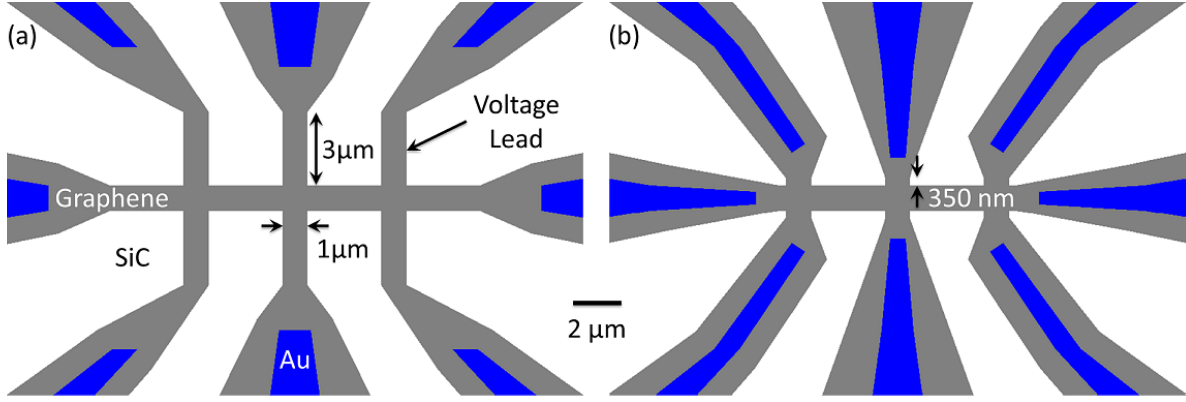

Figure 3.5: (a) Current design of a 1 μm wide device from sample #1. (b) Potential design of a 1 μm wide device optimised for lower $1/f$ noise.

Moreover, S_{VT} decreases exponentially with exponential increase in cross size, primarily related to a lowering of the R_2 (Fig. 3.4b). However, the sensor exhibits a large $1/f$ contribution at $I_{bias} > 0$ and even more so for smaller devices, which is illustrated by extrapolating the frequency at which $S_{VT} = S_{V\alpha}$, known as the $1/f$ noise corner (Fig. 3.4c). Using these noise measurements, $B_{min} = S_{NV}/I_{bias}R_H$ was determined for $I_{bias} = 10\ \mu A$ at $f = 3.3\ kHz$ for all the devices (Fig. 3.4d). The results show that while $B_{min} \sim 2\ \mu T/\sqrt{Hz}$ for the 14.6 μm wide device, B_{min} exponentially increases to $B_{min} \sim 50\ \mu T/\sqrt{Hz}$ for the 100 nm device. The increase in B_{min} with miniaturisation can be attributed to the $1/f$ noise, which ultimately is the result of long and narrow strips of graphene dramatically increasing R_2 of the voltage leads (Fig. 3.5a). B_{min} can be significantly improved by shortening and widening the rather long and narrow voltage leads (Fig. 3.5b), thus decreasing R_2. The other significant contributing factor to R_2 is related to the contact resistance between the graphene and the Au leads, which will be discussed in detail in Section 5.3.

In different types of materials and devices, $1/f$ noise results from different fluctuation processes. In general, the $1/f$ noise in conventional semiconductor devices is described by *carrier density fluctuations*, whereas the $1/f$ noise in metals is attributed to *carrier mobility fluctuations*. As graphene behaves as a semi-metal or zero-gap semiconductor, the $1/f$ noise mechanism can be dictated by carrier density and/or mobility fluctuations [136–138]. The carriers in graphene are subject to trapping from charge impurities in the substrate and/or dopant's attaching to the top surface, which can result in carrier density fluctuations [139]. It has been reported that samples with car-

rier mobilities on the order of 10^3-10^4 cm^2/Vs are the result of long-range, in-plane, Coulomb scattering [133, 140]. Furthermore, the scattering centres in substrate and/or surface can also result in carrier mobility fluctuations [141]. However, carrier density and mobility measurements on the devices presented in Section 3.2 showed no significant cross size dependence. The fact that miniaturisation of the Hall bar device does not significantly affect the carrier density and mobility, increase in $1/f$ noise is largely related to unoptimised device design (Fig. 3.5).

3.4 A comparison with semiconductor devices

Comparing the properties of $\sim 5\,\mu m$ wide EG Hall sensors against those of identical width made out of 300 nm thick InSb epilayers [142–144] under similar measurement conditions (Table 3.1), R_4 and R_H are comparable, while n is an order of magnitude higher and μ is approximately 3 times lower for EG. However, the B_{min} and λ are comparable, indicating that the overall performance of graphene sensors is comparable to that of well-established state-of-the-art InSb sensors. The same cannot be said for CVD graphene [97], which exhibits a lower R_H due to a ten times larger carrier density. Furthermore, B_{min} is order of magnitude higher at a third of the applied I_{bias} compared to EG and InSb devices. The higher B_{min} is the result of a larger noise floor of CVD graphene, thus indicating to a significantly lower carrier mobility (not specified). On the other hand, miniaturising EG sensors down to 600 nm has little effect on the carrier density. However, an increase in the channel resistance ultimately results in larger $1/f$ noise, thus degrading B_{min} by a factor of ~ 3.5. In comparison, the 600 nm wide InSb device retains the material properties, thus resulting in no real

Size [Material] (μm)	R_4 ($k\Omega$)	R_H (Ω/T)	n ($10^{11}\,cm^{-2}$)	μ (cm^2/Vs)	B_{min} [I_{bias}] ($\mu T/\sqrt{Hz}$) [μA]	λ (nm)
0.6 [EG]	29	890	7.1	2415	13.8 [10]	24.4
0.6 [InSb]	9	1,106	1.2	13,000	5.4 [5]	52.5
4.6 [EG]	22	711	8.8	2,643	3.9 [10]	28.5
5.0 [InSb]	12	974	0.87	8,322	6.5 [10]	27.4
5.0 [CVD]	–	310	20	–	43.0 [3]	–

Table 3.1: A summary of data for devices made out of epitaxial graphene, InSb [142–144] and CVD graphene [97].

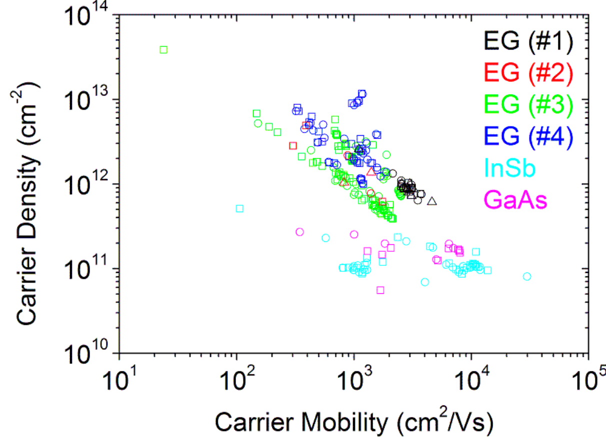

Figure 3.6: A compilation of carrier density and carrier mobility measurements for epitaxial graphene, InSb and GaAs devices.

performance degradation. InSb is a well-established material benefiting from over half a century of research and development [145], whereas graphene was discovered merely a decade ago. All the measurements of carrier density and carrier mobility at room temperature, in ambient conditions, for EG, InSb and GaAs 2DEG devices of similar shape, size are shown in Fig. 3.6. The data points relating to the graphene devices are typically of higher carrier density than InSb and GaAs devices, reaching up to two orders of magnitude larger. However, the largest mobility for graphene reported here is $\mu \sim 4600\, cm^2/Vs$, whereas the GaAs has been shown to reach $\mu \sim 8000\, cm^2/Vs$ and InSb $\mu \sim 30,000\, cm^2/Vs$.

3.5 Single magnetic bead detection

The performance of EG sensor was also tested by detecting the stray field of a single superparamagnetic microbead, where a significant amount of research had previously been carried out with semiconductor sensors for biomedical applications [128, 142, 146–149]. Research in this particular field has shown that semiconductor Hall sensors with their rather simple measurement circuit have offered excellent magnetic field sensitivity ($B_{min} \sim 0.2\ \mu T/\sqrt{Hz}$) at room temperature [128, 148]. Coupled with high spatial resolution of sub-micron scale Hall sensors, these features makes them ideal for detection of nanobeads [142].

3.5.1 Placement of a single Dynal bead

The bead detection experiment was carried out on a modified 1.6 μm wide device (#1a) from sample #1. The modification involved placing a commercially available 1 μm diameter Dynal (MyOne) bead with $m \sim 4 \times 10^8\ \mu_B$. The bead is constructed from a polymer matrix containing 37% ferrite with total Fe concentration of $\sim$ 26%. A single bead was placed on cross 1 using an FEI Nova Nanolab Duel Beam focused ion beam (FIB), equipped with a Zyvex nanomanipulation system.

The beads are originally dispersed in distilled water at a high concentration. The diluted concentration is then drop-cast dispersed on a Si/SiO_2 substrate (Fig. 3.7a). Using electron beam imaging (5 kV), a single bead is located from the sea of beads and weakly attach to a pre-sharpened single carbon fibre strand using a short burst of methylcyclopentadienyl-trimethyl-platinum (standard e-beam Pt deposition). The bead is then gently positioned on cross 1 and held in place by using a short burst of the Pt deposition. After securing the bead on cross 1, the carbon fibre strand is withdrawn (Fig. 3.7b). The magnification was kept as low as possible throughout the manoeuvre, minimising the exposure of the graphene device to e-beam irradiation. However, the estimated dose of e-beam irradiation was $> 4 \times 10^{14}\ e/cm^2$. Cross 2 received a dose of $\sim 4 \times 10^{14}\ e/cm^2$ and Pt deposition so that their combined effects on transport properties could also be investigated. Cross 3 received a negligible e-beam exposure, maintaining a pristine condition.

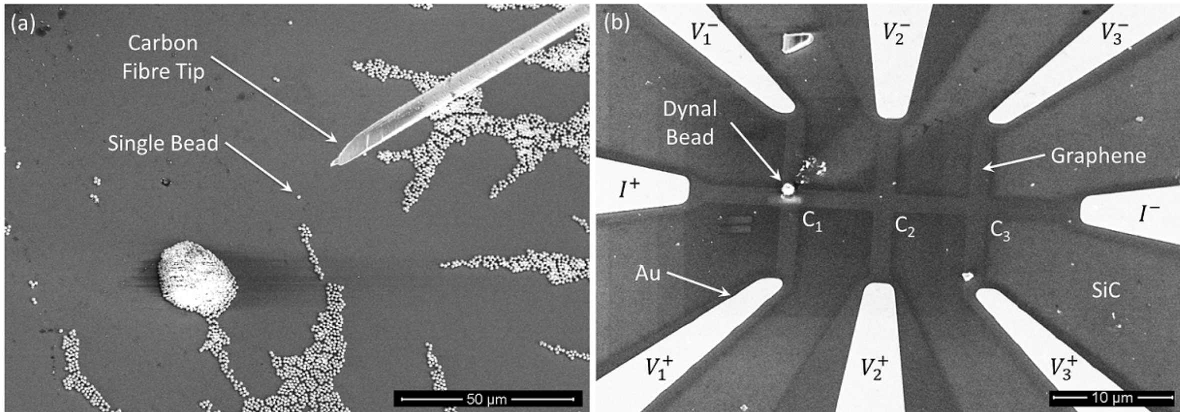

Figure 3.7: Scanning electron micrograph images showing (a) puddles of Dynal MyOne beads and (b) device #1a with a 1 μm diameter Dynal bead attached to cross 1. C_1, C_2 and C_3 denote Crosses 1, 2 and 3, respectively.

3.5.2 Experimental method

The detection of the magnetic bead was carried out using a constant AC ($B_{AC} = 3mT$ at frequency $f = 210Hz$) and pulsed DC ($B_{DC} = 250mT$) magnetic fields that are perpendicular to the device (Fig. 3.8). The B_{AC} is produced by a miniature coil (with an inner diameter $\sim 2\,cm$, inductance $L = 5.87\,mH$ and resistance $R = 16.1\,\Omega$, driven by an Agilent Technologies 33120A arbitrary waveform generator), placed beneath the sample, whereas B_{DC} was produced by the electromagnet used during the transport measurements (Section 3.2, Fig. 3.1b). The device was current biased at $I_{bias} = 50\,\mu A$, while the AC Hall voltage (V^{AC}) response of all three crosses was simultaneously measured at the first harmonic using lock-in amplifiers (Stanford Research Systems SR830) referenced to the B_{AC} drive signal. The lock-in amplifiers measure the in-phase (V_x^{AC}) and out-of-phase (V_y^{AC}) components of the AC signal, effectively separating the real and parasitic signals.

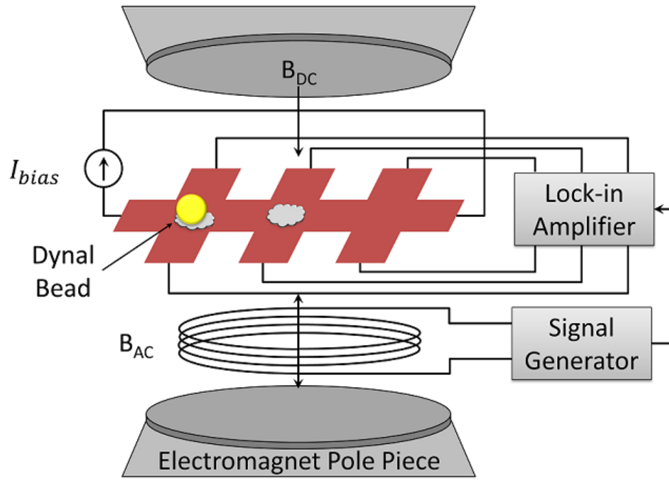

Figure 3.8: (a) Schematic of the bead detection experimental setup showing the arrangements of the device and AC/DC magnetic fields.

3.5.3 Bead detection

The experiment was carried out by continuously measuring V^{AC} with the lock-in amplifiers set to 1 second time constant, while the device was current biased at $I_{bias} = 50\,\mu A$. During the measurement, three separate pulses of the B_{DC} from $B_{DC}^0 = 0$ (60 seconds duration) to $B_{DC}^1 = 250\,mT$ (30 seconds duration) were applied. Fig. 3.9a and Fig. 3.9b shows the response of V_x^{AC} and V_y^{AC}, respectively, for all three crosses, normalised against the parasitic capacitance signal, *i.e.*, $\Delta V^{AC} = V^{AC}(I_{bias}) - V^{AC}(0)$. The results show a distinctive step wise change of $V_x^{AC}(B_{DC}^1) - V_x^{AC}(B_{DC}^0) \sim 7\,\mu V$ for

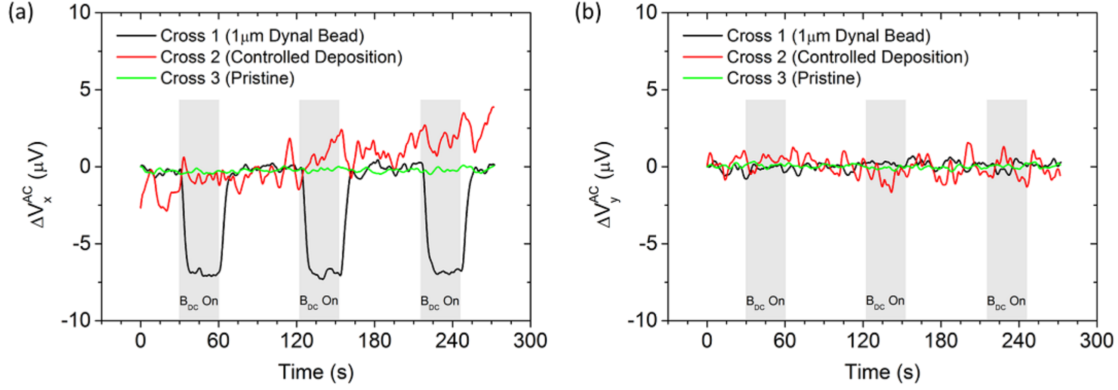

Figure 3.9: Response of (a) in-phase (V_x^{AC}) and (b) out-of-phase (V_y^{AC}) components of the AC Hall voltage to three separate B_{DC} pulses with a duration of 30 seconds, normalised against the background signal, *i.e.*, $\Delta V^{AC} = V^{AC}(I_{bias}) - V^{AC}(0)$. The device was current biased at $I_{bias} = 50\,\mu A$, $B_{DC} \sim 250\,mT$ and $B_{AC} \sim 3\,mT$ at $f = 210\,Hz$.

cross 1 correlating to the B_{DC} pulses, whereas crosses 2 and 3 shows no response (Fig. 3.9a). The distinctive step is a clear indication to the presence of a magnetic particle on cross 1. Furthermore, the signal from cross 2 shows a significant increase in the electrical noise ($\sim 3\,\mu V$), which could be a consequence of damage to the graphene from Pt deposition and e-beam irradiation. In comparison to the signal from crosses 1 and 3, the electrical noise was lower by an order of magnitude ($\sim 0.4\,\mu V$). The measurements of ΔV_y^{AC} on all three crosses show no response to the B_{DC} pulses, however cross 2 maintained the higher level of noise.

The experimental results can be compared to the theoretical model, which describes the change in V_x^{AC} as

$$V_x^{AC}(B_{DC}^1) - V_x^{AC}(B_{DC}^0) = I_{bias} R_H c[\chi(B_{DC}^1) - \chi(B_{DC}^0)] B_{AC}, \tag{3.6}$$

where the bead-sensor coupling constant was numerically calculated as $c_{graphene} \sim 0.045$ (Appendix B) and χ is the magnetic susceptibility of the Dynal beads. Using the susceptibility measurements performed on an ensemble of Dynal beads [144], $\chi(B_{DC}^1) - \chi(B_{DC}^0) \sim 0.012$ was estimated for a single bead. Using the transport measurement technique described in Section 3.2, the sensitivity of cross 1 was determined as $R_H = 408\,\Omega/T$, estimating a change of $V_x^{AC} \sim 16\,\mu V$ due to the presence of a single Dynal bead at $B_{DC}^1 = 250\,mT$. The discrepancy between the measured and estimated value

of V^{AC} could be largely related to the fact that the susceptibility measurements were performed on an ensemble of Dynal beads, from which the value was extrapolated for a single bead.

In comparison to measurements performed on 1 μm wide Hall sensor fabricated out of undoped InSb 300 nm thick film ($R_H = 262\,\Omega/T$ and $\mu = 1.3\,m^2/Vs$) with identical Dynal bead, a significantly lower response of $\sim 500\,nV$ was achieved at $I_{bias} = 1\,\mu A$. The lower response is largely related to a significantly lower maximum bias current limit of $I_{bias} = 5\,\mu A$, whereas the effective electron-lattice interactions in graphene lead to a significantly higher carrier energy loss rate [150, 151], giving it higher stability to larger biasing currents of $I_{bias} \sim 1\,mA$ [152]. Furthermore, the relatively large thickness of the InSb film results in the detection taking place from 0-300 nm below the surface of the material, whereas the detection occurs only at the surface of the graphene sheet, leading to a 30% decrease in the vertical coupling. Despite this, the total bead-sensor coupling for InSb is $c_{InSb} = 0.09$ [144] and for graphene in the present experimental setup is $c_{graphene} = 0.045$. The coupling for graphene is twice as small due to ~ 2.5 times increase in the sensor area.

3.6 Summary

In summary, EG Hall sensors with the size ranging from 0.1-19.6 μm were successfully fabricated. Using transport and noise measurements, it has been shown that the strongly diffusive EG sensors that are ≤ 5 μm wide are typically less sensitive to magnetic fields than their larger counterparts due to an inherently higher R_2, which ultimately results in larger contribution from the $1/f$ noise at $I_{bias} > 0$. The $1/f$ noise can be reduced by shortening and widening the long and narrow voltage leads, significantly reducing the length of the narrowest part of the graphene in the circuit. The cross size dependence of B_{min} clearly signifies the importance of unoptimised design to the performance of the devices. The R_H of EG sensors are approaching that of the ones fabricated out of state-of-the-art 300 nm thick InSb epilayer. In comparison to CVD graphene however, the EG sensors offer lower resistivity and an order of magnitude better magnetic field sensitivity.

Furthermore, the performance of a 1.6 μm wide EG Hall sensor was tested by detecting a single Dynal bead that was accurately placed using nanomanipulation system within a FIB. The bead was reliably detected using an AC/DC Hall magnetometry technique, with a relatively large response of $\sim 7\,\mu V$. The large response is primarily related to robustness of graphene devices to large biasing currents as well as improved bead-sensor coupling in the vertical direction. This demonstrates a significant improvement in the performance of graphene device when compared to identical measurements performed on an InSb device.

Chapter 4

Scanning probe microscopy techniques for nanoscale investigations

This chapter provides a detailed description of all the SPM techniques used to study EG devices. Starting with AFM; the technique operates on the interatomic van der Waals forces to determine the topography, forming the basis for all the SPM techniques described in this chapter. The electrical properties of the graphene were studied using surface potential measurement techniques such as electrostatic force microscopy (EFM), EFS and KPFM. Furthermore, a description of SGM, a technique that measures the response of a device to a local electric or magnetic gate, has also been presented. All the measurements were carried out on a Bruker Dimension Icon SPM [153] using Bruker probes (Table 4.1) [154].

Probe	Coating (Thickness) (nm)	Apex Diameter (nm)	Spring Constant (N/m)	f_0 (kHz)
SCM-PIT	Pt-Ir (~ 20)	~ 20	~ 2.8	~ 75
PFQNE-AL	Uncoated Si	~ 5	~ 0.8	~ 300
MESP	Co-Cr (~ 50)†	~ 35	~ 2.8	~ 75
MESP-HM	Co-Cr (~ 150)‡	~ 80	~ 2.8	~ 75
DNP-10	Uncoated Si_3N_4	~ 20	~ 0.2	

Table 4.1: A summary of Bruker SPM probes used throughout the thesis. Note: †Coercivity $\sim 400\,Oe$ and moment $\sim 1 \times 10^{-13}\,emu$. ‡Coercivity $\sim 400\,Oe$ and moment $> 3 \times 10^{-13}\,emu$. DNP-10 are probes for CM-AFM cleaning (Appendix C).

4.1 Atomic force microscopy

Majority of the SPM techniques are based on the AFM, which exploits the van der Waals forces between the sample and the probe to obtain topographic information. The probe is generally in the shape of a pyramid or cone with the apex on the order of 1-30 nm in radius. The probe is attached to the end of a silicon or silicon nitride cantilever with mechanical resonance frequency of $f_0 \sim$ 50-350 kHz. For simplicity, the probe and cantilever will be simply referred to as the "probe". The probe is placed in a holder containing a small dithering piezoelectric material, who's sole purpose is to mechanically oscillate the cantilever. The holder is than attached to the piezoelectric tube that performs x, y and z movements dictated by the AFM feedback loop with the task of maintaining the specified deflection set point of the cantilever, governed by either positive or negative (repulsive or attractive) force, respectively. In most AFM systems, deflection is measured using a precisely adjusted laser reflecting from the top side of the cantilever and onto a four-quadrant position sensitive detector (PSD). A 2-dimensional topographic map of the sample is recorded by scanning the area with x and y movements of the piezoelectric tube, while also performing z movements to maintain the deflection set point.

Contact and tapping mode AFM are two of the most widely used techniques. Both modes exploit the repulsive regime of the van der Waals forces, *i.e.*, maintaining a positive deflection set point by applying and recording the z movements of the piezoelectric tube. However, as the name suggests, tapping mode is performed with the cantilever oscillating close to f_0. Tapping mode not only provides topographic information, the

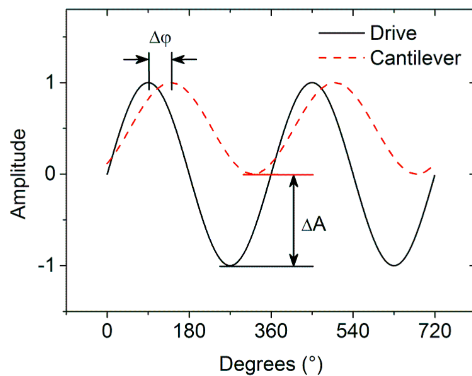

Figure 4.1: Plot showing the phase shift and amplitude of the cantilever relative to the drive signal as a result of energy dissipation from when the probe contacts the sample.

forces between the probe and the sample will also maintain the resonance frequency, oscillation amplitude (A_{osc}) and phase (φ) of the cantilever. Recording parameters such as φ and A_{osc} with respect to the drive signal are known as topography phase imaging (Fig. 4.1). The amplitude and phase shift arise due to the energy dissipation from when the probe contacts the sample, providing mechanical (a convolution of adhesion, composition, friction and viscoelasticity) and electrical information of the sample.

4.2 Electrostatic force microscopy

EFM probes the electrostatic interactions between the electrically conductive probe and the sample. The two-pass technique performs AFM and EFM line scans in an alternating manner, line-by-line, to build-up an image (Fig. 4.2a). Tapping mode AFM is first performed to determine the surface topography (Fig. 4.2b). EFM then retraces the surface topography at a set lift height from the surface (25 nm unless stated otherwise), driving the cantilever near f_0 with a DC bias voltage (V_{probe}) applied to the probe with respect to the sample. The sample is connected to the stage, which is common ground of the microscope, using wire bonding. The potential difference between the sample and the probe generates an electric field (Fig. 4.3), with the electrostatic force, $F_{DC} = -\frac{1}{2}\frac{dC}{dz}\Delta V^2$, where C and z are the capacitance and distance, respectively [126, 155, 156]. The voltage (ΔV) is the sum of the contact potential difference (V_{CPD}), the applied DC voltage to the probe and all other externally induced

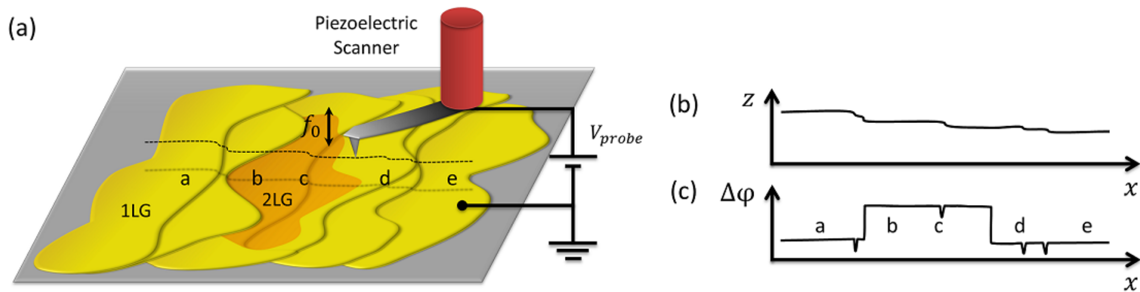

Figure 4.2: (a) EFM experimental setup showing tapping mode AFM to determine (b) the sample topography. (c) EFM performed by retracing the sample topography at a set lift height from the sample to determine the phase shift. The EFM is performed with the cantilever driven near the mechanical resonance with a DC bias voltage applied to the probe, with respect to the grounded sample.

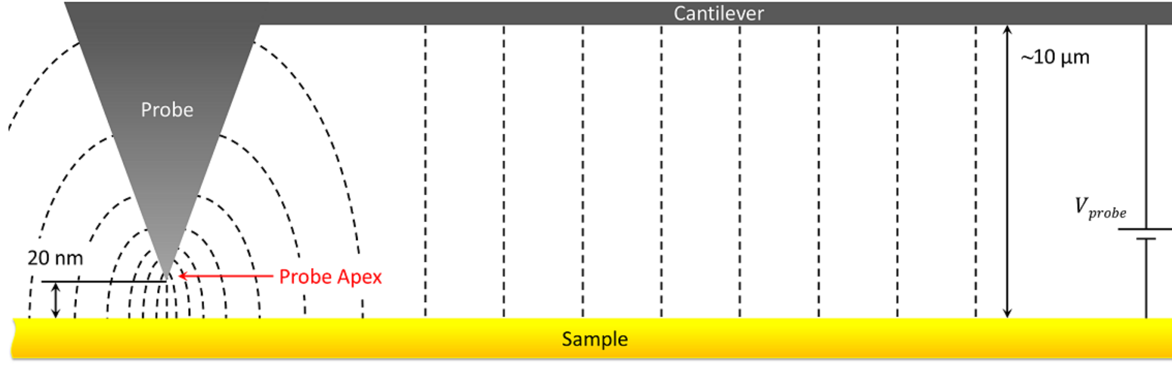

Figure 4.3: A schematic of the probe-sample electrostatic force. Note: image not to scale.

DC voltages ($V_{induced}$); $\Delta V = V_{probe} - (V_{CPD} + V_{induced})$. The force related to only DC voltages that deflect the cantilever is given by

$$F_{DC} = -\frac{1}{2}\frac{dC}{dz}\left[V_{probe} - (V_{CPD} + V_{induced})\right]^2. \tag{4.1}$$

The electrostatic forces related to DC voltages act as a second-order effect on the mechanical oscillation of the cantilever, affecting the A_{osc}, f_0 and φ that are detected using a lock-in amplifier. The EFM image is generated by recording the phase change

$$\Delta\varphi = -\frac{Q}{k}\frac{dF_{DC}}{dz} = -\frac{Q}{2k}\left(\frac{d^2C}{dz^2}\right)\left[V_{probe} - (V_{CPD} + V_{induced})\right]^2, \tag{4.2}$$

where k and Q are the spring constant and quality factor of the cantilever, respectively (Fig. 4.2c). $\Delta\varphi$ is effectively a *qualitative* measurement of the force gradient ($^{dF_{DC}}/_{dz}$), which is largest at the probe apex (Fig. 4.3). Therefore, spatial resolution with EFM is approximately that of the probe apex diameter (Table 4.1).

4.3 Surface potential measurements

4.3.1 Electrostatic force spectroscopy

EFS, an innovative modification to EFM, can provide *quantitative* measurements of the V_{CPD}. Unlike EFM, which provides a 2D map of the sample, EFS is typically performed at well-defined stationary points. The separated charges that result from work function differences between the probe and the sample (Fig. 4.4a) generate a

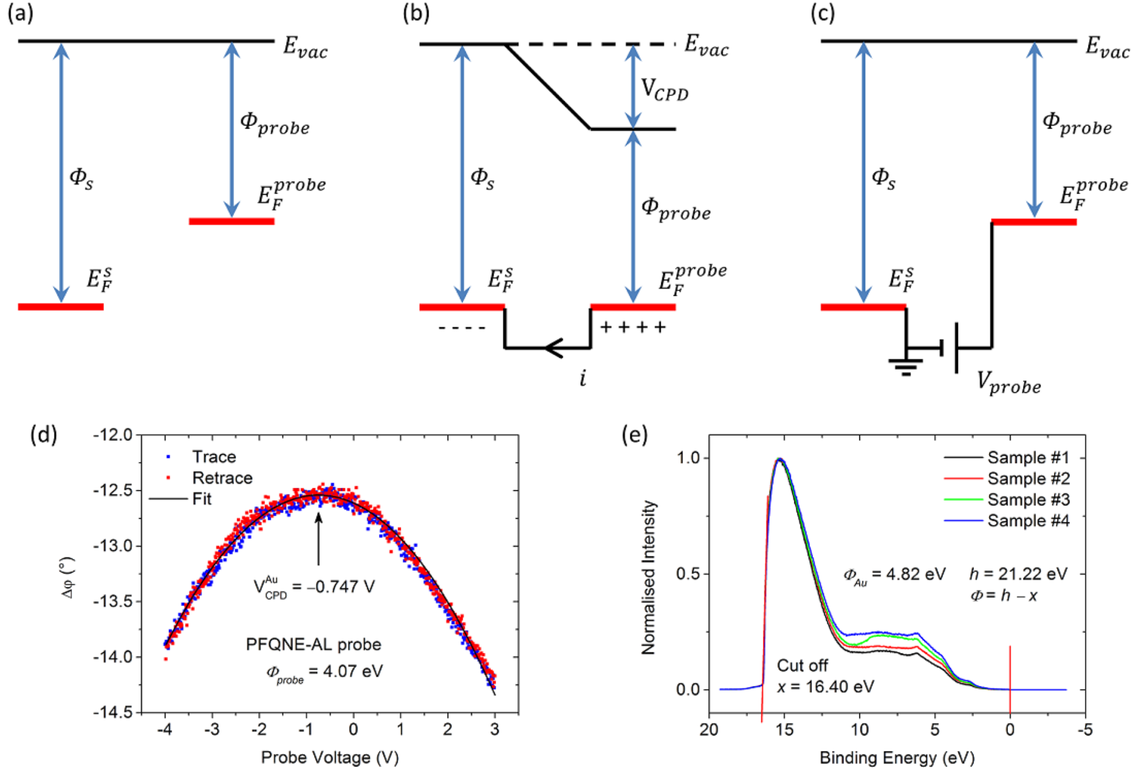

Figure 4.4: Energy level scheme for the Au sample and PFQNE-AL probe when they are (a) electrically isolated, (b) electrically connected and (c) V_{probe} applied to nullify the V_{CPD}. E_{vac} is the vacuum energy level. E_F^{probe} and E_F^s are Fermi energy levels of the probe and sample, respectively. Adapted from Ref. [126]. (d) EFS measurement on Au to calibrate the work function for a PFQNE-AL probe. Blue and red curves represent the forward (trace) and reverse (retrace) sweep of V_{probe} and the arrow points to the inflection point, where $F_{DC} = 0$. (e) UPS measurement showing the binding energy curve for Au, where h and x are the energy of the incident photon and the cut off binding energy, respectively.

V_{CPD} when the probe and sample are in electrical contact (Fig. 4.4b), thus, resulting in attractive/repulsive forces on the cantilever. Applying $V_{probe} = V_{CPD}$ balances the forces, *i.e.*, $F_{DC} = 0$ (Fig. 4.4c). The ΔV^2 term in Eq. 4.2 gives rise to a parabolic response, which is easily detectable by recording the $\Delta\varphi$, while sweeping the V_{probe} from, *i.e.*, –3 to $+3V$ with millivolt resolution (Fig. 4.4d) [157]. The inflection point of the parabola constitutes the point at which $V_{probe} = V_{CPD}$, providing a quantitative measure of the V_{CPD} from $\Delta\varphi$ measurement.

EFS can be used to determine the work function of the sample (Φ_{sample}) by first calibrating the work function of the probe (Φ_{probe}) against a known quantity such as Au (Φ_{Au}) using $\Phi_{probe} \approx \Phi_{Au} + eV_{CPD}$ [126], where $\Phi_{Au} = 4.82\ eV$ was determined using ultraviolet photoelectron spectroscopy (UPS) measurements conducted in UHV

(Fig. 4.4e). It should be noted that some uncertainty in Φ_{Au} may arise from reversible adsorption of gasses and water, which can form surface dipoles when transferring the sample from UHV to ambient air. However, Au is less prone to oxidation and formation of a submonolayer of water, making it more stable than most other good conductors. Surface potential studies on water adsorption behaviour of metal surfaces shows that Φ_{Au} may decrease by $\sim 3\%$ as relative humidity changes from 0-40% [158]. Therefore Au remains one of the best electrode material that is also stable in ambient air. Using Au as a reference, the work function of PFQNE-AL probe was determined as $\Phi_{probe} = 4.07\,eV$ (Fig. 4.4d) and SCM-PIT probe was determined as $\Phi_{probe} = 4.99\,eV$. The Φ_{sample} can then be measured by using $\Phi_{sample} \approx \Phi_{probe} - eV_{CPD}$.

Analysis of hundreds of EFS measurements were made practical by post processing the raw data using a script-based programming language such as MATLAB that fits each parabola and extracting the V_{CPD}. EFS data acquisition is performed at a rate of 1 second per curve, therefore a 2D map of 512×512 pixels with single EFS measurement at each pixel would typically require over 70 hours, making it hugely impractical. In comparison to EFM, an image with the same number of points will only require ~ 30 minutes. However, the quantitative nature of EFS makes it a more useful technique over EFM, while retaining the spatial resolution of the probe apex diameter. Moreover, EFS also benefits from improved accuracy of the V_{CPD} measurement, where the force gradient between the cantilever and sample is negligible in comparison to the probe apex (Fig. 4.3).

4.3.2 Amplitude-modulated Kelvin probe force microscopy

AM-KPFM is one of the most established non-invasive V_{CPD} mapping techniques that can be performed as a single- or double-pass. The single-pass technique operates at the first and second mechanical resonances of the cantilever to determine the topography and V_{CPD}, respectively. However, the Bruker Icon system was operated as a double-pass technique (Fig. 4.5a), where the first pass measures the sample topography (Fig. 4.5b) and second pass measures the V_{CPD} in lift mode. The second pass is performed with the mechanical drive of the cantilever turned off, but instead, an AC voltage ($V_{mod} \sim 2\,V$ at f_0) is applied to the probe. When $V_{probe} \neq V_{CPD} + V_{induced}$, the AC component

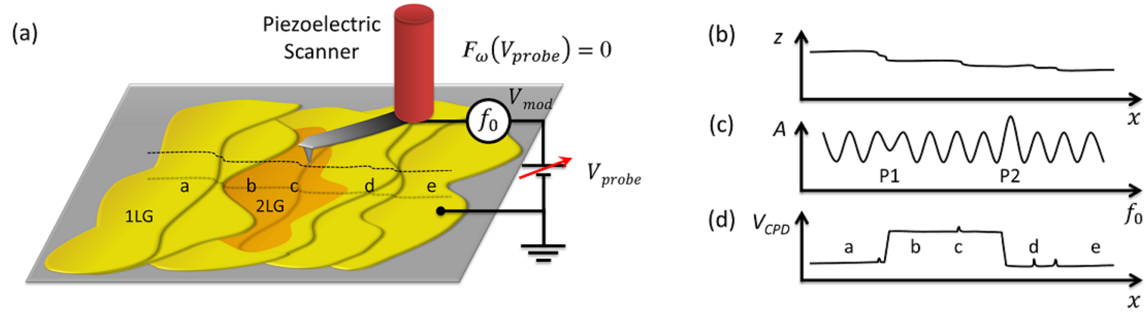

Figure 4.5: (a) AM-KPFM experimental setup showing tapping mode AFM to determine (b) the sample topography and (c) AM-KPFM performed by retracing the sample topography at a set lift height from the sample with the cantilever not mechanically driven at f_0, however, V_{mod} is applied at f_0, thus inducing mechanical oscillations. (d) The V_{CPD} is determined by using a feedback to applying V_{probe} such that F_ω is minimised. Note: $V_{probe} \neq V_{CPD} + V_{induced}$ at P1 and P2 in (c).

induces an oscillatory force on the cantilever (Fig. 4.5c) at the first (F_ω) and second ($F_{2\omega}$) harmonic, described by

$$F_\omega = -\frac{1}{2}\frac{dC}{dz}[(V_{probe} - (V_{CPD} + V_{induced})) + V_{mod}\sin(\omega t)]^2, \tag{4.3}$$

and

$$F_{2\omega} = \frac{1}{4}\frac{dC}{dz}V_{mod}^2\cos(2\omega t), \tag{4.4}$$

where $\omega = 2f_0$ [126], making it a *force* sensitive technique. The AM-KPFM technique measures the V_{CPD} by using a feedback loop to apply and record V_{probe} such that F_ω is minimised (Fig. 4.5d). The second harmonic mode is not utilised by AM-KPFM as it probes the capacitance effect. The cantilever oscillations are detected by the PSD, and thus AM-KPFM is best performed using soft cantilevers that are capable of oscillating at large amplitudes, increasing the signal to noise ratio. Unlike EFS, a 2D map of the V_{CPD} can be obtained with AM-KPFM. However, the large area of the cantilever results in a strong parasitic capacitance effect (Fig. 4.3), which leads to a relatively poor spatial resolution of 50-70 nm and can also affect the accuracy of the V_{CPD} measurement on samples with non-uniform electronic properties.

4.3.3 Frequency-modulated Kelvin probe force microscopy

FM-KPFM is a V_{CPD} measurement technique that operates on the *force gradient* (dF_ω/dz) by detecting the shift in the mechanical resonant frequency of the cantilever (Fig. 4.6a) [159]. FM-KPFM can also be performed as a single- or double-pass technique. The single-pass technique determines the sample topography with tapping mode AFM at f_0 (Fig. 4.6b) and a simultaneous lower frequency ($f_{mod} \sim$ 2-8kHz) AC voltage ($V_{mod} \sim$ 2-10 V) applied to the probe induces a frequency shift of [160]

$$f_0 \pm f_{mod} \approx f_0 \left(1 - \frac{1}{2k}\frac{dF_\omega}{dz}\right), \tag{4.5}$$

when $V_{probe} \neq V_{CPD} + V_{induced}$ (Fig. 4.6c). The V_{CPD} (Fig. 4.6d) is determined by using a feedback loop that monitors the side lobes at $f_0 \pm f_{mod}$ (Fig. 4.6e) and minimises

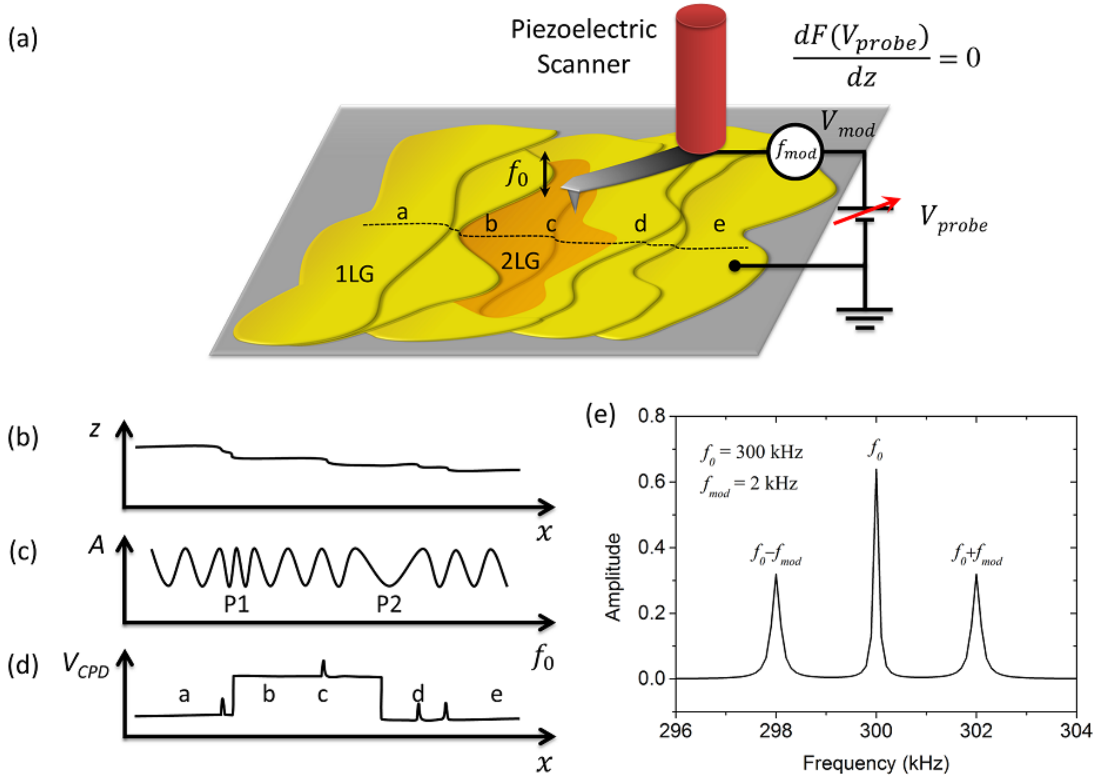

Figure 4.6: (a) FM-KPFM experimental setup showing tapping mode AFM to determine (b) the sample topography. (c) The simultaneous low frequency AC voltage applied to the probe shifts the f_0 of the cantilever, to determine (d) the V_{CPD}. (e) The V_{CPD} is determined by using a feedback loop that minimises the side lobes at $f_0 \pm f_{mod}$. Note: $V_{probe} \neq V_{CPD} + V_{induced}$ at P1 and P2 in (c).

them by applying and recording V_{probe}. With the double-pass FM-KPFM, the first pass simply determines the topography. The second pass essentially involves performing single-pass FM-KPFM. However as the topography is already known, the probe is retraced at a set lift height from the surface. While the *in situ* measurement using single-pass technique can be affected by the cross-talk between the topography and V_{CPD}, the double-pass technique is not affected as the two are determined separately. FM-KPFM is best performed using stiff cantilevers with high f_0. The consequence of the short range detection of the force gradient has a major benefit in that, it is highly localised to the probe apex, thus, providing V_{CPD} map with accuracy and high spatial resolution [126].

4.4 Electrical and magnetic scanning gate techniques

SGM operating on the field gradient is a technique that is essentially identical to EFM in the sense that the first pass measures the sample topography in tapping mode at f_0 and second pass retraces the topography at a set lift height. During the second pass the probe is mechanically oscillated at f_0, therefore when using a DC voltage biased (V_{probe}) electrically conductive probe produces a modulated electric field (dE/dz). In the case of using probes such as MESP or MESP-HM, which are coated with a magnetic material (Table 4.1), a modulating magnetic field (dB/dz) is produced. The contrast between EFM and SGM is that, with EFM, the $\Delta\varphi$ of the cantilever is recorded to produce the image, while with SGM, *in situ* transport measurements are performed using a lock-in amplifier (Stanford Research Systems SR830) on the current biased (I_{bias}) device (Fig. 4.7a). These measurements are fed back into the microscope in synchronous, producing a 2-dimensional map of the voltage response of the device to a field gradient [118, 161, 162]. Using electrical SGM, the longitudinal (V_{xx}) or transverse voltage (V_{xy}) can be recorded at each pixel with an external lock-in amplifier referenced to f_0 of the cantilever, thus producing a map of dV_{xx}/dz response of the channel or dV_{xy}/dz response of the Hall cross, respectively. Using magnetic SGM, dV_{xy}/dz map of the Hall cross is in response to the Lorentz force acting on the charged carriers in the material.

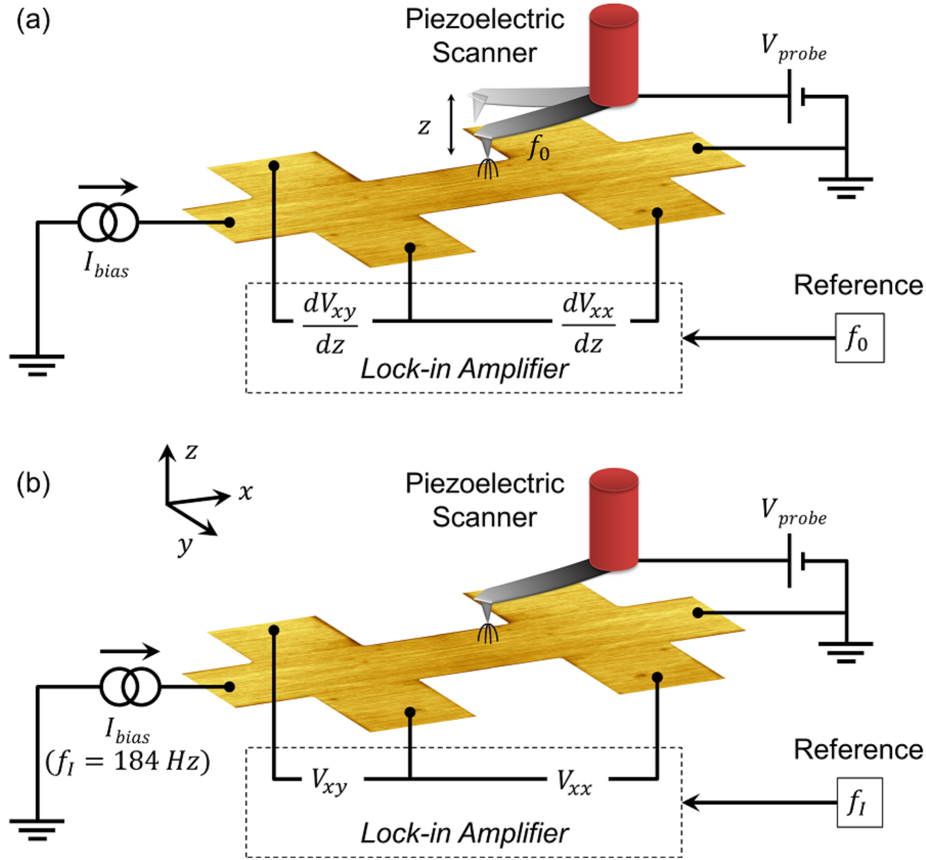

Figure 4.7: SGM schematic showing a probe locally gating a Hall device, while an external lock-in amplifier measures (a) dV_{xx}/dz or V_{xy}/dz in response to a field gradient and (b) V_{xx} or V_{xy} in response to a field, which are fed back into the microscope and recorded at each pixel to produce a 2D map.

SGM operating on the field is similar to the SGM operating on the field gradient in the sense that both are two-pass techniques. The main difference lies in the second pass, where the mechanical oscillation of the probe is disabled, resulting in a non-modulated field (Fig. 4.7b). However, an AC bias current was applied at low frequency (f_I = 184 Hz) to accurately measure the response of the device with the lock-in amplifier. The use of low frequency is essential for avoiding any adverse effects from the inductance of the device, therefore the response of the device to the field can be regarded as purely DC.

SGS can also be performed with both SGM techniques by fixing the x-y position of the probe and measuring the device response to the V_{probe} sweep.

Chapter 5

Nanoscale mapping of devices

Epitaxially grown graphene on $4H$-SiC(0001) typically contains non-uniform number of layer thicknesses. Where bulk transport measurements only provide an average statistics of the material, surface potential mapping techniques quantitatively reveal the changes between differing layer thicknesses. However, each surface potential measurement technique can reveal contradicting results due to their subtle differences in the modes of operation (Section 4.3). This chapter provides a comprehensive comparison of the accuracy of three most widely used surface potential measurement techniques. The most accurate technique(s) were then employed to study in detail various aspects of EG devices. These involve work function measurements of 1LG, 2LG and edge effects. Furthermore, complementary transport measurements were also performed to study the contact resistance between the graphene and Au contact leads, effects of environmental and substrate doping on 1LG and effects of 2LG islands on bulk transport properties.

5.1 Nanoscale mapping with SPM techniques

AFM is the basis for all of the SPM techniques described in Chapter 4. For example, EFM and AM-KPFM techniques rely on knowing the exact surface topography to maintain a constant probe-sample distance during the second pass. Although FM-KPFM is a single-pass technique, simultaneous tracking of the surface topography by AFM is still required. In this section, AFM, EFM, AM-KPFM and FM-KPFM techniques are applied using a PFQNE-AL probe to study a 4.8 μm wide EG device (#2a). The

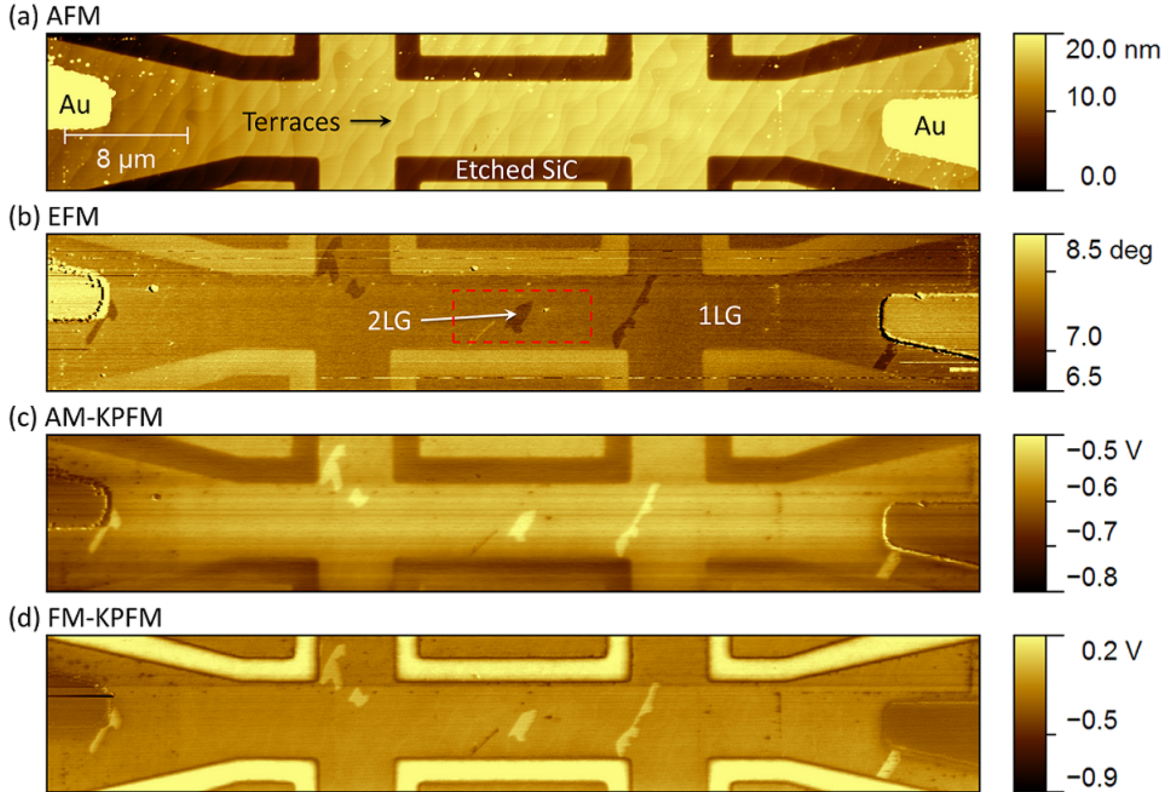

Figure 5.1: Mapping of the 4.8 μm wide EG device (#2a) with (a) AFM, (b) EFM at $V_{probe} = -1.5\,V$ and 40 nm lift height, (c) AM-KPFM and (d) FM-KPFM. Au signifies the gold leads, Etched SiC is where the graphene has been etched to form a trench, 1LG and 2LG are single- and double-layer graphene, respectively.

device was fabricated out of sample #2 using same method as for sample #1 (Appendix A). However, this device contains only two crosses, surrounded by isolated planes of graphene, which can be used as lateral gates. The sample topography of device #2a is shown in Fig. 5.1a. The Cr/Au ($\sim 100\,nm$ thick) contact leads, labelled Au, show up as bright yellow due to their relatively large thickness. The wave like features are the edges of the nanometre scale steps (terraces) in the SiC substrate. The terraces are on average $\sim 0.5\,nm$ high and can be as thin as a single SiC layer (0.25 nm). In the present sample, the terraces are formed from the initial miscut of the substrate (0.11^{o}), however, the high temperature EG growth process sublimes the Si from the substrate, causing the steps to bunch together to form terraces with widths of $\sim 1\,\mu m$. The dark areas of the map are trenches etched into the SiC to effectively form the device.

Identifying domains of different graphene layer thickness is generally very difficult from AFM images due to the complicated surface topography of SiC. However, EFM

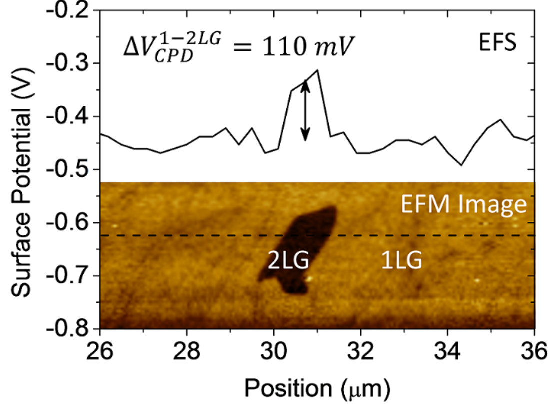

Figure 5.2: Top: V_{CPD} measurement of 1LG and 2LG with EFS. Bottom: Zoomed EFM image showing only the central 2LG from Fig. 5.1b indicated by the dashed red box. EFS measurements were conducted along the indicated dashed line.

phase imaging probes the electrostatic forces (Section 4.2), which can be used to identify domains of different graphene layer thickness due to their inherently unique electrical properties. An EFM phase image was obtained for the same area of device #2a at $V_{probe} = -1.5\ V$ and 40 nm lift height, while keeping the entire device grounded to define the potential (Fig. 5.1b). In contrast to the surface topography, EFM image reveals randomly shaped features that are in fact 2LG islands ($\Delta\varphi = 7.4^{\text{o}}$) and confirms that 1LG grows continuously over the terraces ($\Delta\varphi = 7.6^{\text{o}}$). Despite the clear contrast between 1LG and 2LG, EFM alone cannot be used to definitively identify the domains of different graphene layer thickness, making it a *qualitative* technique. However, by performing EFS at a well-defined point (Section 4.3.1), *i.e.*, measuring $\Delta\varphi$ as a function of V_{probe}, the V_{CPD} can be determined by fitting the parabolic response and extracting V_{probe} at which $d\varphi/dV_{probe} = 0$ (*i.e.*, the inflection point), providing *quantitative* measurement of the surface potential. EFS measurements were performed along the dashed line indicated in the bottom EFM image of Fig. 5.2 and the V_{CPD} of 1LG and 2LG was determined as $V_{CPD}^{1LG} \sim -442\,mV$ and $V_{CPD}^{2LG} \sim -332\,mV$, respectively, giving an absolute difference of $\Delta V_{CPD}^{1-2LG} \sim 110\,mV$ (Fig. 5.2).

AM-KPFM is a mapping technique that providing quantitative information by directly measuring the V_{CPD} (Section 4.3.2). The V_{CPD} measurement performed over the same area of device #2a with AM-KPFM is shown in Fig. 5.1c. This technique reveals the same features as EFM, however, with a visibly lower spatial resolution due to the capacitance between the sample and the entire base of the cantilever as a result of the long range electrostatic *force*, which leads to averaging of the V_{CPD}. For example, if the probe apex is measuring at the centre of the device, the base of the cantilever can

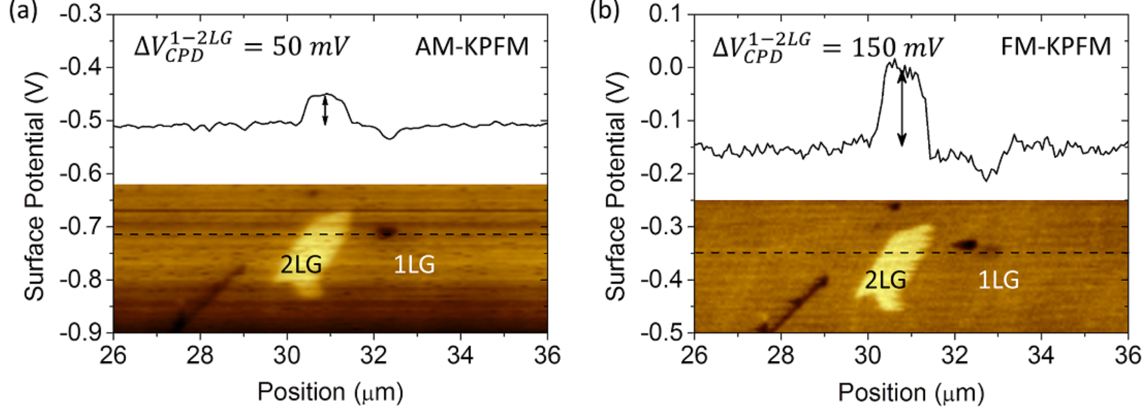

Figure 5.3: Top: V_{CPD} measurement of 1LG and 2LG with (a) AM-KPFM and (b) FM-KPFM. Bottom: Zoomed (a) AM-KPFM and (b) FM-KPFM images showing only the central 2LG from Fig. 5.1c and Fig. 5.1d, respectively. AM-KPFM and FM-KPFM line profiles were obtained along the respectively indicated dashed lines.

be over the thick Au leads. Although the largest cantilever amplitude response will be the result of strong electrostatic interactions between the sample and the probe apex, the weaker interactions between the Au lead and the cantilever base will also affect the cantilever oscillations, thus leading to an averaging effect. Accurate V_{CPD} measurements with AM-KPFM can only be performed on features that are typically 100's of microns wide. Bearing this in mind, the V_{CPD} of 1LG and 2LG is $V_{CPD}^{1LG} \sim -505mV$ and $V_{CPD}^{2LG} \sim -455mV$, respectively, giving an absolute difference of only $\Delta V_{CPD}^{1-2LG} \sim 50mV$ (Fig. 5.3a).

In comparison, FM-KPFM technique provides the same quantitative measurement (Section 4.3.3), however, with a greater consistency and accuracy (Fig. 5.1d). FM-KPFM detects the shift in the oscillation frequency, operating on the electrostatic *force gradient*, which is at its highest at the probe apex and rapidly decreases with increasing distance from the probe apex. This means the base of the cantilever has negligible contribution to the total frequency shift and therefore provides a more accurate V_{CPD} measurement with a higher spatial resolution on the order of the probe apex diameter. The V_{CPD} of 1LG and 2LG using FM-KPFM is $V_{CPD}^{1LG} \sim -154mV$ and $V_{CPD}^{2LG} \sim -4mV$, respectively, giving an absolute difference of $\Delta V_{CPD}^{1-2LG} \sim 150\,mV$ (Fig. 5.3b).

5.2 Accuracy of the surface potential measurements

As each of the three V_{CPD} measurement techniques, performed on the same day, provide a somewhat different ΔV_{CPD}^{1-2LG} of the exact same region of 1LG and 2LG from device #2a, the accuracy of each technique must be investigated. An ideal ways of determining the accuracy is to measure the V_{CPD} of a surface at a well-defined potential, for example, an operating device with a known applied voltage (V_{ch}). Measuring the V_{CPD} of a DC voltage biased (V_{ch}) Au leads of the graphene device will provide a representative comparison between the applied V_{ch} and measured V_{CPD}. For example, the total resistance contribution from measurement cables, wire bonding and Au contact leads are typically many orders of magnitude lower than the graphene channel and Au-graphene contact resistance of the device. The relatively large resistance of the channel results in a negligible potential drop from the measurement cables to the Au contacts, making this method a viable means for investigating the accuracy of V_{CPD} measurements.

The V_{CPD} was measured from left to right Au contact, as indicated by the dashed line in the EFM image of device #2a (Fig. 5.4a). The V_{CPD} line profiles were obtained using AM-KPFM (Fig. 5.4b), FM-KPFM (Fig. 5.4c) and EFS (Fig. 5.4d) for $V_{ch} = \pm 2\ V$, in increments of $0.5\ V$, applied to the left contact while grounding the right contact. The line profiles show a non-zero V_{CPD} for the grounded Au contact, which is the result of a work function difference between the Au and PFQNE-AL probe (Section 4.3). The work function difference of the left contact was accounted for by using $\Delta V = V_{CPD}(V_{ch}) - V_{CPD}(0)$ and plotting it as a function of the applied voltage (Fig. 5.4e). The measured potential is typically $\sim 27.6\%$ lower than the actual V_{ch} for AM-KPFM, whereas it is $\sim 4.4\%$ and $\sim 7.8\%$ higher for FM-KPFM and EFS, respectively. The lower ΔV measurement is consistent with spatial averaging as the relatively large base of the cantilever will weakly interact with the device channel and the right Au contact (Fig. 5.4a), both of which are at a lower V_{CPD} than the left contact. Higher measurement of the ΔV with FM-KPFM is related to an overestimation of the V_{CPD} due to a large excitation voltage ($V_{mod} = 8\ V$), whereas the overestimation with EFS is related to unoptimised fitting parameters. It is important to note that EFS is essentially a frequency-modulated technique where measuring $\Delta\varphi$ is analogous to

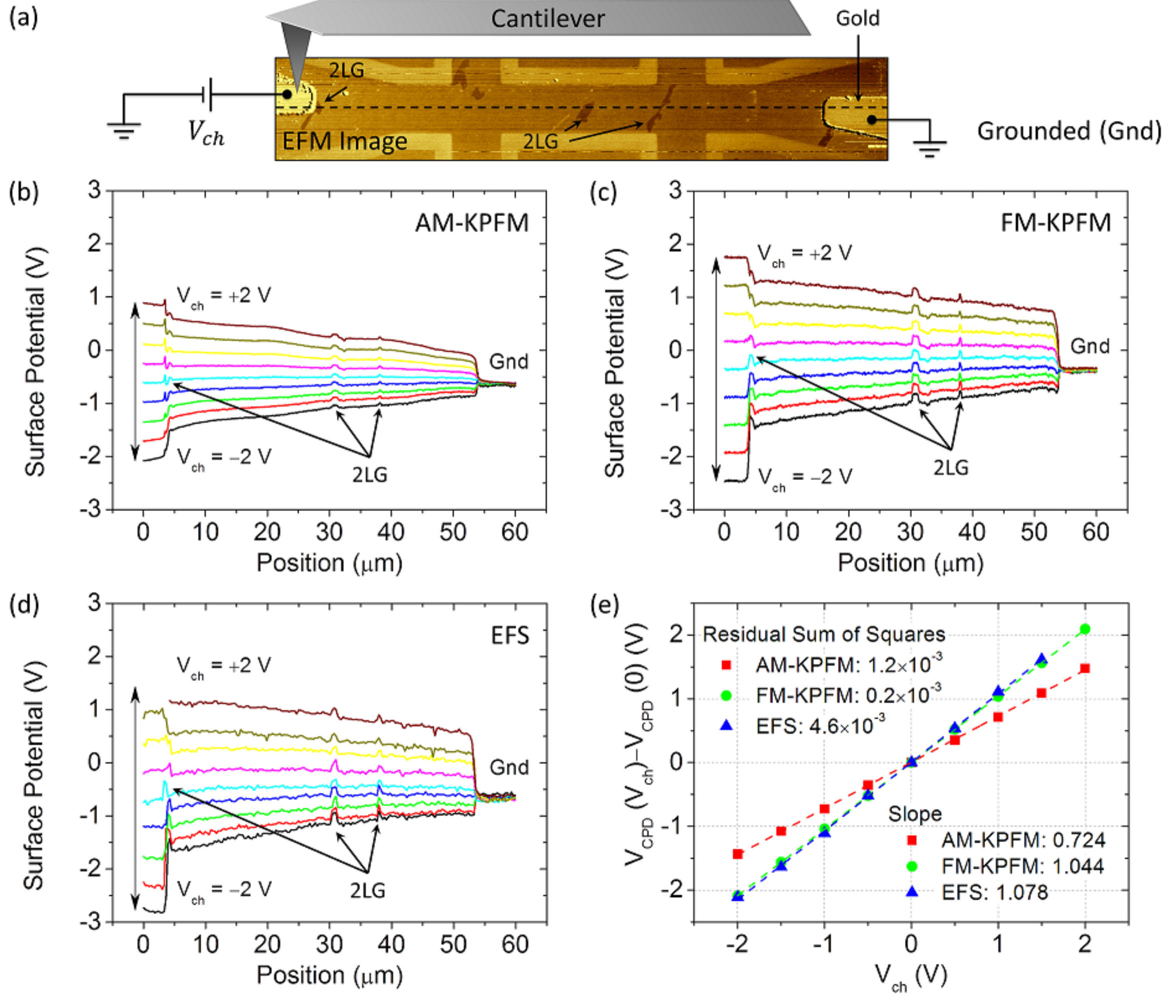

Figure 5.4: The V_{CPD} measured along the indicated dashed line in the (a) EFM image for $V_{ch} = \pm 2\,V$, in increments of $0.5\,V$, with (b) AM-KPFM, (c) FM-KPFM and (d) EFS. (e) ΔV_{CPD} value as measured by different techniques from left to right Au contact in dependence on the applied voltage (V_{ch}).

measuring the frequency shift, thus offering comparable accuracy and spatial resolution to FM-KPFM.

5.3 Contactless resistance measurements

V_{CPD} techniques are excellent contactless methods for measuring the Au-graphene contact resistance without specifically requiring a pattern that is typically used with the transmission line method (TLM) [163]. Having already measured the V_{CPD} line profiles of device #2a at $V_{ch} = \pm 2\,V$, the Au-graphene contact resistance can easily be deduced by normalising Fig. 5.4b, Fig. 5.4c and Fig. 5.4d using $\frac{V_{CPD}(V_{ch})-V_{CPD}(0)}{V_{ch}} = \frac{\Delta V}{V_{ch}}$

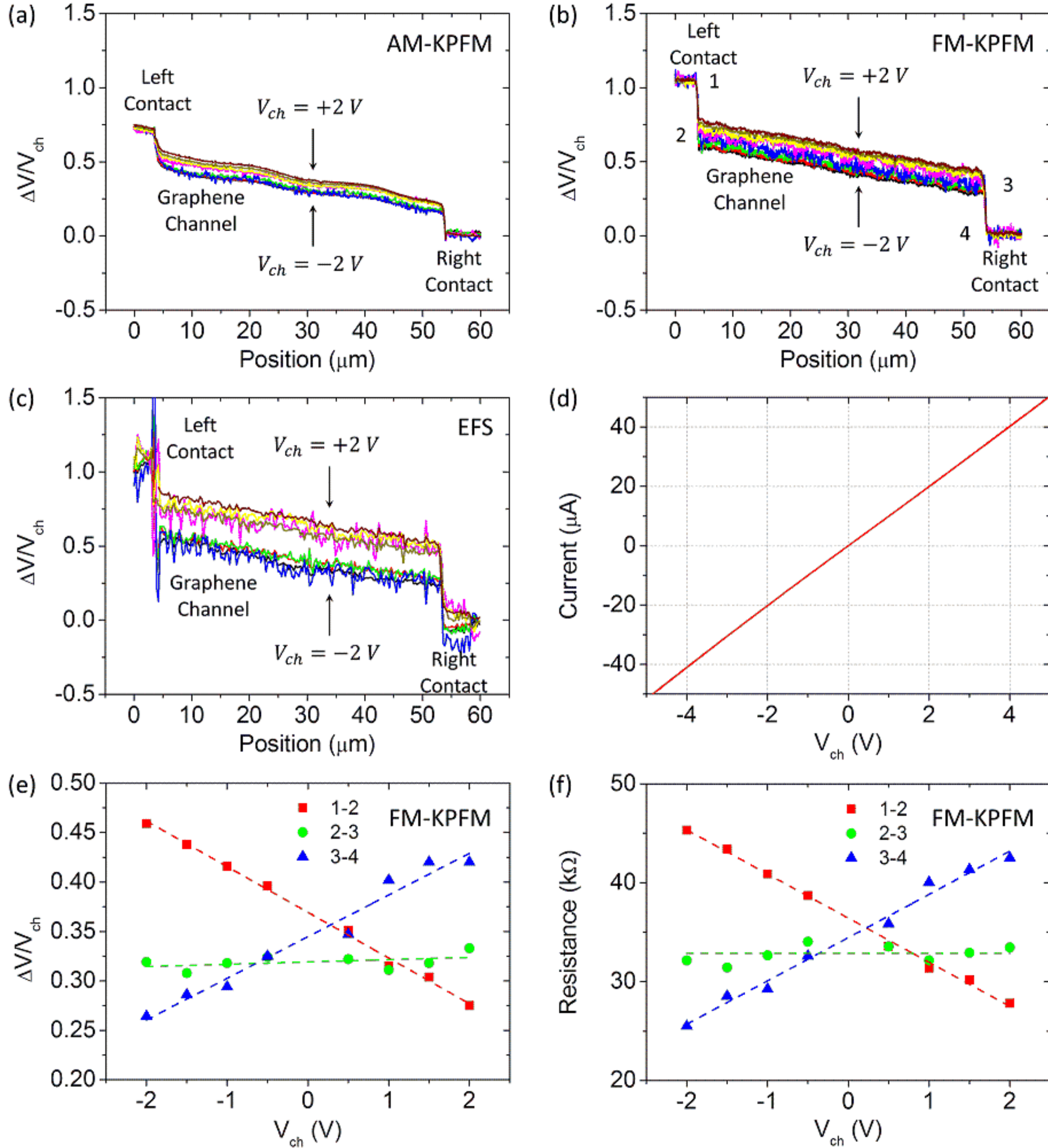

Figure 5.5: The V_{CPD} line profiles shown in Fig. 5.4 normalised using $\frac{V_{CPD}(V_{ch})-V_{CPD}(0)}{V_{ch}} = \frac{\Delta V}{V_{ch}}$ for (a) AM-KPFM, (b) FM-KPFM and (c) EFS. (d) The dependence of current (I), flowing through the entire device, on V_{ch}. V_{ch} dependence of (e) $\Delta V/V_{ch}$ and (f) resistance of graphene channel and Au-graphene contact using FM-KPFM. The dashed lines are a guide for the eye only. 1-2, 2-3 and 3-4 in (e) and (f) signifies left contact, graphene channel and right contact, respectively.

for AM-KPFM (Fig. 5.5a), FM-KPFM (Fig. 5.5b) and EFS (Fig. 5.5c), respectively. Normalising the line profiles in this manner, accounts for any V_{CPD} changes that are totally isolated from the application of V_{ch}, *i.e.*, variations in the work function of features such as 1LG, 2LG and Au. The resulting normalised line profile is solely a

consequence of the potential drop (ΔV) from changes in the resistivity. The focus will be on Fig. 5.5b for the contactless resistance measurement due to the high accuracy of FM-KPFM. Careful inspection of the Au-graphene potential drop for both contacts reveal a clear V_{ch} dependence. Focusing on the left contact (points 1-2 in Fig. 5.5b), $\Delta V/V_{ch} \sim 0.275$ from Au-graphene for $V_{ch} = +2\,V$ and increases to $\Delta V/V_{ch} \sim 0.455$ for $V_{ch} = -2\,V$ (Fig. 5.5e). However, at the right contact (points 3-4 in Fig. 5.5b), $\Delta V/V_{ch} \sim 0.415$ and ~ 0.260 for $V_{ch} = +2\,V$ and $-2\,V$, respectively. Further to the linearity in $\Delta V/V_{ch}$ with V_{ch}, each contact behaves in opposite directions, resulting in a linear current *versus* voltage (I-V_{ch}) characteristics, which was determined by measuring the total current flowing through the circuit (Fig. 5.5d). From these measurements, the contactless resistance can be determined by using $[\Delta V \times V_{ch}]/I(V_{ch})$, where $\Delta V/V_{ch}$ is taken from Fig. 5.5e and $I(V_{ch})$ from Fig. 5.5d. The multiplication of V_{ch} is essential for obtaining the actual resistance value as $\Delta V/V_{ch}$ is unitless due to the earlier normalisation. Fig. 5.5f shows the independent resistances for the graphene channel (R_{ch}) and the two Au-graphene contacts (R_{cont}). The resistance of the graphene channel remains constant at $R_{ch} \sim 33\,k\Omega$, whereas, the contacts exhibit a much larger change of $\Delta R_{cont}^{left} \sim -17.5\,k\Omega$ and $\Delta R_{cont}^{right} \sim 17\,k\Omega$ for left and right contacts, respectively. These measurements show that this particular device exhibits R_{cont} on the order of R_{ch} and that they are highly non-Ohmic. However, the R_{cont}^{left} and R_{cont}^{right} contribution to the total resistance of the device remains constant at $\sim 70\,k\Omega$ irrespective of the applied bias voltage within $V_{ch} = \pm 2\,V$, thus resulting in a linear I-V_{ch} curve.

5.4 Effects of environmental doping on 1LG

Research has shown that the electronic properties of graphene is easily influenced by external conditions. It was shown that the high level of humidity and gases such as N_2 , O_2 and NO_2 act as p-dopants (Section 2.4.4) [82]. These effects can easily be avoided by performing the experiment in vacuum or an inert atmosphere. The use of photochemicals is essential for the device fabrication process, however, their doping effects can generally be avoided by performing chemical or mechanical cleaning (Appendix C). On the contrary, the effects of the IFL is inherent to EG grown on SiC(0001),

making them considerably more difficult to avoid. Even so, research into hydrogen intercalation has shown that hydrogen can migrate under the IFL and passivate the SiC substrate [42,164]. This process transforms the IFL into a quasi-free standing graphene layer (*i.e.*, becomes the new 1LG) and subsequently turns the previous 1LG into a decoupled 2LG [42]. This subsection presents the investigations on the effect of resist residues, that are made up of a mixture of PMMA/MMA and ZEP520, which readily attach to graphene during the electron beam lithography (EBL) fabrication processes. Furthermore, the effects of vacuum, nitrogen and humidity rich environments were also investigated.

5.4.1 UV exposed photochemicals

The devices studied are fabricated from a new sample (#3), however, the graphene growth parameters were similar to sample #1 and #2, thus producing $\sim 96\%$ 1LG and $\sim 4\%$ 2LG on $4H$-SiC(0001) as revealed by large area scans (not shown). The topography image of a 970 nm wide device (#3a) revealed the 1LG was uniformly covered with resist residues with a lateral grain size of $\sim 40\,nm$ (Fig. 5.6a). Transport measurement techniques, described in Section 3.2, revealed a weakly p-doped graphene

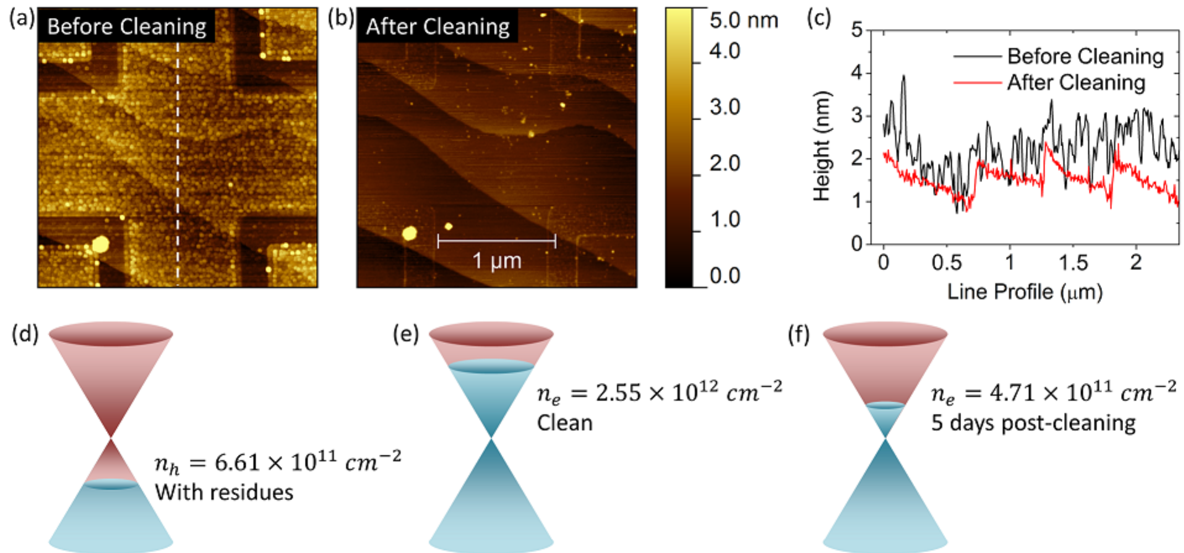

Figure 5.6: Topography image showing device #3a (a) before and (b) after CM-AFM cleaning. (c) The line profiles for both images along the white dashed line in indicated in (a). Schematic of 1LG band structure showing the doping levels of (d) with residues, (e) clean and (f) 5 days post-cleaning.

State of Device #3a	R_4 ($k\Omega$)	R_H (Ω/T)	n (cm^{-2})	μ (cm^2/Vs)	λ (nm)
With residues	26	-945	$n_h = 6.61 \times 10^{11}$	$\mu_h = 1449$	13.8
Clean	6	$+250$	$n_e = 2.55 \times 10^{12}$	$\mu_e = 1673$	31.2
5 days post-cleaning	33	$+1332$	$n_e = 4.71 \times 10^{11}$	$\mu_e = 1616$	13.0

Table 5.1: Transport measurements summary of device #3a to observe the effects of resist residues, substrate and environmental doping on epitaxial graphene.

(Table 5.1 and Fig. 5.6d). The residues were then cleaned from the surface by sweeping them to the side using contact-mode (CM-) AFM with a soft cantilever (Fig. 5.6b and Appendix C). The line profiles for contaminated and cleaned surface reveal the residue thickness to be $\sim$ 1-2 nm (Fig. 5.6c). Immediately after cleaning the sample, the transport measurements reveal a strongly n-doped graphene with 15% and 126% increase in mobility and mean free path, respectively (Table 5.1 and Fig. 5.6e), making it consistent with the vast majority of the results in literature for EG on SiC(0001). The n-type behaviour of the device in the clean state is attributed to intrinsic doping from the IFL as it donates electrons [42]. The sample was studied again further five days after being stored in a desiccator, with relative humidity $< 20\%$, revealing a weakly n-doped graphene with 13% and 58% decrease in mobility and mean free path, with respect to the clean state (Table 5.1 and Fig. 5.6f). These measurements indicate that the EG had been p-doped by the atmosphere, however, unlike the residues, the doping was only strong enough to reduce the overall carrier density to maintain n-type conduction. The p-dopant is most likely to be a common gas such as CO_2, H_2O, N_2 and O_2 [42, 79, 165–171].

Although the conventional n-type conduction is observed for EG devices on SiC(0001), in this particular case, the conduction changed through the Dirac point and all the way to p-type in the presence of the residues. It is very important to note that the residues were first attempted to be removed by exposing the whole sample for 20 minutes to 250 nm wavelength UV light and subsequently submerged in o-Xylene. Exposing the resist to UV light or e-beam irradiation has been known to have a profound effect on the chemical structure, which effectively triggers photo-induced reactions [56, 130, 172, 173]. Exposing PMMA/MMA to deep UV light is not expected to affect the doping as it does not contain chlorine or other acceptor-type radicals [173]. ZEP520 on the other-

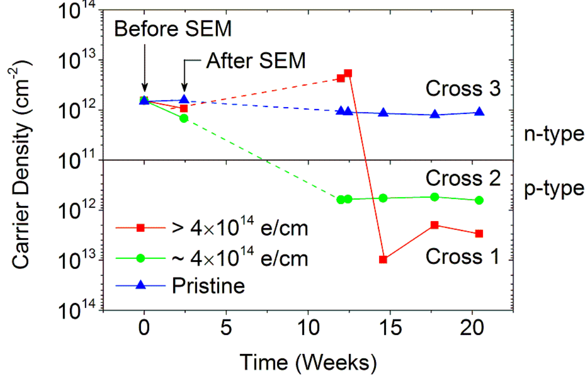

Figure 5.7: Time dependent carrier density measurements of a device (#1a) containing resist residues, which received electron-beam irradiation.

hand forms neutral chlorine radicals when exposed to deep UV or e-beam irradiation, generating active electron acceptors, turning it into a p-dopant [173, 174]. The effect was also observed on device #1a, which at the time was covered with resist residues and subsequently exposed to e-beam irradiation during scanning electron microscopy (Fig. 5.7). During the imaging, the estimated dose of e-beam irradiation received by cross 1 was $> 4 \times 10^{14}\ e/cm^2$. Cross 2 received a dose of $\sim 4 \times 10^{14}\ e/cm^2$ and cross 3 received a negligible exposure, maintaining a pristine condition. Over the course of $\sim$ 15 weeks, crosses 1 and 2 changed from n-type to p-type, while the pristine cross 3 remained n-type throughout, further confirming the p-doping nature of deep UV or e-beam irradiation exposed resist residues.

5.4.2 Controlled environment

To further investigate the p-doping nature of UV exposed resist residues, a planar p-n junction was fabricated by cleaning only part of a dual-cross device (#3b) with CM-AFM, such that the left part with residues remained p-type, while the clean right part changed to n-type (Fig. 5.8a). The mapping of V_{CPD} in ambient air using FM-KPFM produced distinctive contrasts for each side of the device (Fig. 5.8b). The work function of each side of the p-n junction was also measured using EFS (Fig. 5.8c). Using the Au leads as a stable reference, the work function of a PFQNE-AL probe was calibrated to be $\Phi_{probe} = 4.03\,eV$ and so, by using $\Phi_{sample} \approx \Phi_{probe} - eV_{CPD}$, the work functions of p-type and n-type EG were determined as $\Phi_p^{C_1} = 4.68 \pm 0.05\,eV$ and $\Phi_n^{C_2} = 4.35 \pm 0.05\,eV$, respectively (Fig. 5.8d). In this particular case, the doping from the resist residues increased the work function by $\Delta\Phi_{p-n}^{EFS} = 330 \pm 100\,meV$, which is consistent with the

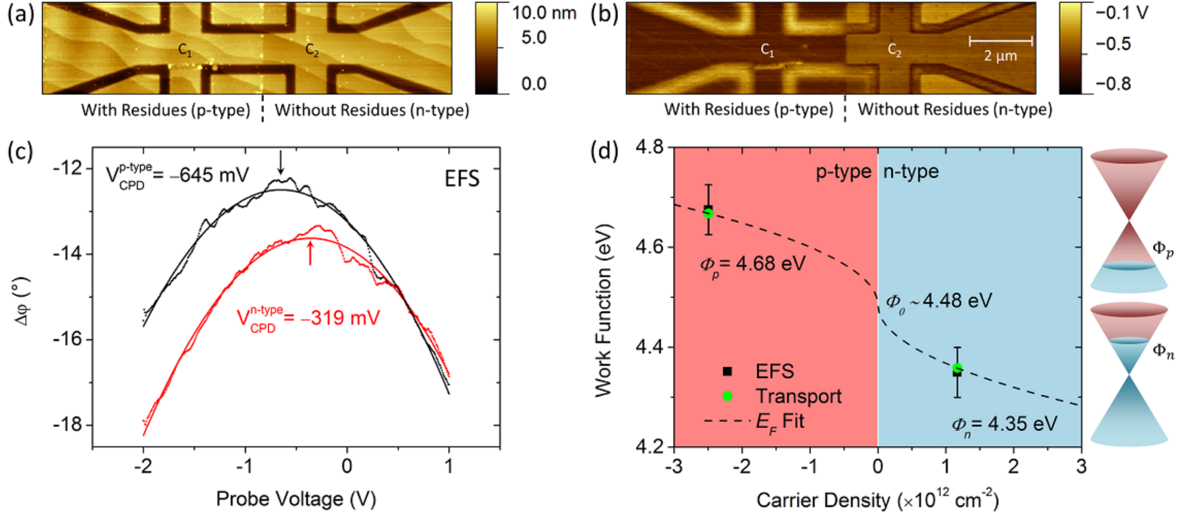

Figure 5.8: (a) Topography and (b) V_{CPD} map, obtained using FM-KPFM, of device #3b after the right-hand-side of the device was cleaned with CM-AFM. C_1 and C_2 represents crosses 1 and 2. (c) EFS measurements performed on each side of the device. (d) Carrier density dependence on the work function for 1LG. The dashed line is a fit of E_F for 1LG.

Device #3b	R_H (Ω/T)	n (cm^{-2})	E_F (meV)	Φ (eV)
Cross 1 (with residues)	-250	$n_h = 2.50 \times 10^{12}$	184	4.68 ± 0.05
Cross 2 (without residues)	$+535$	$n_e = 1.17 \times 10^{12}$	126	4.35 ± 0.05

Table 5.2: A summary of the transport measurements for a p-n junction device.

Fermi energy calculated from transport measurements using the $E_F(n) = \hbar\nu_F\sqrt{\pi n}$, where $\Delta\Phi_{p-n}^{transport} = 310\,meV$ (Table 5.2). Fitting the data using the E_F, the intrinsic work function (*i.e.*, the Dirac point) was extrapolated to be $\Phi_0 \sim 4.48 \pm 0.05\,eV$, which is comparable to a previous published value of $\Phi_0 \sim 4.47 \pm 0.05\,eV$ [124]. Yu *et al.* also demonstrated a $\Delta\Phi_{p-n} \sim 300\,meV$ using bottom gate [124], however, the static doping of the planar p-n junction presented here (device #3b) and the lack of complementary carrier density measurements by Yu *et al.* prohibit a direct comparison between the two sets of results.

In order to understand the cause of p-doping from the resist residues, transport measurements were carried out in a controlled environmental chamber, which was also capable of reaching a high vacuum. Characterising the device again in ambient air revealed $n_h^{C_1} = 5.7 \times 10^{11}\,cm^{-2}$ and $n_e^{C_2} = 4.2 \times 10^{11}\,cm^{-2}$ for crosses 1 and 2, respectively (0th hour in Fig. 5.9). It is important to note that the measurements here were carried out on different days to the work function measurements, therefore the baseline

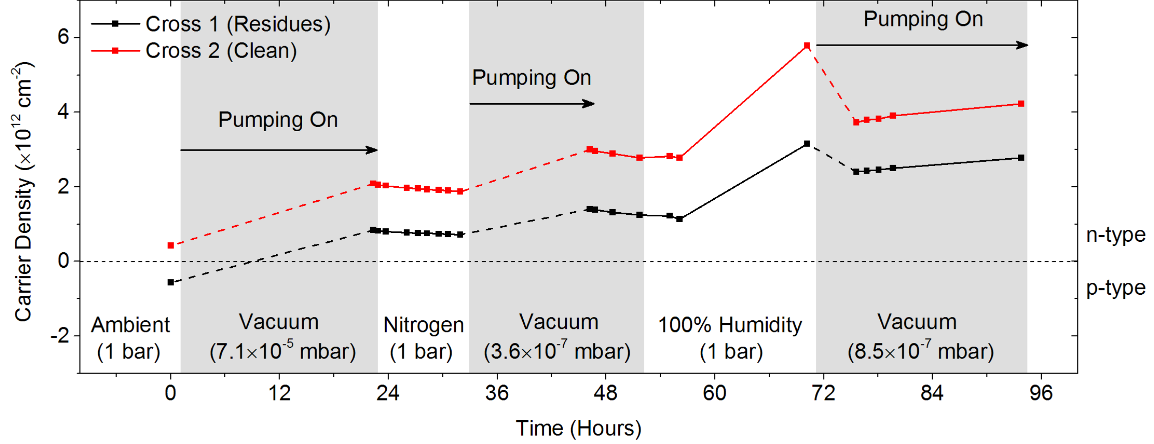

Figure 5.9: The carrier density transformation of device #3b with the environment changing from ambient air → vacuum → nitrogen → vacuum → 100% relative humidity → vacuum, over the course of 4 days.

transport properties of the device are somewhat different. The sample chamber was then pumped for 20 hours using a turbo pump, reaching a base pressure of $7.1 \times 10^{-5}\,mbar$, at which point, $n_e^{C_1} = 8.4 \times 10^{11}\,cm^{-2}$ and $n_e^{C_2} = 2.1 \times 10^{12}\,cm^{-2}$ (22th hour in Fig. 5.9). Note, the entire device changed to n-type due to substantial doping only from the IFL. The effect of nitrogen gas was investigated by flooding the chamber with pure nitrogen direct from vacuum to atmospheric pressure. Over the course of 10 hours, the carrier density dropped to $n_e^{C_1} = 7.2 \times 10^{11}\,cm^{-2}$ and $n_e^{C_2} = 1.9 \times 10^{12}\,cm^{-2}$ (32nd hour in Fig. 5.9). This shows that although the entire device maintained n-type conduction, the reduction in carrier density indicates nitrogen is a p-dopant. The chamber was pumped for 14 hours to clean the sample and chamber from nitrogen, reaching a base pressure of $3.6 \times 10^{-7}\,mbar$. Under this higher vacuum level, the carrier density of the entire sample increased to $n_e^{C_1} = 1.4 \times 10^{12}\,cm^{-2}$ and $n_e^{C_2} = 3.0 \times 10^{12}\,cm^{-2}$ (46th hour in Fig. 5.9). Note: between 46th and 52nd hour, the pumping was stopped and sample was kept under vacuum, however, the pressure was not monitored. At 52nd hour, the sample was flooded with a continuous flow of nitrogen containing 100% relative humidity for 2 hours. Having sealed the chamber full of humid nitrogen, the sample was left in that state for 15 hours (70th hour in Fig. 5.9), at which point the carrier density further increased to $n_e^{C_1} = 3.2 \times 10^{12}\,cm^{-2}$ and $n_e^{C_2} = 5.8 \times 10^{12}\,cm^{-2}$. This shows that humid nitrogen n-dopes the graphene. Furthermore, the relative increase in carrier density of

$\sim 126\%$ (from 46$^{\text{th}}$ to 70$^{\text{th}}$ hour) was larger for the clean cross 2 than the contaminated cross 1 ($\sim 93\%$), indicating that the resist residues act as a weak barrier to humidity. Upon continuous pump on the chamber for 24 hours, removing the humid nitrogen decreased the carrier density to $n_e^{C_1} = 2.8 \times 10^{12}\, cm^{-2}$ and $n_e^{C_2} = 4.2 \times 10^{12}\, cm^{-2}$ (94$^{\text{th}}$ hour in Fig. 5.9). Throughout these measurements, with each subsequent pumping stage, the carrier density for the entire device steadily increases, which indicates to a substantial amount of p-dopants from the ambient air still present on the sample surface. While it is generally regarded that humidity (*i.e.*, water vapour) p-dopes graphene, the measurements conducted here clearly show water vapour in fact n-dopes graphene. It is entirely possible that if the humidity was mixed with air instead of nitrogen, oxygen molecules are the actual p-dopants.

5.5 Work function of 1LG and 2LG

The band structures of 1LG and 2LG are described by linear and parabolic dispersions, respectively, leading to differences in their transport properties (Section 2.1). Completely uniform coverage of EG on SiC has yet to be demonstrated, thus making it important to characterise the properties for each layer thickness. However, as demonstrated in Section 5.1, EFS is a non-invasive technique that is capable of accurately measuring the work function of 1LG (Φ_{1LG}) and 2LG (Φ_{2LG}) on the nanoscale by using a probe with calibrated work function.

The device #2a was first cleaned of resist residues using the CM-AFM followed by EFS measurements to characterise Φ_{1LG} and Φ_{2LG}. The resist residues, discussed in Section 5.4, were removed so that a reliable comparison could be made with measurements obtained by other groups. However, the exact state (*i.e.*, clean or contaminated with residues) of devices presented in literature that are discussed here is not specified. The V_{CPD} for 1LG, 2LG and Au was determined by performing 200 individual measurements along the dashed line indicated in the EFM image (Fig. 5.10a). Using $\Phi_{Au} = 4.82\, eV$ as a reference, the PFQNE-AL probe work function was calibrated to be $\Phi_{probe} = 4.09\, eV$ and subsequently $\Phi_{1LG} = 4.55 \pm 0.02\, eV$ and $\Phi_{2LG} = 4.44 \pm 0.02\, eV$ for 1LG and 2LG, respectively, in ambient air (Fig. 5.10b). The difference in the work

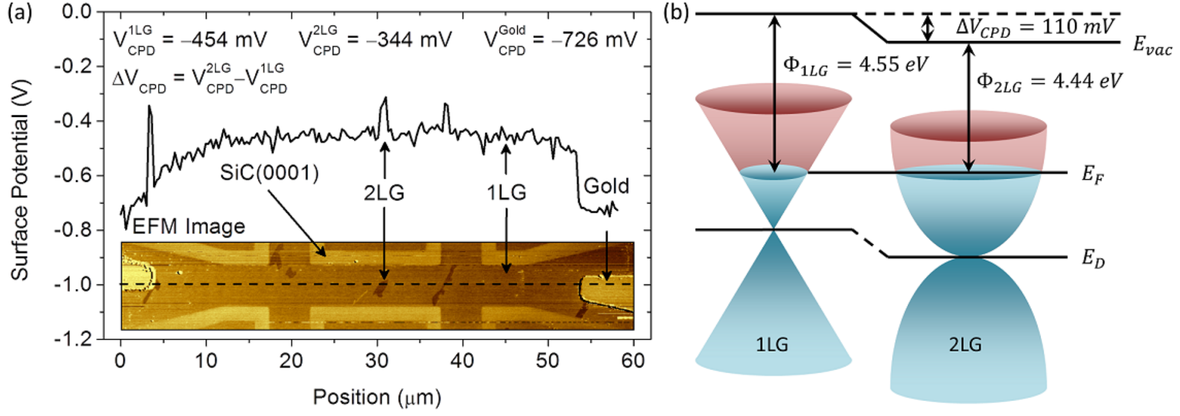

Figure 5.10: (a) The V_{CPD} obtained by EFS along the dashed line indicated in inset EFM image of device #2a. Note: the EFM image is a phase map, where the relative contrast between 1LG and 2LG depends on the DC voltage applied to the probe (V_{probe}). (b) The linear and parabolic band structure of n-type 1LG and 2LG, respectively, when they are in electrical contact with each other, *i.e.*, with the Fermi energy aligned.

Substrate	Φ_{1LG} (eV)	Φ_{2LG} (eV)	$\Delta\Phi_{1-2LG}$ (meV)	KPFM technique	Reference
$4H$-SiC	4.55 ± 0.02	4.44 ± 0.02	110 ± 21	FM	Device #2a
$6H$-SiC	–	–	135 ± 9	FM	[62]
SiO_2	4.57 ± 0.05	4.69 ± 0.05	120 ± 50	FM	[124]
$SrTiO_3$	4.409 ± 0.039	4.516 ± 0.035	$107 \pm 36^{(1)}$	FM	[175]
$4H$-SiC	–	–	$15 - 50^{(2)}$	AM	[84]
$4H$-SiC	–	–	35	AM	[176]
SiO_2	–	–	68	AM	[125]

Table 5.3: A summary of the work function difference between 1LG and 2LG, where graphene was epitaxially grown on SiC (n-type) and graphene obtained by mechanical exfoliation was transferred to SiO_2 and $SrTiO_3$ substrates (p-type). Note: $^{(1)}$Measurements are performed in ultra-high vacuum. In all other cases, measurements are performed in ambient environment. $^{(2)}\Delta\Phi_{1-2LG}$ = 15-50 meV at 20-120 $^{\circ}C$, respectively.

function between 1LG and 2LG, $\Delta\Phi_{1-2LG} = 110 \pm 21\ meV$, is in good agreement with values obtained using FM-KPFM by other groups (Table 5.3).

It is generally accepted that substrate doping tends to decrease with increasing layer thickness. However, the environmental effects must also be considered, for example, the total doping of 1LG is dictated by the doping from the IFL (bottom of 1LG) and the environment (top of 1LG) (Fig. 5.11a). For 2LG, the effect is further complicated. First, the IFL will strongly interact with the bottom layer and weakly interact with the top layer of the 2LG sandwich, which is vice versa for environmental doping (Fig. 5.11b). The effect is further complicated by the weak interactions between the top

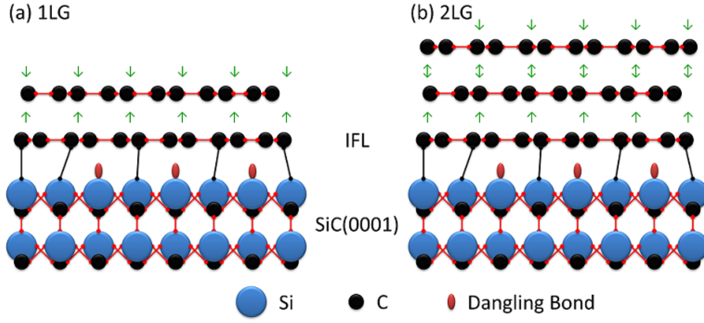

Figure 5.11: Schematic structure showing environmental and IFL doping for (a) 1LG and additional interlayer interactions for (b) 2LG. Adapted from Ref. [42].

and bottom layers of the 2LG sandwich, making it extremely difficult to form an exact comparison between data sets.

5.6 Effects of 2LG islands on transport properties

Transport measurements were also conducted in ambient conditions on a set of 1LG devices containing varying proportions of 2LG islands. Prior to the lithography process, islands of 2LG were located using FM-KPFM and the sample (#4) was strategically designed and fabricated such that the 2LG islands would be present at selected locations of the sensing area and along the channel of 660-970 nm wide devices. Within the specified size range, the transport properties have virtually no size dependence (Section 3.2). The exact percentages of 2LG and their locations were verified again after the fabrication process (Fig. 5.12a inset). Fig. 5.12a shows the dependence of R_4 on

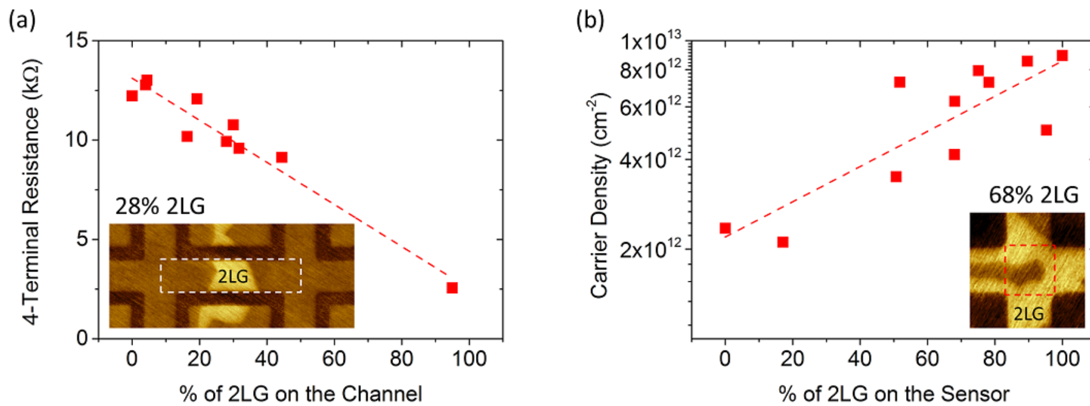

Figure 5.12: The dependence of (a) 4-terminal resistance and (b) carrier density on the percentage of 2LG graphene present on 1LG devices. Insets in (a) and (b) shows a device channel and sensor containing 2LG that covers 28% and 68% of the total area (dashed boxes), respectively.

the percentage of 2LG present on the channel of 1LG devices. The results show that a uniform 1LG device (*i.e.*, 0% 2LG) exhibits $R_4 = 13\,k\Omega$, which linearly decreases to $R_4 = 2.5\,k\Omega$ for an almost uniform 2LG device (*i.e.*, 95% 2LG), indicating that 1LG is ~ 5 times more resistive than 2LG. Carrier density measurements conducted in the Hall geometry, on the same set of devices, show that uniform 1LG exhibits $n_e^{1LG} \sim 2 \times 10^{12}\,cm^{-2}$, whereas a uniform 2LG exhibits $n_e^{2LG} \sim 8 \times 10^{12}\,cm^{-2}$, which is ~ 4 times larger than 1LG (Fig. 5.12b).

5.7 Edge effects

Despite the fact that devices are fabricated from completely different batches of EG, surface potential measurements have shown changes in electronic properties at the edge of graphene devices numerous times (Fig. 5.1d and Fig. 5.8b). For instance, the high resolution topography map and line profile of devices #4b shows a protrusion appearing at the graphene-SiC edge ~ 2 hours after the CM-AFM cleaning process (Fig. 5.13a and Fig. 5.13c, respectively). The surface potential map and line profile of the same location as Fig. 5.13a shows that electronic properties of graphene up to $\sim 75\,nm$ from the lithographically defined edge are somewhat different from bulk, with a total drop of $V_{CPD} \sim 565\,mV$ (Fig. 5.13b and Fig. 5.13c, respectively).

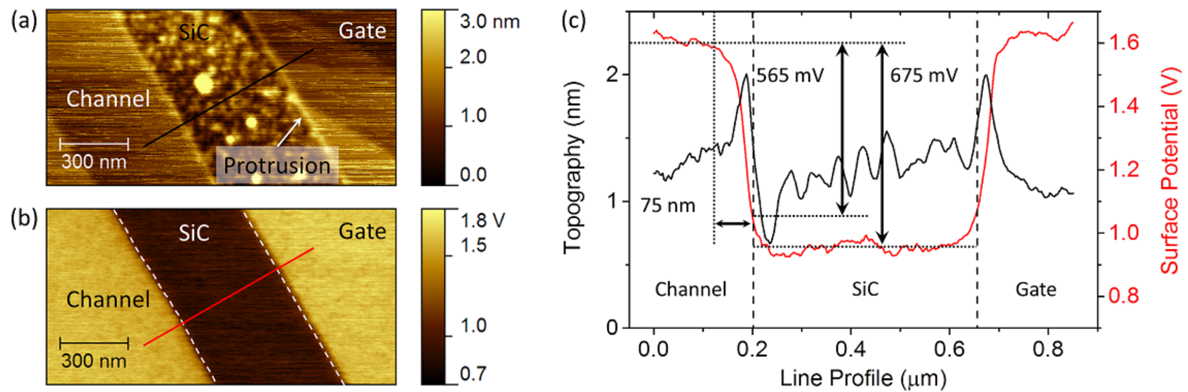

Figure 5.13: (a) Topography and (b) V_{CPD} map of device #4b, obtained using FM-KPFM, ~ 2 hours after the CM-AFM cleaning process. (c) Topography and V_{CPD} line profiles along the black and red lines indicated in (a) and (b), respectively. The dashed white lines in (b) marks out the lithographically defined edge, which was determined from (a) by taking the half-distance between 12 and 88 % relative intensity of the edge spread function, as defined in the standard on lateral resolution [177].

The edge effects were quantitatively studied in detail with EFS on device #4a. SCM-PIT probe with $\Phi_{probe} \sim 5.29\,eV$ was used to carry out the work function measurements at the centre (Φ_C) and $\sim 30\,nm$ from the physical edge (Φ_E) of the etched graphene channel. A total of ten EFS curves were obtained at each position, from which the averages are shown in Fig. 5.14a. The work function of 1LG in the grounded state was determined as $\Phi_C = 4.17 \pm 0.06\,eV$ and $\Phi_E = 4.47 \pm 0.08\,eV$ (Fig. 5.14b). Φ_C is effectively a measure of the bulk 1LG work function, which is lower than $\Phi_n = 4.35 \pm 0.05 eV$ measured on n-doped side of device #3b. This can be attributed to a lower carrier density of $n_e = 1.17 \times 10^{12} cm^{-2}$ for device #3b, whereas transport measurements performed on device #4a revealed $n_e = 2.95 \times 10^{12}\,cm^{-2}$. The differences in bulk carrier density can be attributed to differences in the IFL doping as the devices are fabricated out of completely different batches of EG samples. Furthermore, the measurements were carried out on different days, therefore daily variations in the atmospheric conditions can also result in changes from the environmental doping.

Comparing the work function at the centre with the edge results in a difference of $\Delta\Phi_{C-E} = -300\,meV$, which indicates to a significantly different carrier density at the edges. An estimate can be obtained by using the bulk carrier density from transport measurements together with the work function measurements. The Fermi energy at the centre was first calculated as $E_F^{Centre} = 200\,meV$ from $n_e = 2.95 \times 10^{12}\,cm^{-2}$ using $\pm E_F = \hbar \nu_F \sqrt{\pi n}$, where + is n-type and − is p-type. Then using $\Delta\Phi_{C-E}$ provided us with the estimate of $E_F^{Edge} = E_F^{Centre} + \Delta\Phi_{C-E} = -100\,meV$ for the edge, where the

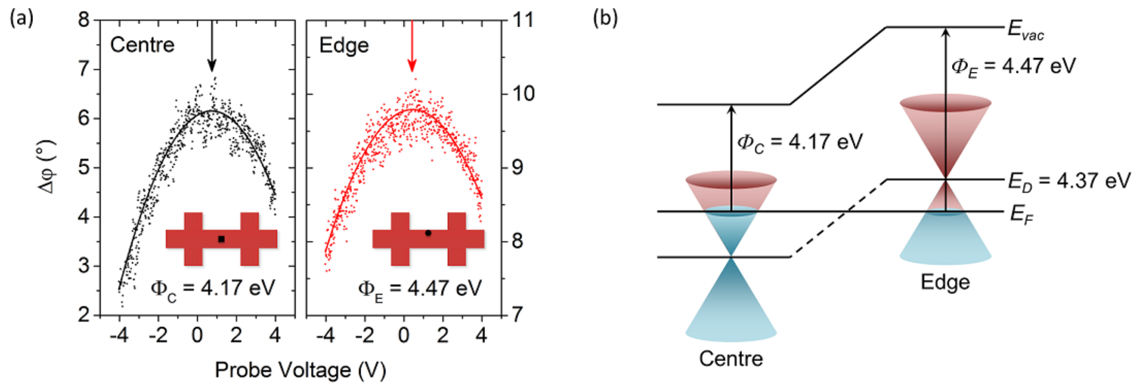

Figure 5.14: (a) EFS measurements performed on device #4a at the centre and edge of the etched graphene channel. (b) 1LG band structure showing the work function at the centre and edge.

negative sign signifies the graphene at the edge is p-doped with $n_h = 7.33 \times 10^{11}\, cm^{-2}$. An estimate of the work function was also obtained for the Dirac point ($E_D = \Phi_C + E_F^{Centre} = 4.37\, eV$) of the graphene (Fig. 5.14b).

Previous reports have been made for graphene samples with n-type central region, surrounded by p-type edges, using other techniques [178–180]. For instance, the doping variations at the edges of exfoliated graphene have shown a red shift of the G-peak in scanning Raman spectroscopy measurements [181]. Furthermore, p-doping has also been observed for lattices of lithographically fabricated antidots, where a significant variation in the D-peak was attributed to defect induced scattering processes [182]. Due to the damaging nature of the reactive ion etching processes, the oxygen plasma can oxidise the edges. Furthermore, the etching can break the symmetry in the honeycomb lattice [178], creating dangling bonds that attract p-doping molecules such as O_2, CO_2 and H_2O [69, 183–186] and n-doping molecules such as NH_3 [183]. The fact that protrusions appear at the graphene edge after the CM-AFM cleaning process indicates to adsorbent molecules attaching to the defective edge, soft gating the graphene. While it is not possible to determine the exact reason for p-type edges from these results, measurements performed in a controlled environment (Section 5.4.2) gives indication to oxygen or oxygen containing molecule being the main cause of the effect. Furthermore, the measurement could be repeated in a specific gas rich atmosphere to potentially enhance the effect.

5.8 Summary

In summary, a comparison of the three most widely used techniques revealed FM-KPFM to be the most accurate surface potential measurement technique, principally due to operation on the force gradient. AM-KPFM was determined to be the least accurate technique for surface potential measurements on non-uniform samples on the submicron scale. AM-KPFM suffers from considerable sample-cantilever base capacitance affecting the force acting on the cantilever. However, with the force gradient being largest at the probe apex, the capacitance effects are negligible for FM-KPFM and EFS. Furthermore, the force gradient confinement yields a spatial resolution of ap-

proximately the probe apex diameter. Applying all three SP measurement techniques to characterise EG devices yielded $\Delta V_{CPD}^{1-2LG} = 50$,110 and $150\,mV$ for AM-KPFM, EFS and FM-KPFM, respectively. The averaging effect of the cantilever base is the result of a lower ΔV_{CPD}^{1-2LG} for AM-KPFM, whereas the discrepancy with EFS is attributed to a small number of measurement points on 2LG. Calibrating the work function of the probe against Au electrodes revealed Φ for 1LG and 2LG to be $\Phi_{1LG} = 4.55 \pm 0.02\,eV$ and $\Phi_{2LG} = 4.44 \pm 0.02\,eV$, respectively (for the particular sample discussed in Section 5.5), Comparison of $\Delta\Phi_{1-2LG}$ obtained with AM- and FM-KPFM against values from literature confirmed the FM-KPFM to be the more superior technique.

The transmission line method is widely used to determine contact resistance, however the method requires a specific TLM pattern. FM-KPFM can be applied to any device, providing a direct measurement of the contact resistance. Investigations into graphene-Au leads contact resistance revealed non-Ohmic behaviour with resistances fluctuating from ~ 25 to $\sim 45\,k\Omega$ at V_{ch} up to $\pm 2\,V$, whereas the channel remained at $\sim 33\,k\Omega$ with resistivity of $2.7 \times 10^{-6}\,\Omega cm$.

Work function measurements were conducted for a quantitative measure of the Fermi energy. For this, the work function of the probe had to be first calibrated using Au as a reference. EFS was used to conduct accurate measurements on a planar p-n junction device that was fabricated by cleaning only half the channel (n-type) and leaving the other half contaminated with residues (p-type), where $\Phi_n = 4.35 \pm 0.05\,eV$ and $\Phi_p = 4.68 \pm 0.05\,eV$, respectively, giving a difference in n- and p-type Fermi energy of $\Delta\Phi_{p-n}^{EFS} = 330 \pm 100\,meV$. This value obtained entirely by SPM technique was consistent with $\Delta\Phi_{p-n}^{transport} = 310\,meV$ obtained from transport measurements. These measurements reveal a significant alteration in the characteristics of graphene devices fabricated using EBL processes. Furthermore, environmental doping effects were investigated by performing measurements in vacuum, pure nitrogen, 100% relative humidity. Transferring the device into vacuum reversed the effects from the environment, restoring the strong n-doping from the IFL. Transferring the sample from vacuum to a pure nitrogen environment decreased the electron carrier density, indicating nitrogen is a p-dopant. However, introducing the sample to 100% relative humidity further increased the electron carrier density, revealing water vapour to be an n-dopant.

FM-KPFM was also applied to study changes in the SP at lithographically defined edges of EG devices. Quantitative work function measurements were used in conjunction with transport measurements to reveal the conduction at the edges were hole driven, whereas the bulk central part of the device remained n-type. The p-type nature of the edges are believed to be the result of oxygen plasma etching process oxidising the graphene as well as breaking the symmetry of the honeycomb lattice, creating dangling bonds that attract oxygen containing molecules.

The effects of isolated 2LG islands on transport properties were also investigated by mapping the SP of devices with varying proportions of 2LG. The transport properties were correlated with the exact percentage of 2LG present on the device. The statistics showed that $R_4 \sim 13\,k\Omega$ for channels containing 0% 2LG (*i.e.*, uniform 1LG) and decreases linearly with increasing percentage of 2LG, reaching $R_4 \sim 2.5\,k\Omega$ for channel with 95% 2LG. Carrier density measurements in the Hall bar geometry showed $n_e^{1LG} \sim 2 \times 10^{12}\,cm^{-2}$ for cross containing 0% 2LG, whereas $n_e^{2LG} \sim 8 \times 10^{12}\,cm^{-2}$ for 100% 2LG, indicating that n is ~ 4 times larger for 2LG, confirming the decrease in resistance for 2LG.

Chapter 6

Electrical and magnetic gating

Further to the nanoscale mapping of epitaxial graphene devices, the effects of lateral and scanning local electrical and magnetic gating are also important in understanding the bulk transport properties. For example, SGM is a well-established technique that can be used to locally top gate graphene devices to investigate effects such as the local [162, 187] and edge conductance enhancement [188], localised states in wide constrictions [189], charge inhomogeneity and extrinsic doping [118]. As it has been shown that a band gap can be opened in 2LG by inducing an electric field between the two layers [13, 190], the presence of 2LG islands on devices can significantly affect the transport properties of devices. Such effects could potentially be investigated with SGM techniques. This chapter first describes the nanoscale investigations into *lateral electrically-gated* 1LG devices and how these effects correlate with bulk transport measurements. However, as the effects of lateral gates on 2LG islands are more difficult to observe, SGM and SGS techniques (Section 4.4) are also used to *locally top-gate* devices. The effects of a local out-of-plane electric and magnetic field on the bulk transport properties of EG devices have been mapped. These techniques are used to understand the behaviour of uniform EG devices and compare them to non-uniform EG devices, effectively revealing the exact screening behaviour of 2LG.

6.1 Electrical lateral gates

This section investigates the nanometre scale changes of the surface potential resulting from electric fields created by lateral gates. The device is formed by etching a trench in the shape of a Hall bar. The remaining graphene is used as lateral gates as they are electrically isolated from the Hall bar due to the insulating nature of the SiC substrate. The electric field effects were investigated on four separate dual-cross devices fabricated out of 1LG from sample #4. Device #4a, #4c and #4d consisted of 970, 680 and 450 nm wide crosses, respectively, with 280 nm channel-gate spacing. Device #4b consisted of a 910 nm wide cross with 480 nm channel-gate spacing. All devices underwent CM-AFM cleaning to remove any resist residues and their effects on the electronic properties of graphene (Section 5.4).

6.1.1 Nanoscale visualisation of the gating effect

The effect of lateral electric fields on the nanometre scale was investigated on device #4b using SCM-PIT probes (Table 4.1). The topography (Fig. 6.1a) and surface potential (Fig. 6.1b) images were simultaneously obtained using FM-KPFM (Section 4.3.3) to first determine the exact electronic structure of the device. The topography map clearly shows all the previously observed features, such as terraces, whereas the surface potential map reveals 1LG with the exception of a few isolated 2LG islands present near Cross 2. The effect of the lateral gates on a grounded channel was observed by using FM-KPFM to measure the V_{CPD} along the red dashed line indicated in Fig. 6.1b. V_{CPD} line profiles were obtained for $V_g = 0$, ± 1 and $\pm 2\,V$, the results of which are shown in Fig. 6.1c. The V_{CPD} values are shifted from zero due to differences in the work function of the probe, graphene and SiC. Fig. 6.1d shows the line profiles which takes into account the work function differences by normalising the raw data using $\Delta V_{CPD} = V_{CPD}(V_g) - V_{CPD}(V_g = 0)$. The resulting data accurately shows the voltages applied to the gates. Furthermore, V_{CPD} for bulk of the grounded channel is largely unaffected for $V_g = \pm 2\,V$, however a small change is observed near the edges (Fig. 6.1e). The changes in $V_{CPD}(V_g = 0)$ observed up to $\sim 75\,nm$ from the edge is related to the inherent changes in the carrier density (Section 5.7). However, inspecting

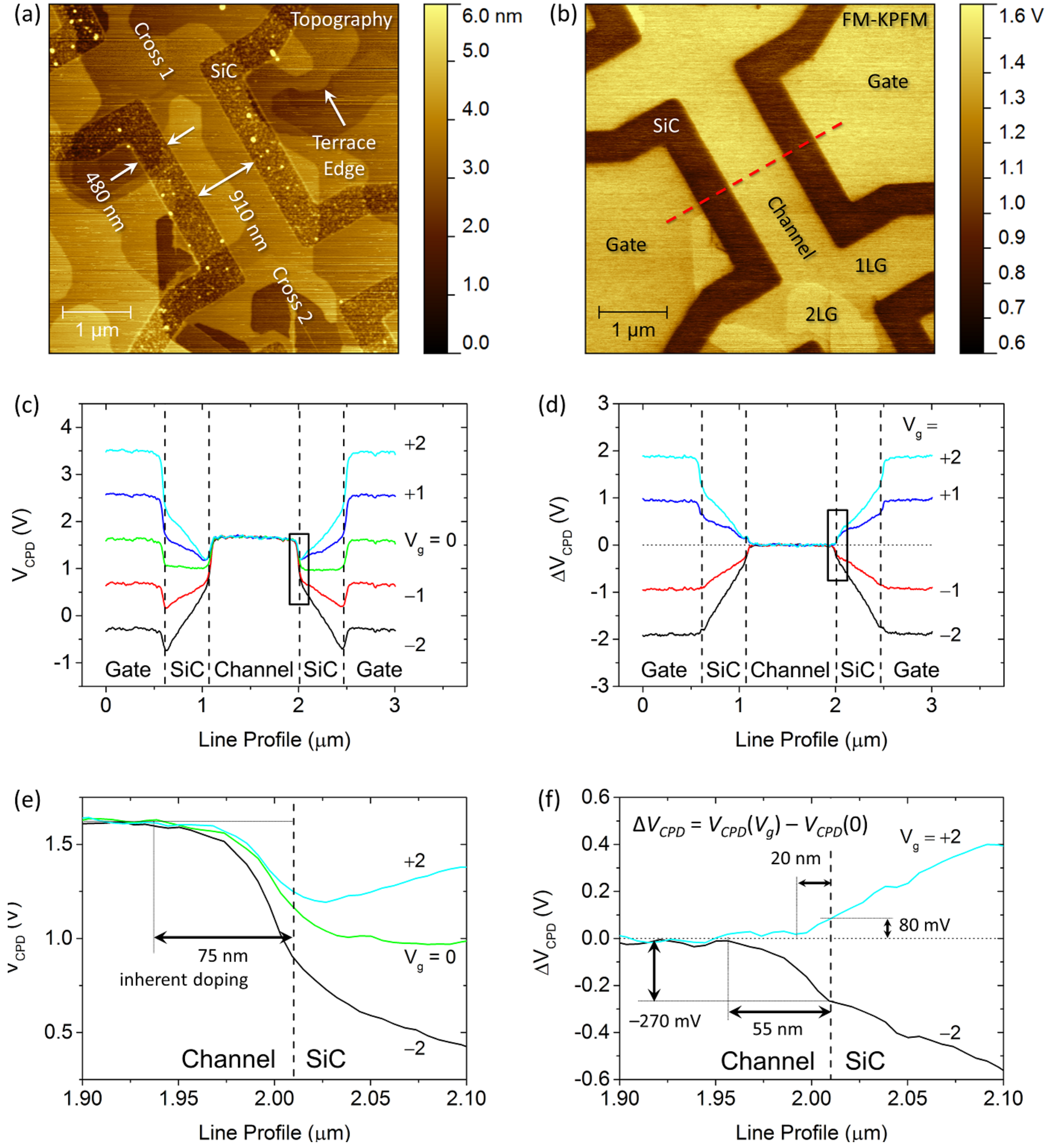

Figure 6.1: (a) Topography and (b) V_{CPD} maps of device #4b obtained by FM-KPFM. (c) V_{CPD} and (d) ΔV_{CPD} (normalised) line profiles obtained along the red dashed line indicated in (b) for $V_g = 0, \pm 1$ and $\pm 2V$. (e) and (f) shows the zoom of the area indicated by the black boxes in (c) and (d), respectively. The vertical dashed lines in (c)-(f) indicate the graphene-SiC boundaries.

the normalised line profiles near the edge shows that ΔV_{CPD} increases by $\sim 80\,mV$ at $V_g = +2\,V$, whereas ΔV_{CPD} decreases by $\sim 270\,mV$ at $V_g = -2\,V$ (Fig. 6.1f). ΔV_{CPD} line profiles also show that positive V_g affects the graphene up to $20\,nm$ from the edge, whereas negative V_g affects it up to $55\,nm$. These results show that positive V_g are ~ 3 times less effective than negative V_g at changing the V_{CPD} and the distance up to which

V_{CPD} is affected. However, this is still only 12% of the entire channel width.

6.1.2 Gating effect quantified on nanoscale

The lateral gating effect was accurately quantified using a calibrated SCM-PIT probe ($\Phi_{probe} \sim 5.29\,eV$) by means of EFS technique. The work function was measured at two locations on device #4a: at the centre (Φ_C) and $\sim 30\,nm$ from the edge (Φ_E) of the channel, for $V_g = -2$ to $+2V$, in increments of $100mV$ (Fig. 6.2a). The work function at the centre of the channel (black squares) was $\Phi_C = 4.17 \pm 0.09eV$, showing no observable effect from the lateral gates, whereas Φ_E (red circles) was affected by $\sim 512\,meV$. Note: Φ_E measurements here also include the inherent changes in the carrier density. Accounting for the latter using $\Delta\Phi = \Phi(V_g) - \Phi(V_g = 0)$ results in $\Delta\Phi_E \sim 345 \pm 75 meV$ and $\Delta\Phi_E \sim 167 \pm 110\,meV$ at $V_g = -2\,V$ and $V_g = +2\,V$, respectively. The work function of the Dirac point ($E_D = 4.37\,eV$), which was previously estimated for the current device in Section 5.7, is also marked out by the horizontal dashed line in Fig. 6.2a. In addition, Fig. 6.2b shows the carrier density, that was estimated from the work function measurements using the technique described in Section 5.7. The results show that majority of carriers (*i.e.*, in the centre of the channel) remains n-type at $n_e \sim 2.95 \times 10^{12}\,cm^{-2}$ with no observable effect from the lateral gates. However, the carrier density and even type can be controlled at the edge from $n_h = 1.8 \times 10^{13}\,cm^{-2}$ (p-type) at $V_g = -2\,V$ to $n_e = 1.3 \times 10^{12}\,cm^{-2}$ (n-type) at $V_g = +2\,V$, where the

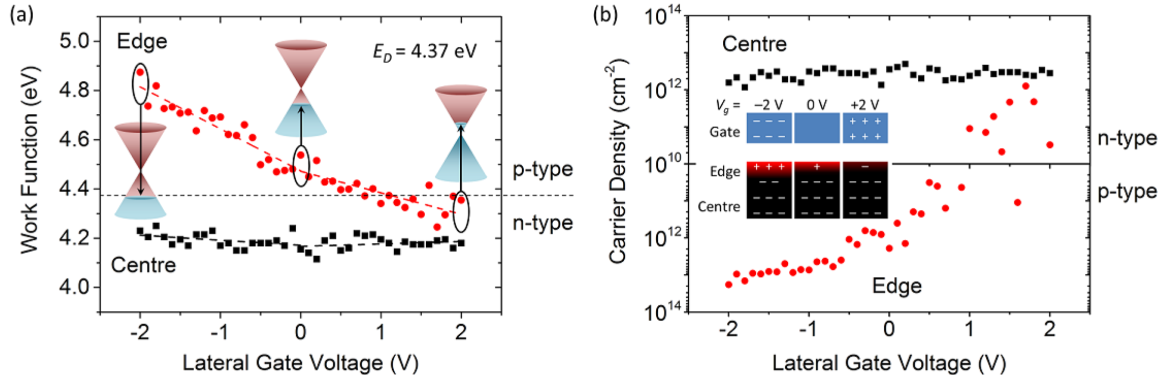

Figure 6.2: (a) The lateral gating effect on (a) work function and (b) carrier density of device #4a at the centre (black squares) and $\sim 30\,nm$ from the edge (red circles) of the channel. The insets in (a) and (b) show schematics of 1LG band structure and charge distribution in the channel.

minimum conductivity (Dirac point) was achieved with $V_g \sim +1\,V$. It should be noted that the scattering of the data points for $V_g > 0$ appears to be more significant than the data points for $V_g < 0$ in Fig. 6.2b, which is related to the fact that the carrier density is plotted on a logarithmic scale.

The behaviour of the carrier density can be understood from electrostatic point of view. For instance, electrons accumulate in the gates when $V_g < 0$, attracting more holes towards the edge of the channel (Fig. 6.2b inset). As the work function is the minimum energy required to remove an election from the Fermi surface to a point just outside the material, larger energy is require to remove an electron from a material that has a lower electron carrier density. For $V_g > 0$, holes accumulate in the gates, attracting electrons towards the edge of the channel. This increases the electron carrier density and lowers the work function. Thus, the experimental results are consistent with carrier density behaviour from an electrostatic point of view.

6.1.3 Gating effect on bulk electronic properties

The effect of lateral gates was also studied during transport measurements to investigate its possible influence on the bulk electronic properties of devices #4a, #4c and #4d. R_4 (Fig. 6.3b inset) measurements were conducted at $V_g = -5$ to $+5\,V$ applied to the lateral gates. Fig. 6.3a shows the dependence of the change in resistance, $\Delta R_4 = R_4(V_g) - R_4(V_g = 0)$, on the lateral gate voltage for device #4a. ΔR_4 could be modified by up to $\sim \pm 15\,\Omega$ for $V_g = \mp 5\,V$, which accounts for $\sim 0.3\%$ of the total

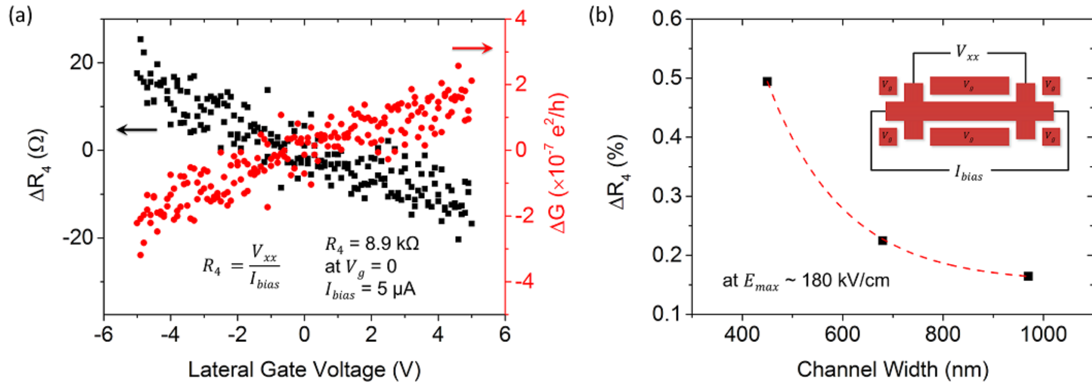

Figure 6.3: (a) The lateral gating effect on change in channel resistance and conductance of device #4a. (b) The dependence of ΔR_4 on channel width at $E_{max} \sim 180\,kV/cm$. The inset in (b) shows the schematic for R_4 measurements.

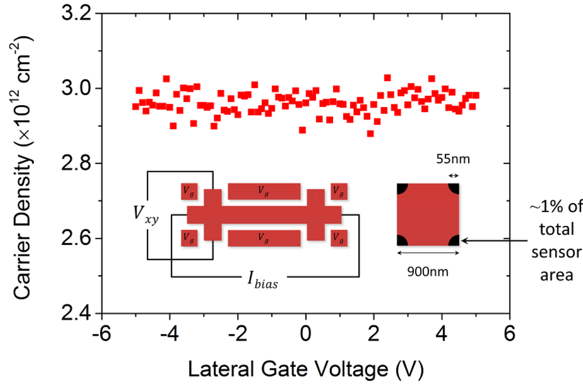

Figure 6.4: The lateral gating effect on carrier density of device #4a. Inset shows the schematic for carrier density measurements.

resistance of the channel ($R_4 = 8.9\,k\Omega$). The conductance was also determined for the channel, where $G = R^{-1} = 1.1 \times 10^{-4}\, e^2/h$ and $\Delta G = G(V_g) - G(V_g = 0)$ is on the order of $10^{-7}\, e^2/h$. At first, this may not seem very compelling, however it should be noted that carrier density for only $\sim 10\%$ of the total channel width ($970\,nm$) was affected at $V_g = -2\,V$ (Section 6.1.1). Decreasing the channel width will result in the affected area of the channel accounting for a larger percentage of the total area. Measurements conducted on narrower channels have shown an exponential increase in the lateral gating effect, where ΔR_4 changed by up to $\sim 1\%$ for $450\,nm$ wide channel (Fig. 6.3b). In literature, measurements conducted on devices with widths down to 10's of nanometres have shown lateral gating to be considerably more effective [191–194]. Furthermore, back/top gates have been used in conjunction with lateral gates to fine-tune the carrier density around the Dirac point [191–193], thereby further enhancing the lateral gating effect. Carrier density measurements conducted in the Hall bar geometry on device #4a showed no observable dependence on the lateral gate voltage (Fig. 6.4). However, this is not so surprising as the measurement was conducted in the Hall geometry, where only $\sim 1\%$ of the total sensor area of a $970\,nm$ wide cross is affected by the lateral gates (Fig. 6.4 inset).

6.1.4 Leakage current

The magnitude of the current leaking (I) through the SiC substrate was investigated on device #4a to account for its effect on the electronic properties of the device. The measurement circuit consisted of an ammeter, the voltage source and the lateral gate device in series (Fig. 6.5 inset). The leakage current was determined by measuring I

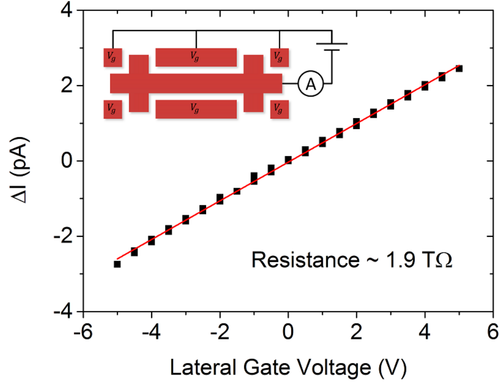

Figure 6.5: Dependence of the current leaking through the SiC substrate on the applied lateral gate voltage for device #4a. Inset shows the electrical circuit for the leakage current measurement. $\Delta I = I(V_g) - I(V_g = 0)$. Red dashed line is a linear fit to the data.

at V_g and subtracting it against I at $V_g = 0$ after each individual $I(V_g)$ measurement: $\Delta I = I(V_g) - I(V_g = 0)$. In this instance, the normalisation is vital for accurate leakage current measurements as the insulating nature of SiC leads to significant charging. The measurement reveals a linear I-V_g relationship for V_g up to $\pm 5\ V$ with channel-gate resistance of $\sim 1.9\ T\Omega$ (Fig. 6.5). During the transport measurements, a maximum of $|\Delta I| \sim 2.5\ pA$ was leaking through the substrate at $V_g = \pm 5\ V$. Compared to the bias currents used for R_4 and n measurements, the leakage current is at least six orders of magnitude smaller, insuring maximum efficiency of the electric fields created by the lateral gates. Thus, ruling out a possibility to affect the lateral side effect measurements.

6.2 Electrical scanning gate

This section describes the investigations of longitudinal (V_{xx}) and transverse voltage (V_{xy}) response of Hall bar devices to local electric fields by the means of SGM and SGS technique described in Section 4.4. Both techniques were performed with DC voltages (up to $V_{probe} = \pm 10\ V$) applied to the SCM-PIT probes. The oscillating cantilever produces an *electric field gradient* (dE/dz) that locally affects the carrier density of the graphene, altering the characteristics of the device. These changes were accurately measured with a lock-in amplifier referenced to the drive frequency of the cantilever (f_0). In addition, non-oscillating SGM and SGS were also performed to investigate the effects of a DC electric field on V_{xx}.

6.2.1 Electrostatic effects in uniform 1LG and 2LG devices

FM-KPFM was first used to study the uniformity of the graphene layer thickness for 1LG and 2LG device (#4e and #4f, respectively). The V_{CPD} maps confirmed that while the 1LG device was indeed 100% uniform, the 2LG device had small patches of 1LG, making it $\sim$ 95% uniform 2LG for the area of the channel within the two V_{xx} leads (Fig. 6.6a). Field gradient SGM measurements were performed with $I_{bias} = 50\ \mu A$, $V_{probe} = -5\ V$ and $20\ nm$ lift height, mapping the dV_{xx}/dz response of both devices with a lock-in amplifier (Fig. 6.6b). For both devices, the dV_{xx}/dz increased for probe gating on the channel, *i.e.*, between the two V_{xx} measurement arms. This indicates that

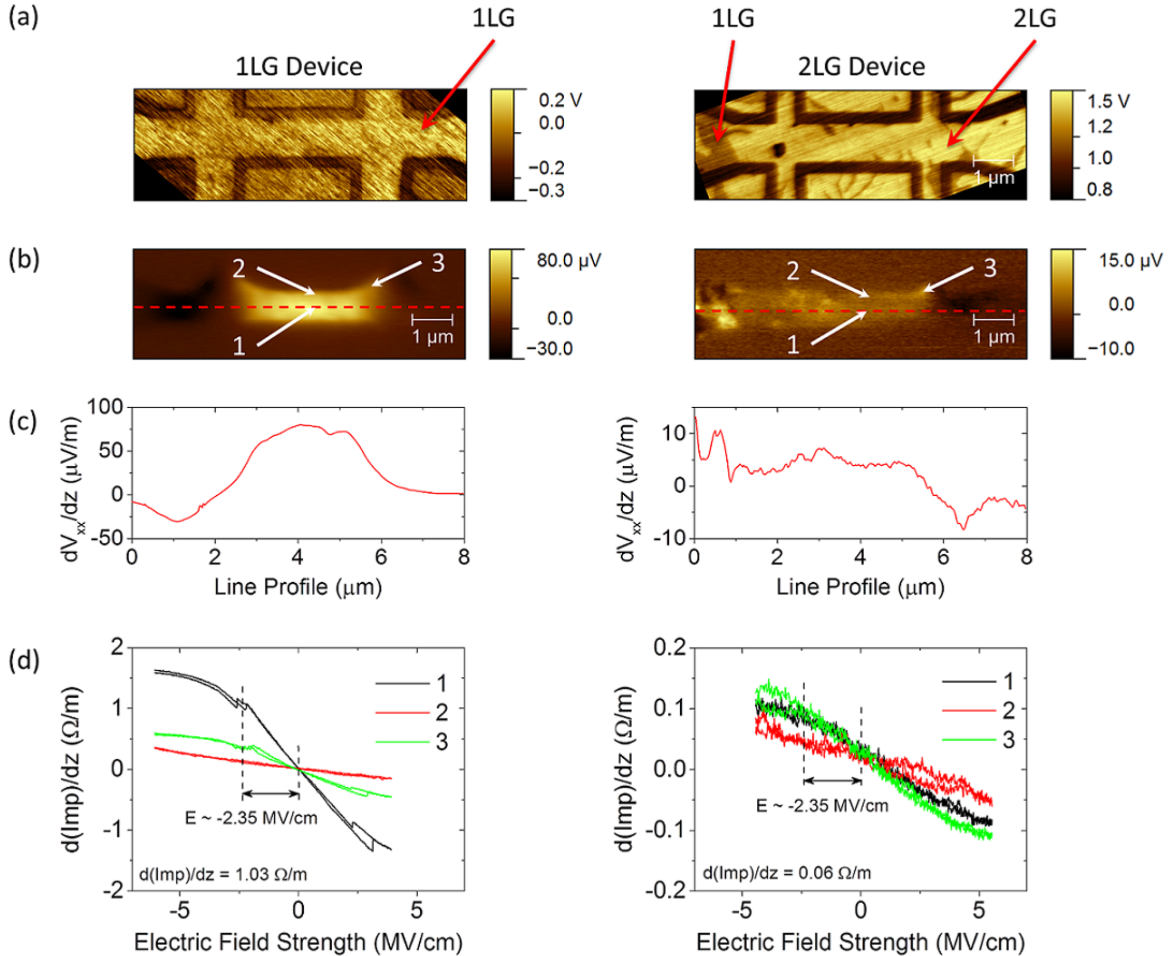

Figure 6.6: Measurements on uniform 1LG and 2LG devices (#4a and #4e, respectively). (a) Surface potential maps performed at $I_{bias} = 0$, and (b) electrical SGM maps of dV_{xx}/dz performed at $I_{bias} = 50\ \mu A$, $V_{probe} = -5\ V$ and $20\ nm$ lift height. (c) Line profiles of the dV_{xx}/dz maps along the dashed line at the centre of the channels indicated in (b). (d) $d(Imp)/dz$ obtained with SGS performed at the three locations indicated in (b).

negative V_{probe} locally decreases the carrier density, which increases the total resistance of the channel, thereby increasing dV_{xx}/dz. The dV_{xx}/dz line profile along the dashed line indicated in Fig. 6.6b for the 1LG device clearly shows that maximum coupling to the local gate occurs when the probe is positioned at the centre of the channel (Fig. 6.6c). However, identical analysis of the measurement on 2LG device shows that gating effect is considerably uniform across the area of the channel (Fig. 6.6c).

To further understand the dependence of V_{probe} (and subsequently the electric field strength) on the channel resistance, SGS measurements were performed on both devices for V_{probe} up to $\pm 10\,V$ at three locations indicated in Fig. 6.6b. However, as we are measuring dV_{xx}/dz at $\sim 70\,kHz$, dividing the voltage by I_{bias} gives the derivative of the impedance ($d(Imp)/dz$). Measurements show that $d(Imp)/dz$ is linear only for $E \sim \pm 2.35\,MV/cm$ (Fig. 6.6d). The gating effect is largest at the centre of the channel (position 1) for the 1LG device, whereas for 2LG device, the effects of gating at the three locations are almost identical (Fig. 6.6d). These SGS results are consistent with previous observations from SGM images (Fig. 6.6b). As the dielectric between the graphene and the probe is simply ambient air during these experiments, non-linearity in $d(Imp)/dz$ shows possible signs of electrical breakdown of the air at $|E| > 2.35\,MV/cm$. For 2LG device, the non-linearity is much less pronounced than that of 1LG device.

In order to assess the gating efficiency, the ratio $\frac{d(Imp)/dz}{R_s}$ can be compared for the 1LG and 2LG devices. In Section 5.6, it was shown that from 1LG to 2LG, a 4 times increase in the carrier density results in a 4 times decrease in R_4, where $R_s^{1LG} = 2.28\,k\Omega$ and $R_s^{2LG} = 0.49\,k\Omega$, respectively. For the 1LG device, $d(Imp)/dz = 1.03\,\Omega/m$ for position 1, which gives a ratio of 4.51×10^{-4}. If we are to assume the same ratio and that 2LG device is simply a material with a 4 time larger carrier density, estimations show that identical $|E| \sim 2.35\,MV/cm$ should result in $d(Imp)/dz = 0.22\,\Omega/m$. However, the measurements show that $d(Imp)/dz = 0.06\,\Omega/m$ at position 1, giving a ratio of 1.22×10^{-4}, which is a further 3.7 times lower than the estimate. This comparison shows that gating effect on 2LG device is reduced by $\sim 73\%$ in relation to 1LG, indicating to substantial screening of the electric field due to Coulomb interactions. The magnitude of the electric field screening is therefore strongly related to the carrier density of 2LG. For example, Castro *et al.* showed that increasing the carrier density of 2LG from $n_e \sim 4$ to

$10 \times 10^{12}\,cm^{-2}$, while applying a perpendicular external electric field ($E_{ext} = 3\,MV/cm$) comparable to the present experiment, leads to an approximately linear decrease in the screened electric field from $E \sim 1.7$ to $1.4\,MV/cm$ [195].

6.2.2 Electrostatic effects of 2LG islands on 1LG device

6.2.2.1 Effects on channel resistance

The electrical gating effect was also investigated with the field gradient SGM for a 1LG device (#4c) containing a 2LG island in the middle of the channel, which was revealed using FM-KPFM (Fig. 6.7a). dV_{xx}/dz map of the device was obtained with SGM at $20\,nm$ lift height and $I_{bias} = +5\,\mu A$ with $V_{probe} = -5$ and $+5\,V$ (Fig. 6.7b and 6.7c, respectively). In a similar fashion to the uniform 1LG device #4e from Section 6.2.1, locally gating with $V_{probe} = -5\,V$ on the 1LG parts of the channel increases the device response by $dV_{xx}/dz = 4.8\mu V/m$ (Fig. 6.7b), indicating the channel resistance increases. However, when the probe is gating with on the 2LG part of the channel, the device response only increases by $dV_{xx}/dz = 1.6\,\mu V/m$. Whereas for gating with $V_{probe} = +5V$ on 1LG part of the channel decreases the device response by $dV_{xx}/dz = -4.2\,\mu V/m$ (Fig. 6.7c) and 2LG by $dV_{xx}/dz = -1.4\,\mu V/m$.

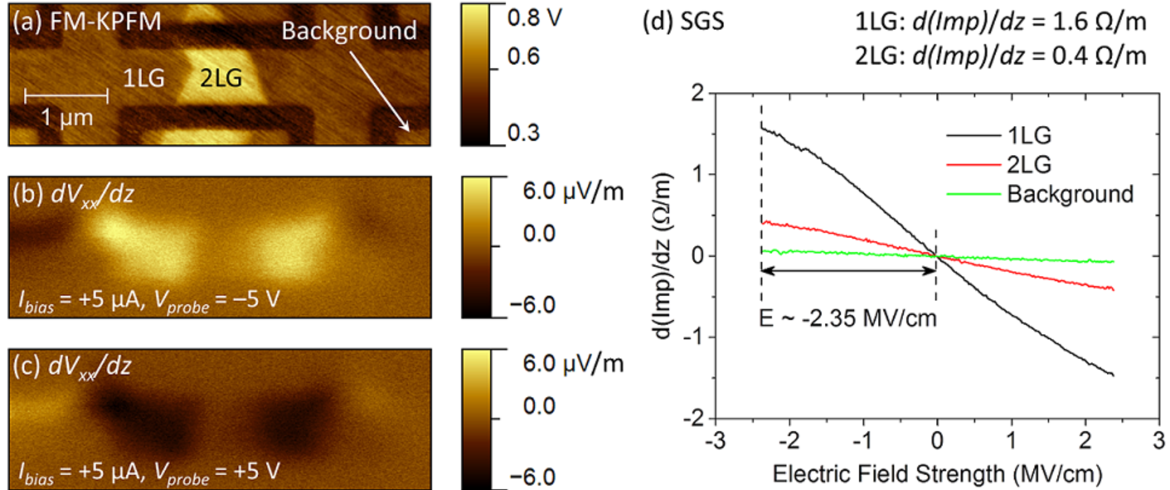

Figure 6.7: (a) Surface potential map of the $680\,nm$ device #4c performed at $I_{bias} = 0$. Electrical SGM maps of dV_{xx}/dz performed at $20\,nm$ lift height with $I_{bias} = +5\,\mu A$, (b) $V_{probe} = -5\,V$ and (c) $V_{probe} = +5\,V$. (d) $d(Imp)/dz$ obtained with SGS performed at the three locations indicated in (a).

SGS measurements performed on 1LG, 2LG and background part of the device shows that, while gating on the background has negligible effect on the channel, gating on 1LG and 2LG at $E \sim 2.35\ MV/cm$ produces $d(Imp)/dz = 1.6$ and $0.4\ \Omega/m$, respectively (Table 6.1). For an accurate comparison of the ratios, R_s must be separated for 1LG and 2LG, because: 1) the resistance of 1LG and 2LG are different and 2) the lock-in amplifier measures the total response of the device. With the total $R_4 = 10.6\ k\Omega$, the contribution from 1LG is $R_4^{1LG} = 9.78\ k\Omega$ and 2LG is $R_4^{2LG} = 0.82\ k\Omega$, thus giving us a sheet resistance of $R_s^{1LG} = 3.40\ k\Omega$ and $R_s^{2LG} = 0.73\ k\Omega$ for 1LG and 2LG, respectively (Table 6.1). Thus, taking the ratio $\frac{d(Imp)/dz}{R_s}$ gives 4.71×10^{-4} and $5.47 \times 10^{-4}\ m^{-1}$ for 1LG and 2LG, respectively (Table 6.1). Comparing the ratios for 1LG and 2LG shows that in this particular geometry, when the probe is located on the 2LG island at the centre of the channel, gating effect is increased by $\sim 16\%$ in relation to gating on 1LG (Table 6.1). However, this comparison is misleading as the local electric field affects the electronic properties over an area that is comparable to the size of the 2LG island. Therefore, gating on 2LG contains gating contributions from 1LG and vice versa. It should be noted that these measurements are performed at $\sim 70\ kHz$, therefore the gating efficiency is further complicated by the device inductance and probe-sample capacitance effects.

To account for such effects, the measurements were also performed on the same device #4c using the DC electric field SGM and SGS techniques described in Section 4.4. Fig. 6.8a and 6.8b shows the V_{xx} map of device #4c obtained with SGM at $20\ nm$ lift height and $I_{bias} = +5\ \mu A$ with $V_{probe} = -5$ and $+5\ V$, respectively. The maps show identical features to the force gradient technique, however, the voltage response of the device is considerably larger. To understand the dependence of R_4 on V_{probe}, SGS measurements were also performed at the same three locations indicated

Gating	R_4 ($k\Omega$)	$no\,of\,\Box's$	R_s ($k\Omega$)	$d(Imp)/dz$ (Ω/m)	ΔR_4 (Ω)	$\frac{d(Imp)/dz}{R_s}$ (m^{-1})	$\frac{\Delta R_4}{R_s}$
1LG	9.78	2.88	3.40	1.6	42	4.71×10^{-4}	1.24×10^{-2}
2LG	0.82	1.12	0.73	0.4	14	5.47×10^{-4}	1.92×10^{-2}
				Relative Change		+16%	+55%

Table 6.1: A summary of the measurements obtained with the electric field gradient and electric field SGS techniques.

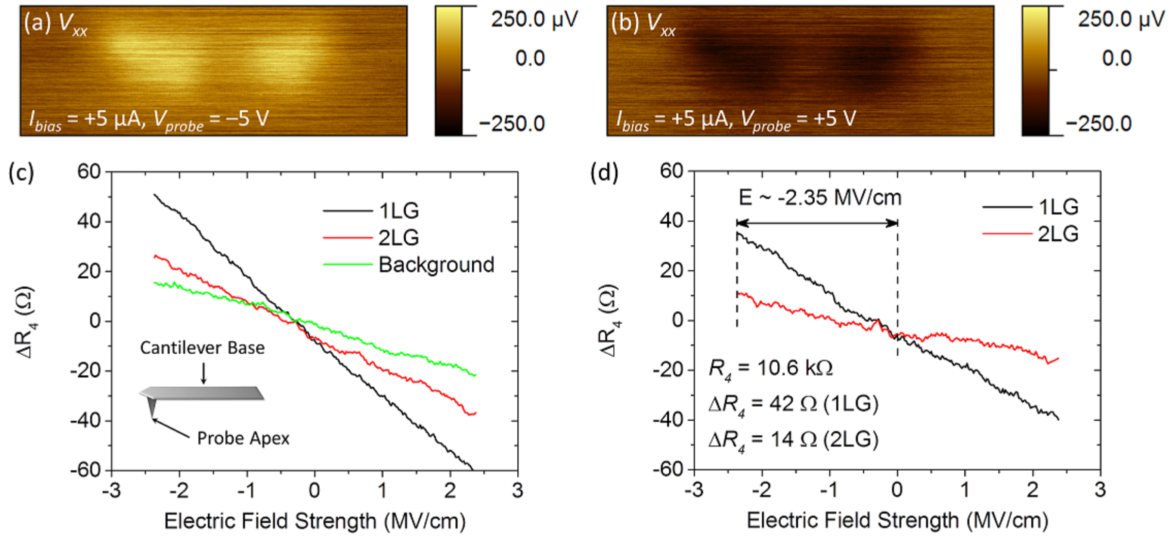

Figure 6.8: Electrical SGM maps of V_{xx} performed at $20\,nm$ lift height with $I_{bias} = +5\,\mu A$, (a) $V_{probe} = -5\,V$ and (b) $V_{probe} = +5\,V$. (c) ΔR_4 obtained with SGS performed at the three locations indicated in Fig. 6.7a. (d) ΔR_4 line profiles for 1LG and 2LG from (c) subtracted with the background measurement to account for gating effect from the cantilever base.

in Fig. 6.7a. Fig. 6.8c shows the dependence of ΔR_4 on electric field strength up to $E \sim \pm 2.35\ MV/cm$, where $R_4 = 10.6\ k\Omega$. Results show that, although gating on 1LG and 2LG has the largest affect on R_4, gating on the background also produces a relatively strong response. While the probe apex is at $20\,nm$ from the surface producing a strong electric field, the significantly larger area of the cantilever base is at $\sim 10\ \mu m$ from the surface, thus affecting the entire device with $\sim 10^3$ times smaller electric field ($E \sim 5\,kV/cm$ assuming parallel plate capacitor), even when the probe is gating on the background (Fig. 6.8c inset). However, as the contribution from the cantilever base is a global effect, the ΔR_4 for background was subtracted from ΔR_4 for 1LG and 2LG (Fig. 6.8d). Results show that gating with $|E| \sim 2.35 MV/cm$ increases the channel resistance by $\Delta R_4^{1LG} = 42\,\Omega$ and $\Delta R_4^{2LG} = 14\,\Omega$ for gating on 1LG and 2LG, respectively. Thus, taking the ratio $\frac{\Delta R_4}{R_s}$ gives 1.24×10^{-2} and 1.92×10^{-2} for 1LG and 2LG, respectively (Table 6.1). Comparing the ratios with each other shows that a DC electric field further increases the efficiency by $\sim 55\%$ for gating on the 2LG island. Similarly to the field gradient SGM technique, gating on the 2LG contains gating contributions from 1LG and vice versa. However, with the DC electric field being considerably less localised than field gradient SGM, the gating contribution from neighbouring graphene area is considerably larger. While the DC electric field SGM technique provides quantitative

analysis of the gating effect, it lacks the spatial resolution given by the electric field gradient SGM technique, making it less useful for observing nanoscale features.

6.2.2.2 Effects on transverse voltage

Furthermore, the electric field *gradient* effect on transverse voltage (dV_{xy}/dz) was also studied for the second cross of device #2a, which contains a long narrow patch of 2LG located in the active sensor area (Fig. 5.1). V_{xy} maps of the device were obtained at 25 nm lift height with all four combinations of $I_{bias} = \pm 100\ \mu A$ and $V_{probe} = \pm 5\ V$ (Fig. 6.9). Similar to the previous dV_{xx}/dz SGM experiments, no measurable dV_{xy}/dz response is observed when gating outside the geometrical boundaries of the device. The largest dV_{xy}/dz response with a two-fold symmetry is observed at the corners of the cross. This has been previously observed in various semiconductor systems and is related to the geometry of the device [161, 196]. For example, in the case of $I_{bias} = +100\ \mu A$ and $V_{probe} = -5\ V$ (Fig. 6.9b), the negative probe voltage repels electrons in the graphene, therefore the probe gating at corners 1 and 4 (Fig. 6.10a and Fig. 6.10d, respectively) diverts the flow of electrons towards V^- electrode, increasing V_{xy}. Similarly, if the probe is gating at corners 2 and 3 (Fig. 6.10b and Fig. 6.10c,

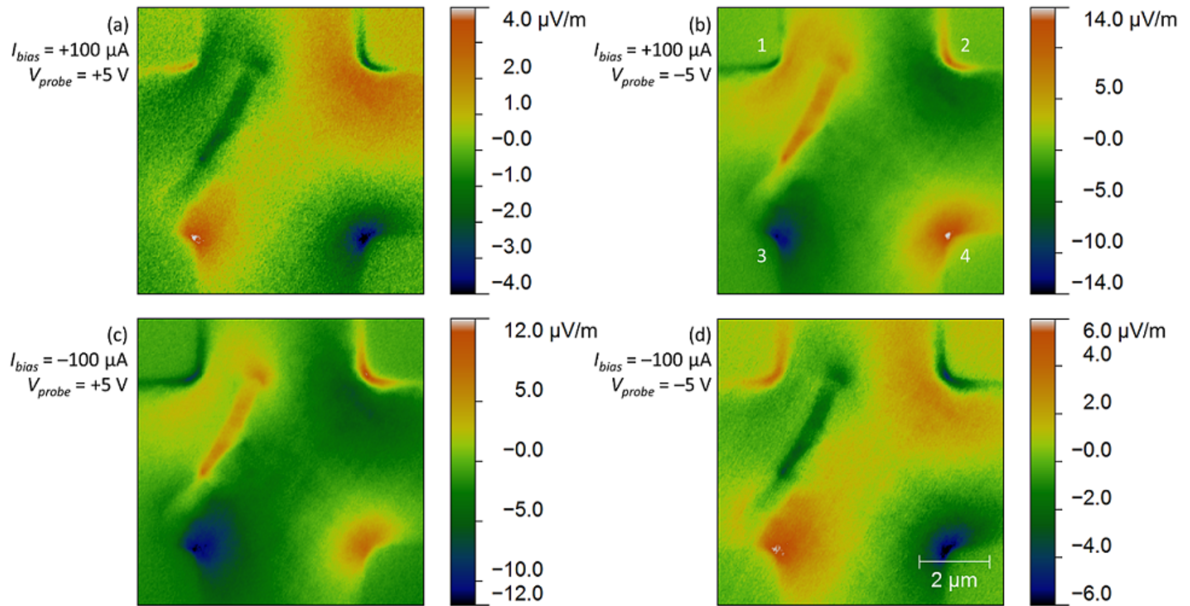

Figure 6.9: (a)-(d) Electric field gradient SGM of second cross of device #2a measuring dV_{xy}/dz at 25 nm lift height with all four combinations of $I_{bias} = \pm 100\,\mu A$ and $V_{probe} = \pm 5\,V$.

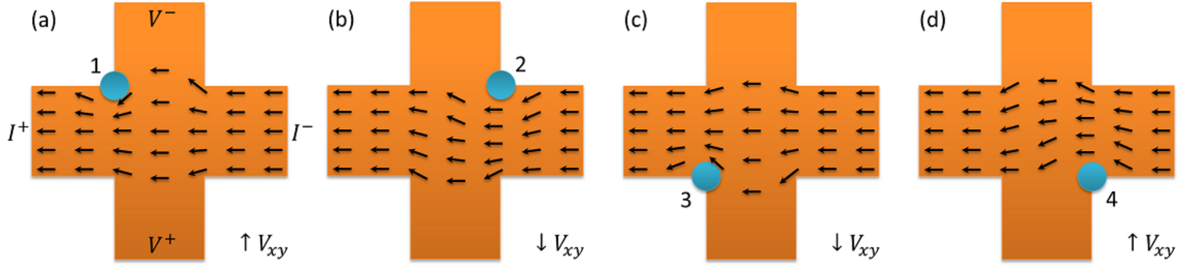

Figure 6.10: Schematic of the current distribution with locally gating with $V_{probe} < V_{CPD}$ at corners (a)-(d) 1-4 of a Hall sensor (corresponds to the case described in Fig. 6.9b). The blue circle represents the location of the probe and arrows represent the flow of electron.

respectively), the current flow is diverted towards V^+ electrode, decreasing dV_{xy}/dz. When measurements are performed with $I_{bias} = +100\mu A$ and $V_{probe} = +5V$, the positive V_{probe} attracts electrons towards the probe, inverting the contrast of the dV_{xy}/dz map (Fig. 6.9a). Furthermore, applying a negative bias current ($I_{bias} = -100\,\mu A$) reverses the direction of the flow of electrons, which also inverts the contrast for respective V_{probe} (Fig. 6.9c and Fig. 6.9d). The SGM dV_{xy}/dz map line profiles performed along the dashed line indicated in Fig. 6.11a inset, clearly shows that the magnitudes of the response at corner 4 is not symmetric for the four combinations of I_{bias} and V_{probe} (Fig. 6.11a), which is the result of differences in the probe-sample voltages. For example, largest difference between V_{CPD} and V_{probe} occurs when I_{bias} and V_{probe} are of opposite polarities, *i.e.*, $I_{bias} = \pm 100\,\mu A$ and $V_{probe} = \mp 5\,V$. Whereas, smallest difference between V_{CPD} and V_{probe} occurs when I_{bias} and V_{probe} are of the same polarity, *i.e.*,

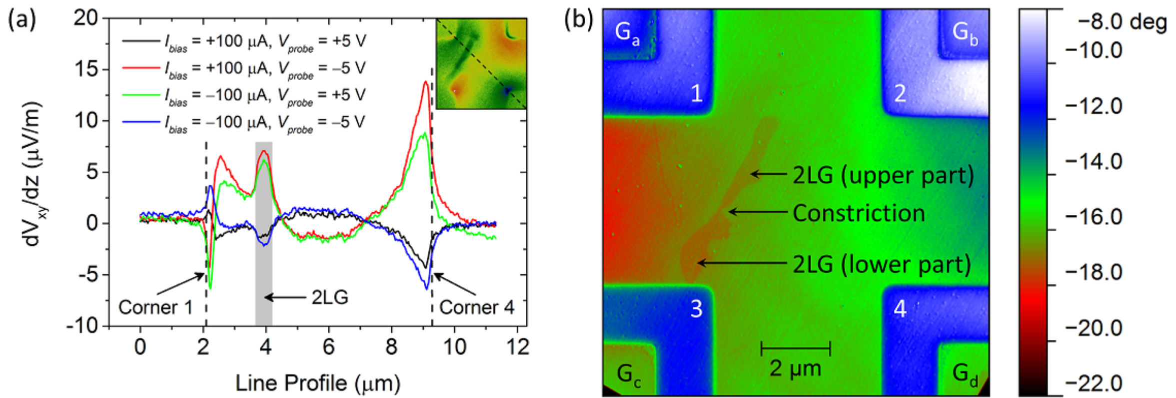

Figure 6.11: (a) SGM dV_{xy}/dz map line profiles at $I_{bias} = \pm 100\,\mu A$ and $V_{probe} = \pm 5\,V$ along the dashed line indicated in the inset image. (b) EFM image of device #2a at $I_{bias} = +100\,\mu A$ with gates G_a and G_b grounded and gates G_c and G_d floating.

$I_{bias} = \pm 100\,\mu A$ and $V_{probe} = \pm 5\,V$.

In addition to the two fold symmetry responses at the corners, a second contrast is also observed at the geometrical edge of corners 1 and 2 for all dV_{xy}/dz maps (Fig. 6.9). This contrast is related to a change in the electric field as a result of the grounded lateral gates $\mathrm{G_a}$ and $\mathrm{G_b}$, which appears as different contrast to the rest of the device in EFM phase imaging (Fig. 6.11b). Furthermore, the double contrast is not observed at corners 3 and 4 (Fig. 6.9) because the floating gates $\mathrm{G_c}$ and $\mathrm{G_d}$ do not create any additional electric fields.

There is also a change in contrast when probe is gating on the 2LG island. For example, the SGM contrast at the lower part of the 2LG island (Fig. 6.11b) is similar to that of background level for all combinations of I_{bias} and V_{probe} (Fig. 6.9), indicating that the 2LG screens the electric field produced by the probe. However, the line profiles of the SGM maps reveal that the SGM contrast at the upper part of the 2LG island is similar to the contrast at corner 1 (not referring to the second contrast in this case) (Fig. 6.11a). This indicates that locally gating on the upper part of the 2LG island has a similar effect to gating at corner 1 (Fig. 6.10). It should be noted that higher resolution EFM images revealed the width of the constriction between the upper and lower part of the 2LG island to be $\sim 120\,nm$, indicating both parts are electrically connected.

6.3 Magnetic scanning gate

This section describes the investigation of transverse voltage (dV_{xy}/dz) response of a Hall sensor to a local oscillating magnetic stray field emanating from a probe (dB_{probe}/dz) by the means of SGM technique described in Section 4.4. The measurements were conducted using MESP and MESP-HM probes (Table 4.1).

6.3.1 Elimination of electrostatic effects

The measurements were carried out on a $1\,\mu m$ wide device (#3a). Topography and surface potential mapping of device #3a shown in Fig. 6.12a and 6.12b, respectively, reveals that the device consists of only 1LG. It is important to note that the device here

has been cleaned of resist residues with the CM-AFM technique (Appendix C). The electrical properties of the device were characterised using the transport measurement technique described in Section 3.2, where $R_H = 1250\,\Omega/T$, $n_e = 5 \times 10^{11}\,cm^{-2}$ and $\mu_e = 1500\,cm^2/Vs$.

The magnetic stray field emanating from MESP and MESP-HM probes was measured by scanning and simultaneously mapping dV_{xy}/dz of a current-biased epitaxial graphene Hall sensor. The technique is essentially the same as electrical SGM, where dV_{xy}/dz responds to the electric field gradient, whereas with magnetic SGM, the dV_{xy}/dz should respond to the magnetic field gradient. Fig. 6.12c shows the dV_{xy}/dz response of device #3a (with $I_{bias} = 20\,\mu A$) to a MESP-HM probe. The image is largely dominated by a strong dV_{xy}/dz response at the corners of the device (position 2 in Fig. 6.12d), which is related to the electrostatic effect described in Section 6.2.2.2. The magnetic coating of the probe is also electrically conductive, therefore applying

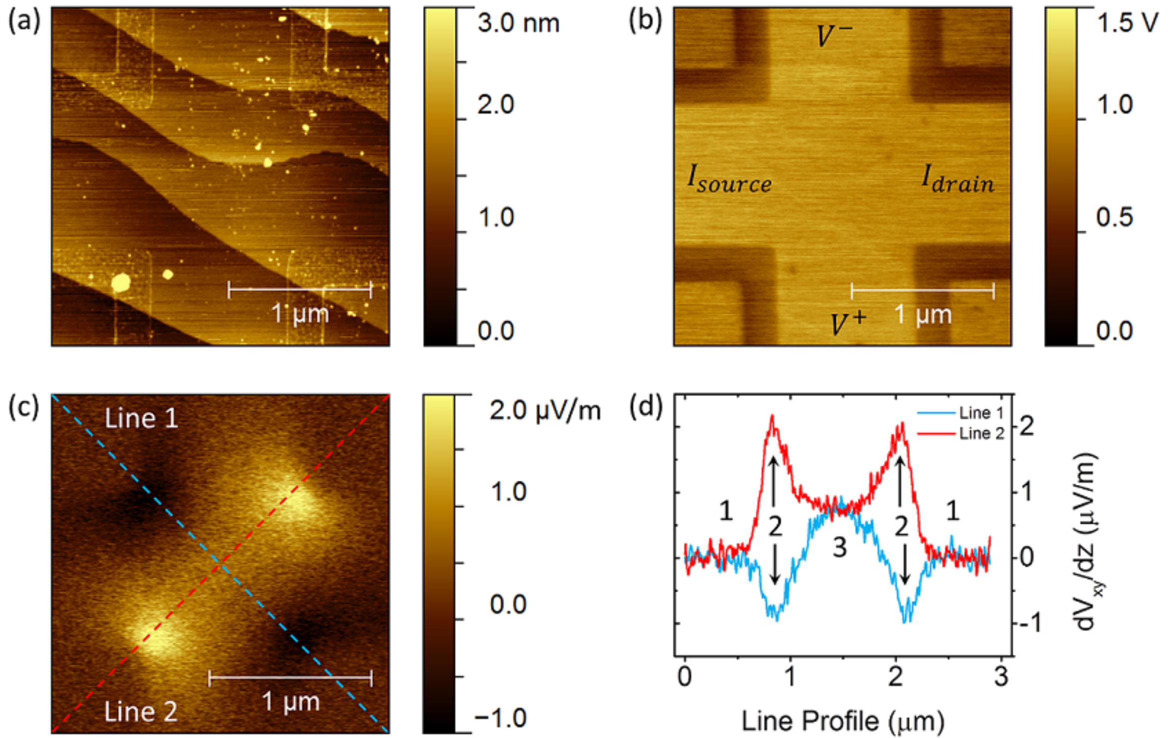

Figure 6.12: Images showing (a) topography and (b) surface potential mapping of device #3a. Red lines in (a) show the outline of the device. (c) The V_{xy} response of a Hall sensor ($I_{bias} = 20\,\mu A$) to electric and magnetic fields emanating from a MESP-HM probe. (d) Line profiles along the indicated dashed lines in (c), where 1: background, 2: electrostatic and 3: magnetic contributions.

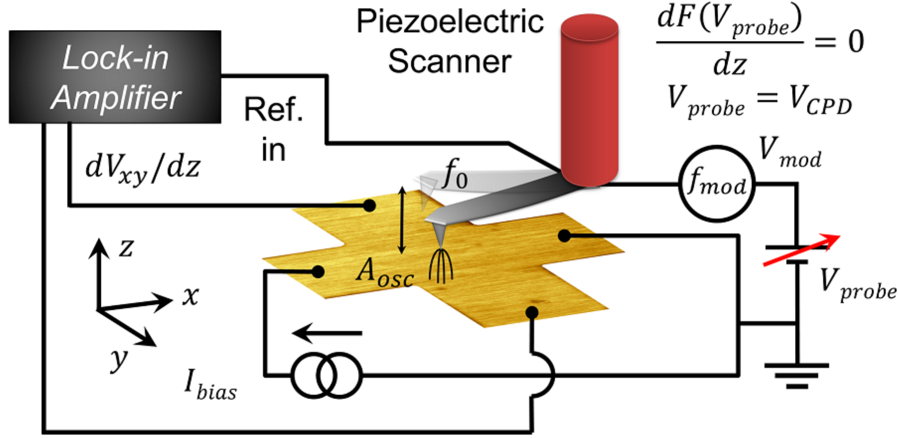

Figure 6.13: A schematic showing the magnetic stray field measurement setup. The probe is scanned across the sensor in FM-KPFM mode, while an external lock-in amplifier measures dV_{xy}/dz, which is fed back into the microscope and recorded at each pixel to produce a 2D map of the dV_{xy}/dz.

$I_{bias} = 20\,\mu A$ across the device raises the potential of the sensor area ($\sim 1\,V$). Furthermore, the grounded probe creates a potential difference between the probe and sample, thereby creating an electric field. This parasitic electric field makes it rather difficult to determine the contribution from the probe magnetic stray field only (position 3 in Fig. 6.12d).

The parasitic electric field can be eliminated by applying a potential to the probe that is equal to the potential of the sample in the sensor area [196]. However, the potential is not fixed across the sample and so this technique is only moderately effective at eliminating the electric field [197]. A more elegant way of eliminating the electric field is by applying a potential equal to the surface, at each individual pixel. The KPFM feedback loop performs this exact procedure to measure the surface potential (Section 4.3). The most accurate surface potential measurement technique (FM-KPFM, Sections 4.3.3 and 5.2) was used to eliminate the parasitic electric field (Fig. 6.13).

6.3.2 Magnetic response of uniform 1LG device

The dV_{xy}/dz response of device #3a to the magnetic field gradient (dB_{probe}/dz) emanating from MESP and MESP-HM probes (Table 4.1) oscillating with an amplitude of A_{osc} was measured. In essence, the technique operates on the Hall effect, where the lock-in amplifier measures the Hall voltage response of the device to the local magnetic

field. Fig. 6.14a and Fig. 6.14b shows the response for MESP-HM with magnetisation pointing down (↓) and up (↑), respectively, at $I_{bias} = 20\ \mu A$. The images show a small contribution from the electrostatic effects in the corners, indicating incomplete nullification of the electric field, however, the largest part of the response originates from the magnetic contributions. The largest response to the magnetic stray field is at the centre of the device due to a maximum coupling of the probe with the sensor area, where ↓ (↑) magnetisation at $A_{osc} = 20\ (10)\ nm$ produces a positive (negative) response of $dV_{xy}/dz = 1.08\,(-0.64)\,\mu V/m$ (Table 6.2). The response from MESP probe is expected

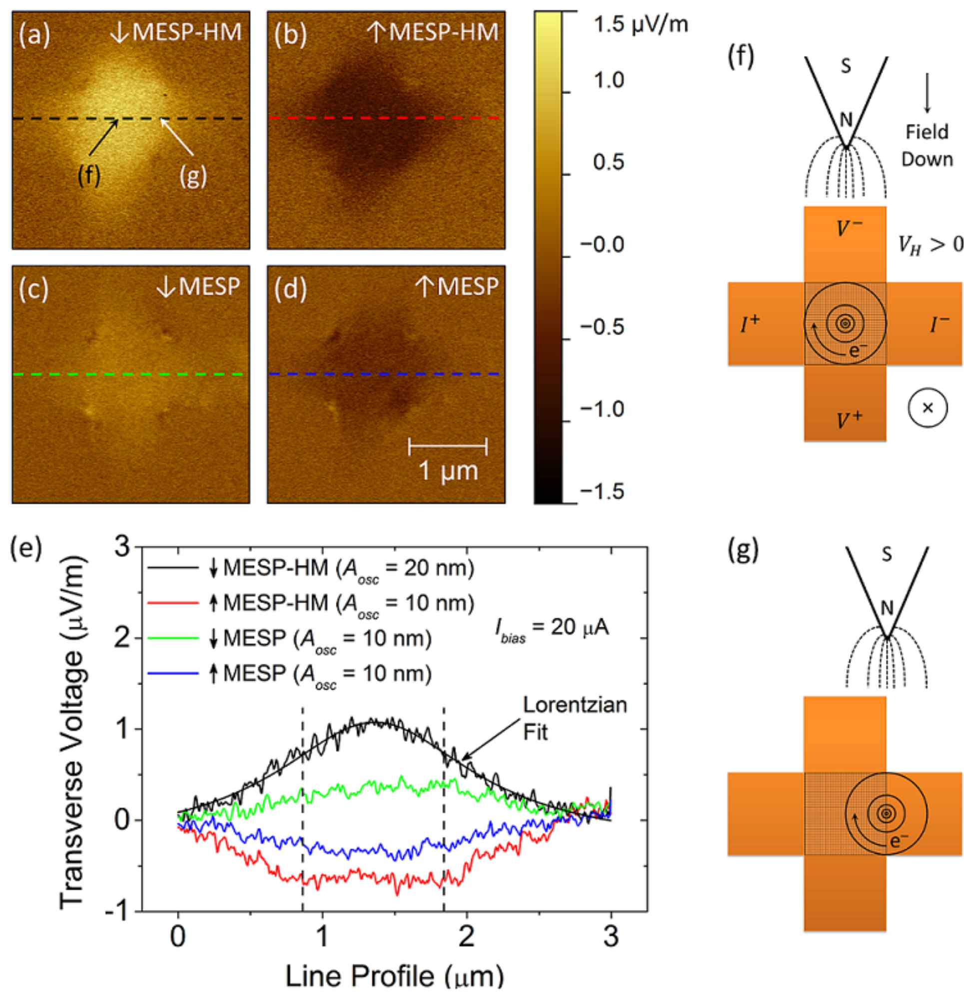

Figure 6.14: The dV_{xy}/dz response of a Hall sensor ($I_{bias} = 20\ \mu A$) to magnetic fields emanating from MESP-HM probe with magnetisation pointing (a) down (↓) and (b) up (↑) and for MESP probe with (c) down (↓) and (d) up (↑). (e) Line profiles along the indicated dashed lines of (a)-(d). $A_{osc} = 10\text{-}20\,nm$ is the oscillation amplitude at cantilever mechanical resonance f_0. The vertical dashed lines in (e) mark out the width of the cross. A schematic view of B_{probe} coupling when probe is gating at (f) the centre and (g) edge of the sensor area.

Probes	Moment (emu)	dV_{xy}/dz $[A_{osc}]$ $(\mu V/m)$ $[nm]$	dV_{xy}/dz $[A_{osc}]$ $(\mu V/m)$ $[nm]$
MESP-HM	$> 3 \times 10^{-13}$	$\downarrow 1.08$ [20]	$\uparrow -0.64$ [10]
MESP	$\sim 1 \times 10^{-13}$	$\downarrow 0.39$ [10]	$\uparrow -0.37$ [10]

Table 6.2: A summary of the maximum dV_{xy}/dz response to MESP and MESP-HM probes.

to be smaller due to a lower moment of $\sim 1 \times 10^{-13}\,emu$, where $\downarrow$ ($\uparrow$) magnetisation at $A_{osc} = 10\,nm$ produces a positive (negative) response of $dV_{xy}/dz = 0.39\,(-0.37)\,\mu V/m$. The line profiles along the indicated dashed lines in Fig. 6.14a-d are shown in Fig. 6.14e. Fit to the line profile from Fig. 6.14a reveals a clear Lorentzian response. For instance, the coupling of B_{probe} is maximum when the probe is gating at the centre of the cross (Fig. 6.14f) and gradually decreases as the probe moves away from the centre position (Fig. 6.14g). When the probe is located on the current arm outside the sensor area, the field gradient still influence the flow of charges, therefore producing a dV_{xy}/dz response.

6.4 Summary

In summary, the effects of lateral and top electrical gating on the channel resistance have been studied. The screening behaviour of 2LG was also investigated with electrical SGM and SGS. In addition, magnetic SGM was used in conjunction with FM-KPFM to study the response of a Hall sensor to a non-uniform magnetic field.

The effects of lateral gates on local transport properties of graphene device were studied using an electrically conductive probe with a calibrated work function. First, the surface potential distribution across the channel width was studied with FM-KPFM, revealing that positive V_g only affect the transport properties up to 20 nm from the lithographically defined edge of the channel, whereas negative V_g affects the transport up to 55 nm. Work function measurements with EFS at the *centre* of the channel revealed no observable change in transport properties as a result of the lateral gates. However, a total change of $\Delta\Phi_E \sim 0.5\,eV$ was measured at the *edge* of the channel. The lateral gating effect could be used to tune the conduction from holes to electrons with carrier densities $n_h = 1.8 \times 10^{13}\,cm^{-2}$ and $n_e = 1.3 \times 10^{12}\,cm^{-2}$, respectively. Although a relatively large edge effects were observed with the SPM techniques, complementary

bulk transport measurements revealed that the resistance of a 970 nm wide channel could be controlled by a total of only $\sim 0.3\%$. Identical measurements conducted on narrower channel of 450 nm width showed an increase in the lateral gating effect, where ΔR_4 could be controlled by a total of $\sim 1\%$. Leakage current measurements were used to characterise the channel-gate resistance $\sim 1.9\, T\Omega$, indicating that changes in electronic properties of the channel are the result of electrostatic gating.

The effects of electrostatic top gating on the impedance of uniform 1LG and 2LG devices were studied using the high spatial resolution qualitative SGM and SGS techniques. Mapping the $d(V_{xx})/dz$ of the devices showed negative (positive) voltages reduce (increase) the local carrier density, thereby increasing (decreasing) the overall impedance of the channel. The relative gating efficiency between 1LG and 2LG devices was assessed with SGS by taking the ratio of $\frac{d(Imp)/dz}{R_s}$. Results show a 73% *reduction* in the gating efficiency for *uniform* 2LG device, which indicates to substantial screening of the electric field.

Applying the same electric field gradient technique to a *non-uniform* EG device shows that locally gating on a 2LG *island* present on the channel significantly affects the total $d(Imp)/dz$ response of the device. However, the local electric field affects the electronic properties of the device over a significantly larger area, resulting in averaging of the gating effect. Thus, making it difficult to accurately assess the gating efficiency in the non-uniform EG device. While the electric field gradient technique provides qualitative information on the device, it also includes device impedance and probe-sample capacitance effects as the measurements are conduced at $\sim 70\, kHz$. Quantitative analysis of the DC resistance can be carried out using the electric field SGS. However, in the non-uniform EG device, averaging of the gating effect prohibits accurate assessment of the gating efficiency. The electric field screening behaviour was also observed with $d(V_{xy})/dz$ maps, where the screening depends on the location and geometry of the 2LG island.

A direct comparison for the efficiency of lateral and top electrical gating on the DC channel resistance can also be performed as measurements were conducted on the same 680 nm wide device. At identical gate voltages, the DC channel resistance was affected by $\sim 0.23\%$ and $\sim 0.43\%$ with lateral and top gating, respectively. Although

the probe only locally affects the channel surface, its close proximity at 20 nm results in a significantly larger electric field than in the lateral gate experiment. On the other hand, the lateral gates are considerably further away at 280 nm from the channel edge. The larger spacing results in a considerably smaller electric field, however affecting the edges along the entire length of the channel from both sides. The net result of close proximity and directly affecting the surface led to ~ 2 times larger efficiency with top gating.

The response of a Hall sensor to a local magnetic field was also studied using SGM. As the technique produces significant electrostatic responses in the transverse voltage due to the potential difference between the current-biased device and the electrically conductive magnetic coating of the MFM probe, the parasitic probe-sample potential difference was eliminated by the means of FM-KPFM feedback loop. The local magnetic response of the Hall sensor was studied with SGM performed *in situ* with FM-KPFM. The response of a 1 μm wide 1LG Hall sensor was mapped with the probes magnetised up and down. The transverse voltage of the Hall sensor responded positively with relation to the magnetic field pointing down and negatively for field pointing up. Under identical experimental conditions, 70% larger dV_{xy}/dz response was observed with MESP-HM probe compared to MESP, which is attributed to a thicker Co-Cr coating, producing a larger B_{probe}. Furthermore, increasing A_{osc} increases the magnetic field gradient, thereby further enhancing the Hall sensor response. This technique is ideal for measuring the stray magnetic field of MFM probes for calibrated MFM measurements.

Chapter 7

Conclusion and future outlook

The aim of this work has been to form a deep understanding of the unique electronic properties of EG. This has been achieved by applying various bulk (transport and noise) and local SPM techniques.

The bulk electronic properties of EG Hall sensors with size ranging from ~ 20 μm down to 100 nm were studied using transport and noise spectrum measurements at room temperature, in ambient conditions. On average, these devices exhibited low electron carrier density of $n \sim 8 \times 10^{11}\, cm^{-2}$, making them highly sensitive to magnetic fields. The carrier mobility remained independent on miniaturisation and showed that the EG devices were strongly diffusive with a mean free path of $\lambda \sim 30nm$. Furthermore, it was clearly demonstrated that, while $B_{min} \sim 2\,\mu T\sqrt{Hz}$ for devices of size $\geq 14.6\,\mu m$, the performance dropped to $B_{min} \sim 50\,\mu T\sqrt{Hz}$ for 100 nm devices. These devices consisted of long and narrow leads, which greatly contributed to the increase in total resistance and thus $1/f$ noise. Device geometry optimisations, such as widening of the voltage leads in all sections other than the sensor area, can potentially improve the noise performance.

The potential of EG devices for sensing application was realised by detecting the stray magnetic field emanating from a single 1 μm diameter magnetic Dynal bead with a moment of $4 \times 10^8\, \mu_B$. The AC/DC Hall magnetometry experiment, that had already been carried out on an InSb device of similar size and physical properties, would serve as an ideal comparison of the two different systems. The results showed that EG device response was $V_x^{AC} \sim 7\,\mu V$, whereas the InSb device was only $V_x^{AC} \sim$

$0.5\,\mu V$. The considerable improvement in the signal with the EG device is the result of improved bead-sensor coupling and a significantly larger biasing current. InSb device was fabricated out of a 300 nm thick epilayer, where the detection takes place from 0-300 nm below the surface of the material. However, in graphene the conduction takes place on the surface of the material due to its 2-dimensional nature, thereby greatly reducing the bead-sensor distance and improving the coupling. Deterioration of the InSb device electronic properties occurs at a modest bias current limit of $I_{bias} = 5\,\mu A$, whereas a similar size graphene channel can withstand biasing currents in excess of $I_{bias} = 1\,mA$. This large stability to bias current is related to an extremely effective electron-lattice interaction, which results in high carrier energy loss rate in graphene.

AFM maps of devices revealed a substantial amount of resist residues left over from the fabrication processes, contaminating the surface of EG. The latter prove to be difficult to remove using UV exposure and chemicals. However, these treatments led to an adverse affect of changing the conduction in graphene from electrons to holes. The technique of using CM-AFM to sweep the residues from side-to-side proved very effective on a small scale, thus restoring the typical n-type behaviour of EG.

SP mapping of EG is widely used to study the nanoscale electronic properties. However, depending on the technique used, *i.e.*, EFS, AM-KPFM or FM-KPFM, the results prove to be rather inconsistent. Having conducted a comprehensive comparison, the most accurate were the force gradient techniques, *i.e.*, EFS and FM-KPFM. The fact that force gradient is highly localised to the probe apex, measurements are not affected by the parasitic capacitance from the cantilever base, thus providing high spatial resolution ($< 20\,nm$) and accuracy. Furthermore, by normalising SP measurements using FM-KPFM, it was demonstrated that Au-graphene contact resistance is strongly non-Ohmic. Such investigations are typically conducted using the transmission line method, which require a specific device geometry, whereas FM-KPFM acts as a movable contactless probe, providing a direct measurement of the SP on any device geometry.

Work function of 1LG and 2LG was investigated with EFS, revealing $\Phi_{1LG} = 4.55 \pm 0.02\,eV$ and $\Phi_{2LG} = 4.44 \pm 0.02\,eV$, respectively, due to their unique band structures, where $\Delta\Phi_{1-2LG} = 110 \pm 21\,meV$. However, these values are directly related to

the carrier density and thus dictated by the growth procedure of EG (substrate/IFL doping) and atmospheric conditions (environmental doping). For example, EG in vacuum is strongly n-doped by the IFL, whereas introducing pure nitrogen p-doped EG from the surface, thus decreasing the electron carrier density. However, introducing EG to 100% relative humidity increases the electron carrier density beyond the level of IFL alone. The presence of 2LG islands on the device channel was also correlated with transport measurements. In essence, 2LG exhibits ~ 4 times larger carrier density than 1LG and can be regarded as islands with a lower resistance. Therefore, increase in percentage of 2LG resulted in a decrease in the channel resistance.

Lithographically defined edges of EG devices were shown to exhibit changes in the electronic properties. Calibrated work function measurements correlated with bulk transport revealed that, while bulk of the material remained n-doped, edges were in fact p-doped. This was attributed to protrusions appearing over the course of a few hours after the contact-mode AFM cleaning process, which indicates that p-doping molecules attach to the defective edges caused by the oxygen plasma etching process. These measurements clearly demonstrate the effectiveness of calibrated work function measurements. Furthermore, studies of the electronic properties by standard transport measurements require fabrication of devices such as Hall bars, which has been shown to contaminate the graphene. Here, non-invasive work function measurements can be carried out on bare EG samples to quantitatively study the electronic properties without a specific need for such devices.

Effects of lateral gating were studied with FM-KPFM, EFS and transport measurements. Surface potential and work function measurements demonstrated that lateral gates can affect the electrical properties of 1LG channel up to $\sim 55\,nm$ from the physical edge with carrier type tunable from p- to n-type. However, only a modest 1% change in the total resistance of a $450\,nm$ wide channel was observed. While lateral gates have a relatively weak effect on channel widths of several hundreds of nanometres, the electronic properties of sub $100\,nm$-wide devices could be significantly controlled as a larger portion of the total channel width will be affected. Lateral gates can also be useful for controlling the performance of devices in the quantum Hall regime, where the conduction takes place along the edges of the channel.

Effects of local electrical top gating on uniform 1LG, 2LG and non-uniform EG devices were studied using electric field gradient SGM and SGS techniques. Measurements on uniform 1LG and 2LG devices revealed a 73% reduction in the gating efficiency for the 2LG device, clearly indicating to screening of the external electric field. However, gating efficiency could not be accurately assessed for the non-uniform EG device due to the effective gating area comparable to the size of the 2LG island, resulting in averaging of the gating effect with neighbouring graphene. While electric field gradient SGM and SGS provide relative change of the device with a high spatial resolution, the measurements also include impedance and capacitance effects related to the $\sim 70\,kHz$ operation. On the other hand, electric field SGM and SGS were also used for *quantitative* study of the non-uniform EG device. However, although the device channel is locally gated by the probe apex with a large electric field ($E \sim 2.35\ MV/cm$), the cantilever base also affects the entire channel with $E \sim 5\ kV/cm$, leading to a substantial averaging of the gating effect with the entire device. These measurements provide some insight into different behaviours of uniform and non-uniform EG devices. However, a considerable amount of research is further required to fully understand the interactions between the top and bottom layer of the 2LG sandwich.

Effects of local magnetic top gating on a uniform 1LG device was studied using SGM with MFM probes, which are coated by a magnetic layer, producing a magnetic field gradient. Mapping the transverse voltage of the device revealed peaks that dominate the signal, which is typical for electrostatic gating. In this case, the magnetic coating of the probe is also electrically conductive, therefore creating a potential difference between the grounded probe and current biased device. The parasitic electrostatic response was eliminated by using the FM-KPFM feedback loop to apply a compensating voltage to the probe, effectively separating the magnetic response. The technique sets the foundations for study of magnetic response of non-uniform EG Hall sensors. In addition, the elimination of the electrostatic interactions is extremely important with MFM, where the long-range nature of the interactions can lead to strong correlations with electrostatic forces. Furthermore, accurate measurements of the probe stray magnetic fields are also important for calibrating the magnetic moment of the probe, which is useful for *quantitative* MFM imaging of magnetic domains.

The performance of EG devices exceeds ones fabricated out of CVD graphene, however, the performance of InSb epilayer devices of similar size and physical properties are marginally better at this current stage of development. The best graphene devices, however, are still ones fabricated out of mechanical exfoliated flakes from HOPG. Raman spectroscopy measurements have shown that, unlike EG, flakes contain very small number of crystalline defects, which results in their far superior carrier mobility. However, the major drawback of mechanically exfoliated flakes is their small size, which results in a low yield and limited scalability. CVD graphene can be grown in large quantities on substrates such as copper. However, the graphene must then be transferred onto an insulating substrate, which can lead to contamination and additional defects in the crystalline lattice. EG has the potential for mass production of graphene electronics as SiC wafers are readily available and compatible with the well-established CMOS technologies. Furthermore, EG does not require a transfer processes due to the insulating nature of SiC. However, the current high costs of SiC wafer and complicated growth procedure makes large scale production of EG electronics unattractive.

Future outlook | Graphene that is of low quality, affordable and easy to incorporate into existing applications, will most likely be the first to reach the end user in a few years. However, the key to successful implementation of graphene lies with novel applications that are specific to graphene. These applications will require extensive research and development, material of the highest quality and expensive fabrication methods, thus, will most likely take decades to reach the end user.

The results presented in this thesis sets out many directions for future work. For example, although it is clear that deep UV exposed resist residues can p-dope graphene, the exact mechanism is not fully understood. While the act of placing the sample in vacuum temporarily restores the n-type behaviour of EG, the p-doping nature of deep UV exposed residues gradually dominates. Therefore, it is clear that p-doping is caused by the adsorption of certain type(s) of molecules from ambient air, where the species are presently unknown. Furthermore, it remains to be seen weather UV exposed resist residues can be used to p-dope the top layer of the 2LG sandwich, while the IFL n-dopes the bottom layer. If such system could be established, a passive electric field could be maintained between the two layers, potentially opening up a band gap. The

correlation of bulk transport properties with nanoscale mapping techniques sets out a solid foundation for probing such effects not only in EG, but other materials as well.

The second direction of future work can be directed towards the screening behaviour of 2LG. While the measurements show a significant gating effect on the performance of EG devices, the exact mechanism of the gating efficiency for uniform and non-uniform 2LG is yet to be determined. Additional techniques, such as scanning capacitance microscopy and scanning spreading resistance microscopy, can also be used to further clarify the coupling in 2LG and it effects on screening.

The third direction of future work could involve exploiting laterally gated devices to control the edge states in graphene, which can play a significant role in nanoribbons, governing their performance. While measurements have shown a significant change in material properties at the edges of devices, lateral gates could be used to alter the characteristics of these devices and improve their performance. The edge states also play a significant role in the quantum Hall regime, where the lateral gates could be used to control the electronic properties at the edges, potentially providing an extra degree of freedom for understanding and optimisation of the QHE.

Due to the massless Dirac characteristics of the carriers in graphene, new and exciting phenomena such as quasi-bound states, particle collimation, relativistic Klein tunnelling and planar electron Veselago lensing are predicted to occur in graphene junction devices due to the unique energy band structure. While top gates can be used to electrically gate devices, fabrication typically involves deposition of a dielectric material, which can degrade material properties of graphene, such as carrier mobility. Here, the photochemically gated passive planar p-n junction could prove to be useful as the carrier mobility is barely affected.

While all these are just a few directions for future work originating from various experiments presented in this thesis, the reality is, graphene remains a hot topic for other applications such as detection of small moments, chemical sensing, resistance standard, transparent and flexible electronics, composite materials, batteries, super-capacitors, hydrogen storage and many more...

Appendix A - Fabrication

The EG sample (#1) was grown by the Linköping group using high temperature (2000 °C) sublimation of Si from $4H$-SiC(0001) substrate at argon gas pressure of 1 bar, producing nominally 1LG [37, 198]. The devices were fabricated using the cleanroom facilities at Chalmers University, Sweden, using a three stage process involving various steps of electron beam lithography (EBL) in conjunction with electron beam evaporation and oxygen plasma etching.

The first step involved defining the bonding pads using poly(methyl methacrylate)/methyl methacrylate [PMMA/MMA] (250 nm thick) and ZEP520 (200 nm thick) resists, which were spin coated and baked on the $7 \times 7\, mm^2$ EG sample, followed by EBL to define the bonding pads. The ZEP520 and PMMA/MMA were developed using o-Xylene (96%) and H_2O/IPA (7 : 93 ratio), respectively, followed by oxygen plasma to etch the graphene. Cr/Au (5/100 nm) was deposited over the entire sample using electron beam evaporation. The unwanted metal was removed by lift-off performed in acetone, thus forming the bonding pads with excellent adhesion to the substrate (Fig. A.1a). The second step involved defining the leads (Fig. A.1a), which were formed in similar fashion to the first step, however with the crucial absence of oxygen plasma etching to ensure the metal is in a direct electrical contact to the graphene. The third and final step involved defining the Hall bars using the same resist recipe as the previous two steps. EBL was used to write the Hall bar pattern in the resist, exposing the unwanted regions of the device. The resists were developed using the same recipe as the previous two steps, exposing the unwanted regions of the graphene, while leaving behind the resist in the shape of Hall bars and leads (Fig. A.1b). Oxygen plasma was used to etch away the unwanted graphene, forming devices with the cross size ranging from 0.1-19.6 μm (Fig. A.1c).

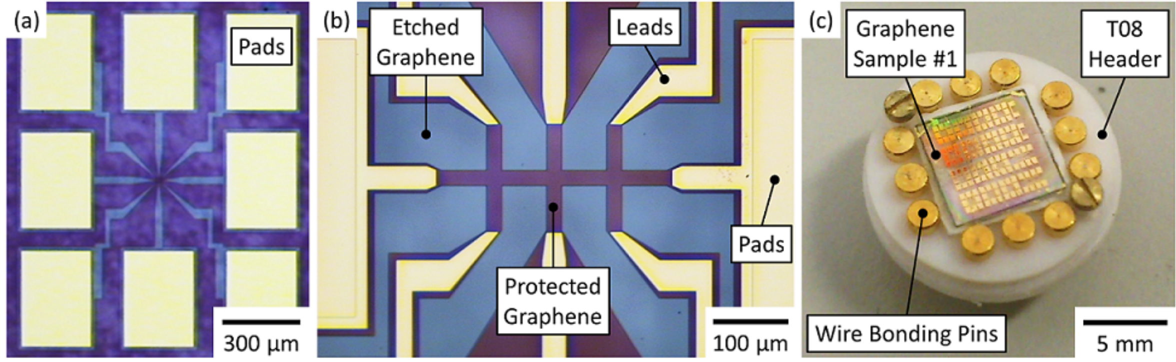

Figure A.1: (a) Optical image showing the bonding pads with resist patterned in the shape of the leads. Image was taken prior to evaporating Cr/Au leads. (b) Optical image of a 19.6 μm wide device showing the bonding pads, leads and the patterned resist protecting the graphene. Image was taken at the end of the third step fabrication step. (c) Image of the completed sample mounted on a 12-pin TO-8 header.

Sample	Device	Size [Gate] (nm)	Section	% of 2LG Cross1/Cross2/Channel
G197 (#1)	14 total	100-19600	3.2, 3.3	
	#1a	1600	3.5, 5.4.1	
G198 (#2)	#2a	4800	5.1, 5.2, 5.3, 5.5	6.6/7.9/5
G299 (#3)	#3a	1000	5.4.1	0/0/0
	#3b	1000	5.4.2	0/0/0
G366 (#4)	16 total	660-970	5.6, 6.3	
	#4a	970 [280]	5.7, 6.1.4	17.1/0/4.4
	#4b	910 [480]	6.1	0/50.7/4
	#4c	680 [280]	6.1, 6.2.1	0/0/28
	#4d	450 [280]	6.1	0/0/0
	#4e	900	6.2.1	0/0/0
	#4f	930	6.2.1	100/89.6/95

Table A.1: A summary of EG devices used throughout the thesis. Note: 0% of 2LG signifies uniform 1LG.

Appendix B - Bead-sensor coupling

The magnetic bead-sensor coupling constant was calculated as $c_{graphene} \sim 0.045$ by using [199]

$$c = \frac{R^3}{3w^2} \int_{(-w/2)}^{(w/2)} \int_{(-w/2)}^{(w/2)} \frac{2z^2 - (x-a)^2 - (y-b)^2}{[(x-a)^2 + (y-b)^2 + z^2]^{5/2}} dxdy. \quad (7.1)$$

where R is the bead radius ($0.5\ \mu m$), w is the cross width ($1.6\ \mu m$), a and b are the coordinates of the bead centre with respect to the Hall cross (-0.265 and $0.706\ \mu m$, respectively). $z = R + t$, where t is the distance between the sensor surface and middle of the 2DEG. In the present case, conduction takes places on the surface of graphene, therefore $t = 0$.

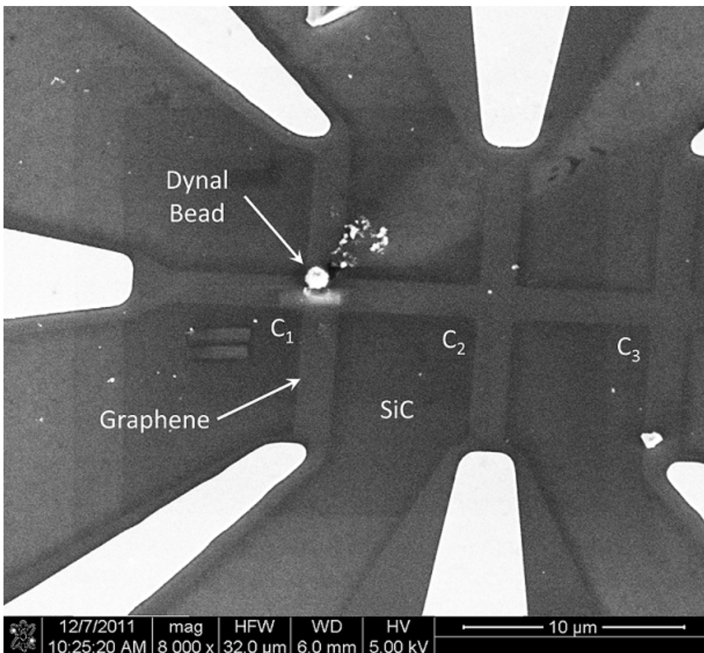

Figure B.1: Scanning electron micrograph of device #1a with a 1 μm diameter Dynal bead attached to the first cross. C_1, C_2 and C_3 denote Crosses 1, 2 and 3, respectively.

Appendix C - Atomic force microscopy cleaning

Contact-mode (CM-) AFM was used to raster scan the area with non-oscillating probes, while maintaining physical contact with the surface [200]. The map of the surface topography is obtained by adjusting the z-piezo to maintaining a set cantilever deflection (200-800 nm). In order to avoid physical damage of the sample, the scanning was conducted with the soft DNP-10 probes (Table 4.1). The act of scanning the sample in contact mode pushes the resist residues from side-to-side, gently cleaning the surface over the course of a few scans (Fig. C.1).

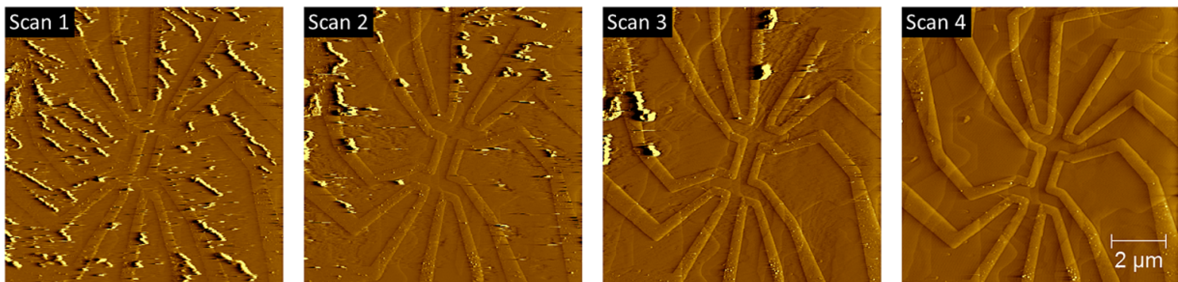

Figure C.1: Series of cantilever deflection error images showing the resist residues being swept from side-to-side. Colour scale range is 10 nm.

Bibliography

[1] “www.nobelprize.org,” 2013.

[2] K. S. Novoselov, A. K. Geim, S. V. Morozov, D. Jiang, Y. Zhang, S. V. Dubonos, I. V. Grigorieva, and A. A. Firsov, “Electric field effect in atomically thin carbon films,” *Science*, vol. 306, pp. 666–9, Oct. 2004.

[3] P. R. Wallace, “The band theory of graphite,” *Physical Review*, vol. 329, 1947.

[4] A. K. Geim and K. S. Novoselov, “The rise of graphene,” *Nature Materials*, vol. 6, pp. 183–91, Mar. 2007.

[5] A. H. Castro Neto, N. M. R. Peres, K. S. Novoselov, and A. K. Geim, “The electronic properties of graphene,” *Reviews of Modern Physics*, vol. 81, pp. 109–162, Jan. 2009.

[6] S. Das Sarma, S. Adam, E. Hwang, and E. Rossi, “Electronic transport in two-dimensional graphene,” *Reviews of Modern Physics*, vol. 83, pp. 407–470, May 2011.

[7] K. S. Novoselov, A. K. Geim, S. V. Morozov, D. Jiang, M. I. Katsnelson, I. V. Grigorieva, S. V. Dubonos, and A. A. Firsov, “Two-dimensional gas of massless Dirac fermions in graphene,” *Nature*, vol. 438, pp. 197–200, Nov. 2005.

[8] Y. Hancock, “The 2010 Nobel Prize in physics—ground-breaking experiments on graphene,” *Journal of Physics D: Applied Physics*, vol. 44, p. 473001, Nov. 2011.

[9] H. Min, B. Sahu, S. Banerjee, and A. MacDonald, “Ab initio theory of gate induced gaps in graphene bilayers,” *Physical Review B*, vol. 75, p. 155115, Apr. 2007.

[10] T. Ohta, A. Bostwick, T. Seyller, K. Horn, and E. Rotenberg, "Controlling the electronic structure of bilayer graphene," *Science*, vol. 313, pp. 951–4, Aug. 2006.

[11] E. Castro, K. Novoselov, S. Morozov, N. Peres, J. dos Santos, J. Nilsson, F. Guinea, A. Geim, and A. Neto, "Biased Bilayer Graphene: Semiconductor with a Gap Tunable by the Electric Field Effect," *Physical Review Letters*, vol. 99, pp. 8–11, Nov. 2007.

[12] J. B. Oostinga, H. B. Heersche, X. Liu, A. F. Morpurgo, and L. M. K. Vandersypen, "Gate-induced insulating state in bilayer graphene devices," *Nature Materials*, vol. 7, pp. 151–7, Feb. 2008.

[13] Y. Zhang, T.-T. Tang, C. Girit, Z. Hao, M. C. Martin, A. Zettl, M. F. Crommie, Y. R. Shen, and F. Wang, "Direct observation of a widely tunable bandgap in bilayer graphene," *Nature*, vol. 459, pp. 820–3, June 2009.

[14] Y. Zhang, Y.-W. Tan, H. L. Stormer, and P. Kim, "Experimental observation of the quantum Hall effect and Berry's phase in graphene," *Nature*, vol. 438, pp. 201–4, Nov. 2005.

[15] S. Stankovich, D. A. Dikin, G. H. B. Dommett, K. M. Kohlhaas, E. J. Zimney, E. A. Stach, R. D. Piner, S. T. Nguyen, and R. S. Ruoff, "Graphene-based composite materials," *Nature*, vol. 442, pp. 282–6, July 2006.

[16] K. S. Novoselov, Z. Jiang, Y. Zhang, S. V. Morozov, H. L. Stormer, U. Zeitler, J. C. Maan, G. S. Boebinger, P. Kim, and A. K. Geim, "Room-temperature quantum Hall effect in graphene," *Science*, vol. 315, p. 1379, Mar. 2007.

[17] J. C. Meyer, A. K. Geim, M. I. Katsnelson, K. S. Novoselov, T. J. Booth, and S. Roth, "The structure of suspended graphene sheets," *Nature*, vol. 446, pp. 60–3, Mar. 2007.

[18] A. K. Geim, "Graphene: status and prospects," *Science*, vol. 324, pp. 1530–4, June 2009.

[19] J.-H. Chen, C. Jang, S. Xiao, M. Ishigami, and M. S. Fuhrer, “Intrinsic and extrinsic performance limits of graphene devices on SiO2,” *Nature Nanotechnology*, vol. 3, pp. 206–9, Apr. 2008.

[20] X. Du, I. Skachko, A. Barker, and E. Y. Andrei, “Approaching ballistic transport in suspended graphene,” *Nature Nanotechnology*, vol. 3, pp. 491–5, Aug. 2008.

[21] F. Schwierz, “Graphene transistors,” *Nature Nanotechnology*, vol. 5, pp. 487–496, May 2010.

[22] K. Bolotin, K. Sikes, Z. Jiang, M. Klima, G. Fudenberg, J. Hone, P. Kim, and H. Stormer, “Ultrahigh electron mobility in suspended graphene,” *Solid State Communications*, vol. 146, pp. 351–355, June 2008.

[23] C. R. Dean, A. F. Young, I. Meric, C. Lee, L. Wang, S. Sorgenfrei, K. Watanabe, T. Taniguchi, P. Kim, K. L. Shepard, and J. Hone, “Boron nitride substrates for high-quality graphene electronics,” *Nature Nanotechnology*, vol. 5, pp. 722–6, Oct. 2010.

[24] K. Klitzing, G. Dorda, and M. Pepper, “New Method for High-Accuracy Determination of the Fine-Structure Constant Based on Quantized Hall Resistance,” *Physical Review Letters*, vol. 45, pp. 494–497, Aug. 1980.

[25] X. Li, W. Cai, J. An, S. Kim, J. Nah, D. Yang, R. Piner, A. Velamakanni, I. Jung, E. Tutuc, S. K. Banerjee, L. Colombo, and R. S. Ruoff, “Large-area synthesis of high-quality and uniform graphene films on copper foils,” *Science*, vol. 324, pp. 1312–4, June 2009.

[26] D. Stojanović, N. Woehrl, and V. Buck, “Synthesis and characterization of graphene films by hot filament chemical vapor deposition,” *Physica Scripta*, vol. T149, p. 014068, May 2012.

[27] Y. Gamo, A. Nagashima, M. Wakabayashi, M. Terai, and C. Oshima, “Atomic structure of monolayer graphite formed on Ni(111),” *Surface Science*, vol. 374, pp. 61–64, Mar. 1997.

[28] A. G. Starodubov, M. A. Medvetskii, A. M. Shikin, and V. K. Adamchuk, "Intercalation of silver atoms under a graphite monolayer on Ni(111)," *Physics of the Solid State*, vol. 46, pp. 1340–1348, July 2004.

[29] A. Reina, X. Jia, J. Ho, D. Nezich, H. Son, V. Bulovic, M. S. Dresselhaus, and J. Kong, "Large area, few-layer graphene films on arbitrary substrates by chemical vapor deposition," *Nano Letters*, vol. 9, pp. 30–5, Jan. 2009.

[30] K. S. Kim, Y. Zhao, H. Jang, S. Y. Lee, J. M. Kim, K. S. Kim, J.-H. Ahn, P. Kim, J.-Y. Choi, and B. H. Hong, "Large-scale pattern growth of graphene films for stretchable transparent electrodes," *Nature*, vol. 457, pp. 706–10, Feb. 2009.

[31] X. Li, Y. Zhu, W. Cai, M. Borysiak, B. Han, D. Chen, R. D. Piner, L. Colombo, and R. S. Ruoff, "Transfer of large-area graphene films for high-performance transparent conductive electrodes," *Nano Letters*, vol. 9, pp. 4359–63, Dec. 2009.

[32] A. L. Friedman, J. T. Robinson, F. K. Perkins, and P. M. Campbell, "Extraordinary magnetoresistance in shunted chemical vapor deposition grown graphene devices," *Applied Physics Letters*, vol. 99, no. 2, p. 022108, 2011.

[33] Y.-M. Lin, C. Dimitrakopoulos, K. A. Jenkins, D. B. Farmer, H.-Y. Chiu, A. Grill, and P. Avouris, "100-GHz transistors from wafer-scale epitaxial graphene," *Science*, vol. 327, p. 662, Feb. 2010.

[34] I. Forbeaux, J.-M. Themlin, and J.-M. Debever, "Heteroepitaxial graphite on 6H-SiC(0001): Interface formation through conduction-band electronic structure," *Physical Review B*, vol. 58, pp. 16396–16406, Dec. 1998.

[35] T. Kihlgren, T. Balasubramanian, L. Walldén, and R. Yakimova, "Narrow photoemission lines from graphite valence states," *Physical Review B*, vol. 66, p. 235422, Dec. 2002.

[36] C. Berger, Z. Song, T. Li, X. Li, A. Y. Ogbazghi, R. Feng, Z. Dai, A. N. Marchenkov, E. H. Conrad, P. N. First, and W. A. de Heer, "Ultrathin Epitaxial Graphite: 2D Electron Gas Properties and a Route toward Graphene-based Na-

noelectronics," *The Journal of Physical Chemistry B*, vol. 108, pp. 19912–19916, Dec. 2004.

[37] R. Yakimova, C. Virojanadara, D. Gogova, M. Syväjärvi, D. Siche, K. Larsson, and L. Johansson, "Analysis of the Formation Conditions for Large Area Epitaxial Graphene on SiC Substrates," *Materials Science Forum*, vol. 645-648, pp. 565–568, Apr. 2010.

[38] C. Dimitrakopoulos, Y.-M. Lin, A. Grill, D. B. Farmer, M. Freitag, Y. Sun, S.-J. Han, Z. Chen, K. A. Jenkins, Y. Zhu, Z. Liu, T. J. McArdle, J. A. Ott, R. Wisnieff, and P. Avouris, "Wafer-scale epitaxial graphene growth on the Si-face of hexagonal SiC (0001) for high frequency transistors," *Journal of Vacuum Science & Technology B: Microelectronics and Nanometer Structures*, vol. 28, no. 5, p. 985, 2010.

[39] H. Hibino, S. Tanabe, S. Mizuno, and H. Kageshima, "Growth and electronic transport properties of epitaxial graphene on SiC," *Journal of Physics D: Applied Physics*, vol. 45, p. 154008, Apr. 2012.

[40] N. Srivastava, G. He, P. C. Mende, R. M. Feenstra, and Y. Sun, "Graphene formed on SiC under various environments: comparison of Si-face and C-face," *Journal of Physics D: Applied Physics*, vol. 45, p. 154001, Apr. 2012.

[41] L. Johansson, S. Watcharinyanon, A. Zakharov, T. Iakimov, R. Yakimova, and C. Virojanadara, "Stacking of adjacent graphene layers grown on C-face SiC," *Physical Review B*, vol. 84, pp. 1–8, Sept. 2011.

[42] C. Riedl, C. Coletti, and U. Starke, "Structural and electronic properties of epitaxial graphene on SiC(0001): a review of growth, characterization, transfer doping and hydrogen intercalation," *Journal of Physics D: Applied Physics*, vol. 43, p. 374009, Sept. 2010.

[43] J. Eriksson, R. Pearce, T. Iakimov, C. Virojanadara, D. Gogova, M. Andersson, M. Syvajarvi, A. Lloyd Spetz, and R. Yakimova, "The influence of substrate morphology on thickness uniformity and unintentional doping of epitaxial graphene on SiC," *Applied Physics Letters*, vol. 100, no. 24, p. 241607, 2012.

[44] J. B. Hannon and R. M. Tromp, "Pit formation during graphene synthesis on SiC(0001): In situ electron microscopy," *Physical Review B*, vol. 77, p. 241404, June 2008.

[45] F. Hiebel, L. Magaud, P. Mallet, and J.-Y. Veuillen, "Structure and stability of the interface between graphene and 6H-SiC(0 0 0 1) (3 3): an STM and ab initio study," *Journal of Physics D: Applied Physics*, vol. 45, p. 154003, Apr. 2012.

[46] A. Van Bommel, J. Crombeen, and A. Van Tooren, "LEED and Auger electron observations of the SiC(0001) surface," *Surface Science*, vol. 48, pp. 463–472, Mar. 1975.

[47] F. Owman and P. Martensson, "STM study of the SiC(0001) 3 3 surface," *Surface Science*, vol. 330, pp. L639–L645, June 1995.

[48] S. Tanaka, K. Morita, and H. Hibino, "Anisotropic layer-by-layer growth of graphene on vicinal SiC(0001) surfaces," *Physical Review B*, vol. 81, p. 041406, Jan. 2010.

[49] P. Lauffer, K. V. Emtsev, R. Graupner, T. Seyller, and L. Ley, "Atomic and electronic structure of few-layer graphene on SiC(0001) studied with scanning tunneling microscopy and spectroscopy," *Physical Review B*, vol. 77, p. 155426, Apr. 2008.

[50] C. Virojanadara, R. Yakimova, A. A. Zakharov, and L. I. Johansson, "Large homogeneous mono-/bi-layer graphene on 6H–SiC(0 0 0 1) and buffer layer elimination," *Journal of Physics D: Applied Physics*, vol. 43, p. 374010, Sept. 2010.

[51] N. Srivastava, R. M. Feenstra, and P. J. Fisher, "Formation of epitaxial graphene on SiC(0001) using vacuum or argon environments," *Journal of Vacuum Science & Technology B: Microelectronics and Nanometer Structures*, vol. 28, no. 4, p. C5C1, 2010.

[52] J. Hass, W. A. de Heer, and E. H. Conrad, "The growth and morphology of epitaxial multilayer graphene," *Journal of Physics: Condensed Matter*, vol. 20, p. 323202, Aug. 2008.

[53] C. Riedl, A. A. Zakharov, and U. Starke, "Precise in situ thickness analysis of epitaxial graphene layers on SiC(0001) using low-energy electron diffraction and angle resolved ultraviolet photoelectron spectroscopy," *Applied Physics Letters*, vol. 93, no. 3, p. 033106, 2008.

[54] G. Gu, S. Nie, R. M. Feenstra, R. P. Devaty, W. J. Choyke, W. K. Chan, and M. G. Kane, "Field effect in epitaxial graphene on a silicon carbide substrate," *Applied Physics Letters*, vol. 90, no. 25, p. 253507, 2007.

[55] C. Virojanadara, M. Syväjarvi, R. Yakimova, L. Johansson, A. Zakharov, and T. Balasubramanian, "Homogeneous large-area graphene layer growth on 6H-SiC(0001)," *Physical Review B*, vol. 78, pp. 1–6, Dec. 2008.

[56] A. Tzalenchuk, S. Lara-Avila, A. Kalaboukhov, S. Paolillo, M. Syväjärvi, R. Yakimova, O. Kazakova, T. J. B. M. Janssen, V. Fal'ko, and S. Kubatkin, "Towards a quantum resistance standard based on epitaxial graphene," *Nature Nanotechnology*, vol. 5, pp. 186–9, Mar. 2010.

[57] V. Panchal, K. Cedergren, R. Yakimova, A. Tzalenchuk, S. Kubatkin, and O. Kazakova, "Small epitaxial graphene devices for magnetosensing applications," *Journal of Applied Physics*, vol. 111, no. 7, p. 07E509, 2012.

[58] D. Waldmann, J. Jobst, F. Fromm, F. Speck, T. Seyller, M. Krieger, and H. B. Weber, "Implanted bottom gate for epitaxial graphene on silicon carbide," *Journal of Physics D: Applied Physics*, vol. 45, p. 154006, Apr. 2012.

[59] C. Dimitrakopoulos, A. Grill, T. J. McArdle, Z. Liu, R. Wisnieff, and D. A. Antoniadis, "Effect of SiC wafer miscut angle on the morphology and Hall mobility of epitaxially grown graphene," *Applied Physics Letters*, vol. 98, no. 22, p. 222105, 2011.

[60] K. V. Emtsev, A. Bostwick, K. Horn, J. Jobst, G. L. Kellogg, L. Ley, J. L. McChesney, T. Ohta, S. A. Reshanov, J. Röhrl, E. Rotenberg, A. K. Schmid, D. Waldmann, H. B. Weber, and T. Seyller, "Towards wafer-size graphene layers by atmospheric pressure graphitization of silicon carbide," *Nature Materials*, vol. 8, pp. 203–7, Mar. 2009.

[61] M. Bolen, S. Harrison, L. Biedermann, and M. Capano, "Graphene formation mechanisms on 4H-SiC(0001)," *Physical Review B*, vol. 80, p. 115433, Sept. 2009.

[62] T. Filleter, K. V. Emtsev, T. Seyller, and R. Bennewitz, "Local work function measurements of epitaxial graphene," *Applied Physics Letters*, vol. 93, no. 13, p. 133117, 2008.

[63] X. Weng, J. A. Robinson, K. Trumbull, R. Cavalero, M. A. Fanton, and D. Snyder, "Epitaxial graphene on SiC(0001): Stacking order and interfacial structure," *Applied Physics Letters*, vol. 100, no. 3, p. 031904, 2012.

[64] T. Seyller, K. Emtsev, K. Gao, F. Speck, L. Ley, A. Tadich, L. Broekman, J. Riley, R. Leckey, O. Rader, A. Varykhalov, and A. Shikin, "Structural and electronic properties of graphite layers grown on SiC(0001)," *Surface Science*, vol. 600, pp. 3906–3911, Sept. 2006.

[65] J. Borysiuk, R. Bozek, W. Strupinski, A. Wysmołek, K. Grodecki, R. Stepniewski, and J. M. Baranowski, "Transmission electron microscopy and scanning tunneling microscopy investigations of graphene on 4H-SiC(0001)," *Journal of Applied Physics*, vol. 105, no. 2, p. 023503, 2009.

[66] T. Low, V. Perebeinos, J. Tersoff, and P. Avouris, "Deformation and Scattering in Graphene over Substrate Steps," *Physical Review Letters*, vol. 108, p. 096601, Mar. 2012.

[67] F. Ming and A. Zangwill, "Model and simulations of the epitaxial growth of graphene on non-planar 6H–SiC surfaces," *Journal of Physics D: Applied Physics*, vol. 45, p. 154007, Apr. 2012.

[68] M. Nagase, H. Hibino, H. Kageshima, and H. Yamaguchi, "Local conductance measurements of double-layer graphene on SiC substrate," *Nanotechnology*, vol. 20, p. 445704, Nov. 2009.

[69] M. Acik and Y. J. Chabal, "Nature of Graphene Edges: A Review," *Japanese Journal of Applied Physics*, vol. 50, p. 070101, July 2011.

[70] C. Vecchio, S. Sonde, C. Bongiorno, M. Rambach, R. Yakimova, V. Raineri, and F. Giannazzo, "Nanoscale structural characterization of epitaxial graphene grown on off-axis 4H-SiC (0001)," *Nanoscale Research Letters*, vol. 6, p. 269, Jan. 2011.

[71] S.-H. Ji, J. B. Hannon, R. M. Tromp, V. Perebeinos, J. Tersoff, and F. M. Ross, "Atomic-scale transport in epitaxial graphene," *Nature Materials*, vol. 11, pp. 114–9, Feb. 2012.

[72] T. L. Burnett, R. Yakimova, and O. Kazakova, "Identification of epitaxial graphene domains and adsorbed species in ambient conditions using quantified topography measurements," *Journal of Applied Physics*, vol. 112, no. 5, p. 054308, 2012.

[73] H. Hibino, H. Kageshima, and M. Nagase, "Epitaxial few-layer graphene: towards single crystal growth," *Journal of Physics D: Applied Physics*, vol. 43, p. 374005, Sept. 2010.

[74] C. Lee, Q. Li, W. Kalb, X.-Z. Liu, H. Berger, R. W. Carpick, and J. Hone, "Frictional characteristics of atomically thin sheets," *Science*, vol. 328, pp. 76–80, Apr. 2010.

[75] G. Prakash, M. L. Bolen, R. Colby, E. A. Stach, M. A. Capano, and R. Reifenberger, "Nanomanipulation of ridges in few-layer epitaxial graphene grown on the carbon face of 4H-SiC," *New Journal of Physics*, vol. 12, p. 125009, Dec. 2010.

[76] G. F. Sun, J. F. Jia, Q. K. Xue, and L. Li, "Atomic-scale imaging and manipulation of ridges on epitaxial graphene on 6H-SiC(0001)," *Nanotechnology*, vol. 20, p. 355701, Sept. 2009.

[77] Y. Yang, K. Brenner, and R. Murali, "The influence of atmosphere on electrical transport in graphene," *Carbon*, vol. 50, pp. 1727–1733, Apr. 2012.

[78] R. Pearce, T. Iakimov, M. Andersson, L. Hultman, A. L. Spetz, and R. Yakimova, "Epitaxially grown graphene based gas sensors for ultra sensitive NO2 detection," *Sensors and Actuators B: Chemical*, vol. 155, pp. 451–455, July 2011.

[79] T. O. Wehling, K. S. Novoselov, S. V. Morozov, E. E. Vdovin, M. I. Katsnelson, A. K. Geim, and A. I. Lichtenstein, "Molecular doping of graphene," *Nano Letters*, vol. 8, pp. 173–7, Jan. 2008.

[80] F. Yavari, C. Kritzinger, C. Gaire, L. Song, H. Gulapalli, T. Borca-Tasciuc, P. M. Ajayan, and N. Koratkar, "Tunable bandgap in graphene by the controlled adsorption of water molecules," *Small*, vol. 6, pp. 2535–8, Nov. 2010.

[81] G. Kalon, Y. J. Shin, and H. Yang, "Tunable metal–insulator transitions in bilayer graphene by thermal annealing," *Applied Physics Letters*, vol. 98, no. 23, p. 233108, 2011.

[82] R. Pearce, R. Yakimova, J. Eriksson, L. Hultman, M. Andersson, and A. Lloyd Spetz, "Development of FETs and Resistive Devices Based on Epitaxially Grown Single Layer Graphene on SiC for Highly Sensitive Gas Detection," *Materials Science Forum*, vol. 717-720, pp. 687–690, May 2012.

[83] A. C. Crowther, A. Ghassaei, N. Jung, and L. E. Brus, "Strong charge-transfer doping of 1 to 10 layer graphene by NO2," *ACS Nano*, vol. 6, pp. 1865–75, Feb. 2012.

[84] T. L. Burnett, J. Patten, and O. Kazakova, "Water desorption and re-adsorption on epitaxial graphene studied by SPM," *ArXiv*, p. 20, Apr. 2012.

[85] "www.cree.com," 2011.

[86] C. Mapelli, C. Castiglioni, G. Zerbi, and K. Müllen, "Common force field for graphite and polycyclic aromatic hydrocarbons," *Physical Review B*, vol. 60, pp. 12710–12725, Nov. 1999.

[87] L. Malard, M. Pimenta, G. Dresselhaus, and M. Dresselhaus, "Raman spectroscopy in graphene," *Physics Reports*, vol. 473, pp. 51–87, Apr. 2009.

[88] S. Shivaraman, R. A. Barton, X. Yu, J. Alden, L. Herman, M. Chandrashekhar, J. Park, P. L. McEuen, J. M. Parpia, H. G. Craighead, and M. G. Spencer, "Free-standing epitaxial graphene," *Nano Letters*, vol. 9, pp. 3100–5, Sept. 2009.

[89] S. Berciaud, S. Ryu, L. E. Brus, and T. F. Heinz, "Probing the intrinsic properties of exfoliated graphene: Raman spectroscopy of free-standing monolayers," *Nano Letters*, vol. 9, pp. 346–52, Jan. 2009.

[90] Z. Luo, C. Cong, J. Zhang, Q. Xiong, and T. Yu, "Direct observation of inner and outer G band double-resonance Raman scattering in free standing graphene," *Applied Physics Letters*, vol. 100, no. 24, p. 243107, 2012.

[91] Y. Y. Wang, Z. H. Ni, T. Yu, Z. X. Shen, H. M. Wang, Y. H. Wu, W. Chen, and A. T. Shen Wee, "Raman Studies of Monolayer Graphene: The Substrate Effect," *Journal of Physical Chemistry C*, vol. 112, pp. 10637–10640, July 2008.

[92] D. S. Lee, C. Riedl, B. Krauss, K. von Klitzing, U. Starke, and J. H. Smet, "Raman spectra of epitaxial graphene on SiC and of epitaxial graphene transferred to SiO2," *Nano Letters*, vol. 8, pp. 4320–5, Dec. 2008.

[93] A. C. Ferrari, J. C. Meyer, V. Scardaci, C. Casiraghi, M. Lazzeri, F. Mauri, S. Piscanec, D. Jiang, K. S. Novoselov, S. Roth, and A. K. Geim, "Raman Spectrum of Graphene and Graphene Layers," *Physical Review Letters*, vol. 97, pp. 1–4, Oct. 2006.

[94] R. Podila, R. Rao, R. Tsuchikawa, M. Ishigami, and A. M. Rao, "Raman spectroscopy of folded and scrolled graphene," *ACS Nano*, vol. 6, pp. 5784–90, July 2012.

[95] A. Tiberj, N. Camara, P. Godignon, and J. Camassel, "Micro-Raman and micro-transmission imaging of epitaxial graphene grown on the Si and C faces of 6H-SiC," *Nanoscale Research Letters*, vol. 6, p. 478, Jan. 2011.

[96] J. Rohrl, M. Hundhausen, K. V. Emtsev, T. Seyller, R. Graupner, and L. Ley, "Raman spectra of epitaxial graphene on SiC(0001)," *Applied Physics Letters*, vol. 92, no. 20, p. 201918, 2008.

[97] C.-C. Tang, M.-Y. Li, L. J. Li, C. C. Chi, and J. C. Chen, "Characteristics of a sensitive micro-Hall probe fabricated on chemical vapor deposited graphene over

the temperature range from liquid-helium to room temperature," *Applied Physics Letters*, vol. 99, no. 11, p. 112107, 2011.

[98] D. Choudhury, B. Das, D. Sarma, and C. Rao, "XPS evidence for molecular charge-transfer doping of graphene," *Chemical Physics Letters*, vol. 497, pp. 66–69, Sept. 2010.

[99] M. Bruna and S. Borini, "Raman signature of electron-electron correlation in chemically doped few-layer graphene," *Physical Review B*, vol. 83, p. 241401, June 2011.

[100] R. Lv, Q. Li, A. R. Botello-Méndez, T. Hayashi, B. Wang, A. Berkdemir, Q. Hao, A. L. Elías, R. Cruz-Silva, H. R. Gutiérrez, Y. A. Kim, H. Muramatsu, J. Zhu, M. Endo, H. Terrones, J.-C. Charlier, M. Pan, and M. Terrones, "Nitrogen-doped graphene: beyond single substitution and enhanced molecular sensing," *Scientific Reports*, vol. 2, p. 586, Jan. 2012.

[101] A. Das, S. Pisana, B. Chakraborty, S. Piscanec, S. K. Saha, U. V. Waghmare, K. S. Novoselov, H. R. Krishnamurthy, A. K. Geim, A. C. Ferrari, and A. K. Sood, "Monitoring dopants by Raman scattering in an electrochemically top-gated graphene transistor," *Nature Nanotechnology*, vol. 3, pp. 210–5, Apr. 2008.

[102] C. P. Puls, N. E. Staley, J.-S. Moon, J. A. Robinson, P. M. Campbell, J. L. Tedesco, R. L. Myers-Ward, C. R. Eddy, D. K. Gaskill, and Y. Liu, "Top-gate dielectric induced doping and scattering of charge carriers in epitaxial graphene," *Applied Physics Letters*, vol. 99, no. 1, p. 013103, 2011.

[103] M. Lazzeri, C. Attaccalite, L. Wirtz, and F. Mauri, "Impact of the electron-electron correlation on phonon dispersion: Failure of LDA and GGA DFT functionals in graphene and graphite," *Physical Review B*, vol. 78, pp. 8–11, Aug. 2008.

[104] F. Tuinstra, "Raman Spectrum of Graphite," *The Journal of Chemical Physics*, vol. 53, no. 3, p. 1126, 1970.

[105] S. Kopylov, A. Tzalenchuk, S. Kubatkin, and V. I. Fal'ko, "Charge transfer between epitaxial graphene and silicon carbide," *Applied Physics Letters*, vol. 97, no. 11, p. 112109, 2010.

[106] C. Berger, Z. Song, X. Li, X. Wu, N. Brown, C. Naud, D. Mayou, T. Li, J. Hass, A. N. Marchenkov, E. H. Conrad, P. N. First, and W. A. de Heer, "Electronic confinement and coherence in patterned epitaxial graphene," *Science*, vol. 312, pp. 1191–6, May 2006.

[107] C. Faugeras, A. Nerriere, M. Potemski, A. Mahmood, E. Dujardin, C. Berger, and W. A. de Heer, "Few-layer graphene on SiC, pyrolitic graphite, and graphene: A Raman scattering study," *Applied Physics Letters*, vol. 92, no. 1, p. 011914, 2008.

[108] J. Burton, L. Sun, F. Long, Z. Feng, and I. Ferguson, "First- and second-order Raman scattering from semi-insulating 4H-SiC," *Physical Review B*, vol. 59, pp. 7282–7284, Mar. 1999.

[109] F. Fromm, M. H. Oliveira Jr, A. Molina-Sánchez, M. Hundhausen, J. M. J. Lopes, H. Riechert, L. Wirtz, and T. Seyller, "Contribution of the buffer layer to the Raman spectrum of epitaxial graphene on SiC(0001)," *New Journal of Physics*, vol. 15, p. 043031, Apr. 2013.

[110] D. Graf, F. Molitor, K. Ensslin, C. Stampfer, A. Jungen, C. Hierold, and L. Wirtz, "Spatially resolved Raman spectroscopy of single- and few-layer graphene," *Nano Letters*, vol. 7, pp. 238–42, Feb. 2007.

[111] J. A. Robinson, C. P. Puls, N. E. Staley, J. P. Stitt, and M. A. Fanton, "Raman topography and strain uniformity of large-area epitaxial graphene," *Nano Letters*, vol. 9, pp. 964–8, Mar. 2009.

[112] J. A. Robinson, M. Wetherington, J. L. Tedesco, P. M. Campbell, X. Weng, J. Stitt, M. A. Fanton, E. Frantz, D. Snyder, B. L. VanMil, G. G. Jernigan, R. L. Myers-Ward, C. R. Eddy, and D. K. Gaskill, "Correlating Raman spectral signatures with carrier mobility in epitaxial graphene: a guide to achieving high mobility on the wafer scale," *Nano Letters*, vol. 9, pp. 2873–6, Aug. 2009.

[113] Q. Yu, L. A. Jauregui, W. Wu, R. Colby, J. Tian, Z. Su, H. Cao, Z. Liu, D. Pandey, D. Wei, T. F. Chung, P. Peng, N. P. Guisinger, E. A. Stach, J. Bao, S.-S. Pei, and Y. P. Chen, "Control and characterization of individual grains and grain boundaries in graphene grown by chemical vapour deposition," *Nature Materials*, vol. 10, pp. 443–9, June 2011.

[114] J. Shim, C. H. Lui, T. Y. Ko, Y.-J. Yu, P. Kim, T. F. Heinz, and S. Ryu, "Water-gated charge doping of graphene induced by mica substrates," *Nano Letters*, vol. 12, pp. 648–54, Feb. 2012.

[115] S. S. Datta, D. R. Strachan, E. J. Mele, and A. T. C. Johnson, "Surface potentials and layer charge distributions in few-layer graphene films," *Nano Letters*, vol. 9, pp. 7–11, Jan. 2009.

[116] N. J. Lee, J. W. Yoo, Y. J. Choi, C. J. Kang, D. Y. Jeon, D. C. Kim, S. Seo, and H. J. Chung, "The interlayer screening effect of graphene sheets investigated by Kelvin probe force microscopy," *Applied Physics Letters*, vol. 95, no. 22, p. 222107, 2009.

[117] M. R. Connolly and C. G. Smith, "Nanoanalysis of graphene layers using scanning probe techniques," *Philosophical transactions. Series A, Mathematical, physical, and engineering sciences*, vol. 368, pp. 5379–89, Dec. 2010.

[118] R. Jalilian, L. A. Jauregui, G. Lopez, J. Tian, C. Roecker, M. M. Yazdanpanah, R. W. Cohn, I. Jovanovic, and Y. P. Chen, "Scanning gate microscopy on graphene: charge inhomogeneity and extrinsic doping," *Nanotechnology*, vol. 22, p. 295705, July 2011.

[119] M. Syväjärvi and R. Yakimova, "Sublimation Epitaxial Growth of Hexagonal and Cubic SiC," *Comprehensive Semiconductor Science and Technology*, vol. 3, pp. 202–231, 2011.

[120] L. Yan, C. Punckt, I. A. Aksay, W. Mertin, and G. Bacher, "Local voltage drop in a single functionalized graphene sheet characterized by Kelvin probe force microscopy," *Nano Letters*, vol. 11, pp. 3543–9, Sept. 2011.

[121] A. E. Curtin, M. S. Fuhrer, J. L. Tedesco, R. L. Myers-Ward, C. R. Eddy, and D. K. Gaskill, "Kelvin probe microscopy and electronic transport in graphene on SiC(0001) in the minimum conductivity regime," *Applied Physics Letters*, vol. 98, no. 24, p. 243111, 2011.

[122] W. J. Liu, H. Y. Yu, S. H. Xu, Q. Zhang, X. Zou, J. L. Wang, K. L. Pey, J. Wei, H. L. Zhu, and M. F. Li, "Understanding Asymmetric Transportation Behavior in Graphene Field-Effect Transistors Using Scanning Kelvin Probe Microscopy," *IEEE Electron Device Letters*, vol. 32, pp. 128–130, Feb. 2011.

[123] R. Wang, S. Wang, D. Zhang, Z. Li, Y. Fang, and X. Qiu, "Control of carrier type and density in exfoliated graphene by interface engineering," *ACS Nano*, vol. 5, pp. 408–12, Jan. 2011.

[124] Y.-J. Yu, Y. Zhao, S. Ryu, L. E. Brus, K. S. Kim, and P. Kim, "Tuning the graphene work function by electric field effect," *Nano Letters*, vol. 9, pp. 3430–4, Oct. 2009.

[125] D. Ziegler, P. Gava, J. Güttinger, F. Molitor, L. Wirtz, M. Lazzeri, A. Saitta, A. Stemmer, F. Mauri, and C. Stampfer, "Variations in the work function of doped single- and few-layer graphene assessed by Kelvin probe force microscopy and density functional theory," *Physical Review B*, vol. 83, pp. 1–7, June 2011.

[126] W. Melitz, J. Shen, A. C. Kummel, and S. Lee, "Kelvin probe force microscopy and its application," *Surface Science Reports*, vol. 66, pp. 1–27, Jan. 2011.

[127] E. H. Hall, "On a New Action of the Magnet on Electric Currents," *American Journal of Mathematics*, vol. 2, pp. 287–292, Dec. 1979.

[128] P.-A. Besse, G. Boero, M. Demierre, V. Pott, and R. Popovic, "Detection of a single magnetic microbead using a miniaturized silicon Hall sensor," *Applied Physics Letters*, vol. 80, no. 22, p. 4199, 2002.

[129] R. Popovic, *Hall Effect Devices: Magnetic Sensors and Characterization of Semiconductors*. Adam Hilger, 1991.

[130] A. Tzalenchuk, S. Lara-Avila, K. Cedergren, M. Syväjärvi, R. Yakimova, O. Kazakova, T. Janssen, K. Moth-Poulsen, T. Bjø rnholm, S. Kopylov, V. Fal'ko, and S. Kubatkin, "Engineering and metrology of epitaxial graphene," *Solid State Communications*, vol. 151, pp. 1094–1099, June 2011.

[131] S. Lara-Avila, A. Tzalenchuk, S. Kubatkin, R. Yakimova, T. J. B. M. Janssen, K. Cedergren, T. Bergsten, and V. Fal'ko, "Disordered Fermi Liquid in Epitaxial Graphene from Quantum Transport Measurements," *Physical Review Letters*, vol. 107, p. 166602, Oct. 2011.

[132] E. Hwang and S. Das Sarma, "Acoustic phonon scattering limited carrier mobility in two-dimensional extrinsic graphene," *Physical Review B*, vol. 77, p. 115449, Mar. 2008.

[133] W. Zhu, V. Perebeinos, M. Freitag, and P. Avouris, "Carrier scattering, mobilities, and electrostatic potential in monolayer, bilayer, and trilayer graphene," *Physical Review B*, vol. 80, p. 235402, Dec. 2009.

[134] T. R. Garcia, A. Kumar, B. Reinke, T. E. Blue, and W. Windl, "Electron-hole pair generation in SiC high-temperature alpha particle detectors," *Applied Physics Letters*, vol. 103, no. 15, p. 152108, 2013.

[135] K. Vervaeke, E. Simoen, G. Borghs, and V. V. Moshchalkov, "Size dependence of microscopic Hall sensor detection limits," *The Review of scientific instruments*, vol. 80, p. 074701, July 2009.

[136] G. Liu, W. Stillman, S. Rumyantsev, Q. Shao, M. Shur, and A. A. Balandin, "Low-frequency electronic noise in the double-gate single-layer graphene transistors," *Applied Physics Letters*, vol. 95, no. 3, p. 033103, 2009.

[137] G. Xu, C. M. Torres, Y. Zhang, F. Liu, E. B. Song, M. Wang, Y. Zhou, C. Zeng, and K. L. Wang, "Effect of Spatial Charge Inhomogeneity on 1/ f Noise Behavior in Graphene," *Nano Letters*, p. 100804125201005, Aug. 2010.

[138] A. A. Balandin, "Low-frequency 1/f noise in graphene devices," *Nature Nanotechnology*, vol. 8, pp. 549–55, Aug. 2013.

[139] A. A. Kaverzin, A. S. Mayorov, A. Shytov, and D. W. Horsell, "Impurities as a source of 1/f noise in graphene," *Physical Review B*, vol. 85, p. 075435, Feb. 2012.

[140] D. Farmer, V. Perebeinos, Y.-M. Lin, C. Dimitrakopoulos, and P. Avouris, "Charge trapping and scattering in epitaxial graphene," *Physical Review B*, vol. 84, pp. 1–5, Nov. 2011.

[141] S. Rumyantsev, G. Liu, W. Stillman, V. Y. Kachorovskii, M. S. Shur, and A. A. Balandin, "Low-frequency noise in graphene field-effect transistors," in *2011 21st International Conference on Noise and Fluctuations*, pp. 234–237, IEEE, June 2011.

[142] O. Kazakova, V. Panchal, J. Gallop, P. See, D. C. Cox, M. Spasova, and L. F. Cohen, "Ultrasmall particle detection using a submicron Hall sensor," *Journal of Applied Physics*, vol. 107, no. 9, p. 09E708, 2010.

[143] L. Di Michele, C. Shelly, J. Gallop, and O. Kazakova, "Single particle detection: Phase control in submicron Hall sensors," *Journal of Applied Physics*, vol. 108, no. 10, p. 103918, 2010.

[144] L. Di Michele, C. Shelly, P. de Marco, P. See, D. Cox, and O. Kazakova, "Detection and susceptibility measurements of a single Dynal bead," *Journal of Applied Physics*, vol. 110, no. 6, p. 063916, 2011.

[145] D. G. Avery, D. W. Goodwin, W. D. Lawson, and T. S. Moss, "Optical and Photo-Electrical Properties of Indium Antimonide," *Proceedings of the Physical Society. Section B*, vol. 67, pp. 761–767, Oct. 1954.

[146] G. Landry, M. M. Miller, B. R. Bennett, M. Johnson, and V. Smolyaninova, "Characterization of single magnetic particles with InAs quantum-well Hall devices," *Applied Physics Letters*, vol. 85, no. 20, p. 4693, 2004.

[147] G. Mihajlovic, P. Xiong, S. von Molnar, K. Ohtani, H. Ohno, M. Field, and G. J. Sullivan, "Detection of single magnetic bead for biological applications using an InAs quantum-well micro-Hall sensor," *Applied Physics Letters*, vol. 87, no. 11, p. 112502, 2005.

[148] O. Florescu, M. Mattmann, and B. Boser, "Fully integrated detection of single magnetic beads in complementary metal-oxide-semiconductor," *Journal of Applied Physics*, vol. 103, no. 4, p. 046101, 2008.

[149] O. Kazakova, J. Gallop, P. See, D. Cox, G. Perkins, J. Moore, and L. Cohen, "Detection of a Micron-Sized Magnetic Particle Using InSb Hall Sensor," *IEEE Transactions on Magnetics*, vol. 45, pp. 4499–4502, Oct. 2009.

[150] A. M. Baker, J. Alexander-Webber, T. Altebaeumer, and R. Nicholas, "Energy relaxation for hot Dirac fermions in graphene and breakdown of the quantum Hall effect," *Physical Review B*, vol. 85, pp. 1–6, Mar. 2012.

[151] A. M. R. Baker, J. A. Alexander-Webber, T. Altebaeumer, S. D. McMullan, T. J. B. M. Janssen, A. Tzalenchuk, S. Lara-Avila, S. Kubatkin, R. Yakimova, C.-T. Lin, L.-J. Li, and R. J. Nicholas, "Energy loss rates of hot Dirac fermions in epitaxial, exfoliated, and CVD graphene," *Physical Review B*, vol. 87, p. 045414, Jan. 2013.

[152] S. Hertel, F. Kisslinger, J. Jobst, D. Waldmann, M. Krieger, and H. B. Weber, "Current annealing and electrical breakdown of epitaxial graphene," *Applied Physics Letters*, vol. 98, no. 21, p. 212109, 2011.

[153] "www.bruker.com," 2013.

[154] "www.brukerafmprobes.com," 2013.

[155] P. Girard, "Electrostatic force microscopy: principles and some applications to semiconductors," *Nanotechnology*, vol. 12, p. 485, 2001.

[156] R. A. Oliver, "Advances in AFM for the electrical characterization of semiconductors," *Reports on Progress in Physics*, vol. 71, p. 076501, July 2008.

[157] T. Burnett, R. Yakimova, and O. Kazakova, "Mapping of local electrical properties in epitaxial graphene using electrostatic force microscopy," *Nano Letters*, vol. 11, pp. 2324–8, June 2011.

[158] L. Guo, X. Zhao, Y. Bai, and L. Qiao, "Water adsorption behavior on metal surfaces and its influence on surface potential studied by in situ SPM," *Applied Surface Science*, vol. 258, pp. 9087–9091, Sept. 2012.

[159] M. Nonnenmacher, M. P. O'Boyle, and H. K. Wickramasinghe, "Kelvin probe force microscopy," *Applied Physics Letters*, vol. 58, no. 25, p. 2921, 1991.

[160] U. Zerweck, C. Loppacher, T. Otto, S. Grafström, and L. Eng, "Accuracy and resolution limits of Kelvin probe force microscopy," *Physical Review B*, vol. 71, p. 125424, Mar. 2005.

[161] A. Baumgartner, T. Ihn, K. Ensslin, G. Papp, F. Peeters, K. Maranowski, and A. Gossard, "Classical Hall effect in scanning gate experiments," *Physical Review B*, vol. 74, pp. 1–7, Oct. 2006.

[162] M. R. Connolly, K. L. Chiou, C. G. Smith, D. Anderson, G. A. C. Jones, A. Lombardo, A. Fasoli, and A. C. Ferrari, "Scanning gate microscopy of current-annealed single layer graphene," *Applied Physics Letters*, vol. 96, no. 11, p. 113501, 2010.

[163] E. Watanabe, A. Conwill, D. Tsuya, and Y. Koide, "Low contact resistance metals for graphene based devices," *Diamond and Related Materials*, vol. 24, pp. 171–174, Apr. 2012.

[164] C. Riedl, C. Coletti, T. Iwasaki, and U. Starke, "Hydrogen Intercalation below Epitaxial Graphene on SiC(0001)," *Materials Science Forum*, vol. 645-648, pp. 623–628, Apr. 2010.

[165] F. Schedin, A. K. Geim, S. V. Morozov, E. W. Hill, P. Blake, M. I. Katsnelson, and K. S. Novoselov, "Detection of individual gas molecules adsorbed on graphene," *Nature Materials*, vol. 6, pp. 652–655, July 2007.

[166] S. Zhou, D. Siegel, A. Fedorov, and A. Lanzara, "Metal to Insulator Transition in Epitaxial Graphene Induced by Molecular Doping," *Physical Review Letters*, vol. 101, p. 086402, Aug. 2008.

[167] H. J. Yoon, D. H. Jun, J. H. Yang, Z. Zhou, S. S. Yang, and M. M.-C. Cheng, "Carbon dioxide gas sensor using a graphene sheet," *Sensors and Actuators B: Chemical*, vol. 157, pp. 310–313, Sept. 2011.

[168] H. Zhou, P. Ganesh, V. Presser, M. Wander, P. Fenter, P. Kent, D.-e. Jiang, A. Chialvo, J. McDonough, K. Shuford, and Y. Gogotsi, "Understanding controls on interfacial wetting at epitaxial graphene: Experiment and theory," *Physical Review B*, vol. 85, p. 035406, Jan. 2012.

[169] M. G. Chung, D. H. Kim, H. M. Lee, T. Kim, J. H. Choi, D. kyun Seo, J.-B. Yoo, S.-H. Hong, T. J. Kang, and Y. H. Kim, "Highly sensitive NO2 gas sensor based on ozone treated graphene," *Sensors and Actuators B: Chemical*, vol. 166-167, pp. 172–176, May 2012.

[170] H. Sojoudi, J. Baltazar, C. Henderson, and S. Graham, "Impact of post-growth thermal annealing and environmental exposure on the unintentional doping of CVD graphene films," *Journal of Vacuum Science & Technology B: Microelectronics and Nanometer Structures*, vol. 30, no. 4, p. 041213, 2012.

[171] E. Llobet, "Gas sensors using carbon nanomaterials: A review," *Sensors and Actuators B: Chemical*, vol. 179, pp. 32–45, Mar. 2013.

[172] K. Okudaira, E. Morikawa, S. Hasegawa, P. Sprunger, V. Saile, K. Seki, Y. Harada, and N. Ueno, "Radiation damage of poly(methylmethacrylate) thin films analyzed by UPS," *Journal of Electron Spectroscopy and Related Phenomena*, vol. 88-91, pp. 913–917, Mar. 1998.

[173] S. Lara-Avila, K. Moth-Poulsen, R. Yakimova, T. Bjø rnholm, V. Fal'ko, A. Tzalenchuk, and S. Kubatkin, "Non-volatile photochemical gating of an epitaxial graphene/polymer heterostructure," *Advanced Materials*, vol. 23, pp. 878–82, Feb. 2011.

[174] H. Ikeura-Sekiguchi, T. Sekiguchi, and M. Koike, "Characterization and degradation of ZEP520 resist film by TOF-PSID and NEXAFS," *Journal of Electron Spectroscopy and Related Phenomena*, vol. 144-147, pp. 453–455, June 2005.

[175] B. K. Bussmann, O. Ochedowski, and M. Schleberger, "Doping of graphene exfoliated on SrTiO3," *Nanotechnology*, vol. 22, p. 265703, July 2011.

[176] R. Pearce, J. Eriksson, T. Iakimov, L. Hultman, A. Lloyd Spetz, and R. Yakimova, "On the differing sensitivity to chemical gating of single and double layer epitaxial graphene explored using scanning Kelvin probe microscopy," *ACS Nano*, vol. 7, pp. 4647–56, May 2013.

[177] "ISO/TR 19319:2013. Surface chemical analysis – Fundamental approaches to determination of lateral resolution and sharpness in beam-based methods," tech. rep.

[178] E. J. H. Lee, K. Balasubramanian, R. T. Weitz, M. Burghard, and K. Kern, "Contact and edge effects in graphene devices," *Nature Nanotechnology*, vol. 3, pp. 486–90, Aug. 2008.

[179] J. Karch, C. Drexler, P. Olbrich, M. Fehrenbacher, M. Hirmer, M. M. Glazov, S. A. Tarasenko, E. L. Ivchenko, B. Birkner, J. Eroms, D. Weiss, R. Yakimova, S. Lara-Avila, S. Kubatkin, M. Ostler, T. Seyller, and S. D. Ganichev, "Terahertz Radiation Driven Chiral Edge Currents in Graphene," *Physical Review Letters*, vol. 107, p. 276601, Dec. 2011.

[180] M. Burghard, H. Klauk, and K. Kern, "Carbon-Based Field-Effect Transistors for Nanoelectronics," *Advanced Materials*, vol. 21, pp. 2586–2600, July 2009.

[181] C. Casiraghi, A. Hartschuh, H. Qian, S. Piscanec, C. Georgi, A. Fasoli, K. S. Novoselov, D. M. Basko, and A. C. Ferrari, "Raman spectroscopy of graphene edges," *Nano Letters*, vol. 9, pp. 1433–41, Apr. 2009.

[182] S. Heydrich, M. Hirmer, C. Preis, T. Korn, J. Eroms, D. Weiss, and C. Schuller, "Scanning Raman spectroscopy of graphene antidot lattices: Evidence for systematic p-type doping," *Applied Physics Letters*, vol. 97, no. 4, p. 043113, 2010.

[183] B. Huang, Z. Li, Z. Liu, G. Zhou, S. Hao, J. Wu, B.-L. Gu, and W. Duan, "Adsorption of Gas Molecules on Graphene Nanoribbons and Its Implication for Nanoscale

Molecule Sensor," *Journal of Physical Chemistry C*, vol. 112, pp. 13442–13446, Sept. 2008.

[184] J. Berashevich and T. Chakraborty, "Doping graphene by adsorption of polar molecules at the oxidized zigzag edges," *Physical Review B*, vol. 81, p. 205431, May 2010.

[185] Y. Ouyang, S. Sanvito, and J. Guo, "Effects of edge chemistry doping on graphene nanoribbon mobility," in *68th Device Research Conference*, pp. 217–218, IEEE, June 2010.

[186] C. Cao, L. Chen, W. Huang, and H. Xu, "Electronic Transport of Zigzag Graphene Nanoribbons with Edge Hydrogenation and Oxidation," *The Open Chemical Physics Journal*, vol. 4, pp. 1–7, Feb. 2012.

[187] N. Pascher, D. Bischoff, T. Ihn, and K. Ensslin, "Scanning gate microscopy on a graphene nanoribbon," *Applied Physics Letters*, vol. 101, no. 6, p. 063101, 2012.

[188] J. Chae, S. Jung, S. Woo, H. Baek, J. Ha, Y. J. Song, Y.-W. Son, N. B. Zhitenev, J. A. Stroscio, and Y. Kuk, "Enhanced carrier transport along edges of graphene devices," *Nano Letters*, vol. 12, pp. 1839–44, Apr. 2012.

[189] A. G. F. Garcia, M. König, D. Goldhaber-Gordon, and K. Todd, "Scanning gate microscopy of localized states in wide graphene constrictions," *Physical Review B*, vol. 87, p. 085446, Feb. 2013.

[190] L. Yan, W. Wang, T. Wan, Q. Guo, K. Sheng, and B. Yu, "The tunable bandgap of AB-stacking bilayer graphene under the applied electric fields for power devices," *2011 2nd International Conference on Artificial Intelligence, Management Science and Electronic Commerce (AIMSEC)*, pp. 6040–6043, Aug. 2011.

[191] X. Li, X. Wu, M. Sprinkle, F. Ming, M. Ruan, Y. Hu, C. Berger, and W. A. de Heer, "Top- and side-gated epitaxial graphene field effect transistors," *Physica Status Solidi (a)*, vol. 207, pp. 286–290, Feb. 2010.

[192] J. F. Tian, L. A. Jauregui, G. Lopez, H. Cao, and Y. P. Chen, "Ambipolar graphene field effect transistors by local metal side gates," *Applied Physics Letters*, vol. 96, no. 26, p. 263110, 2010.

[193] C.-T. Chen, T. Low, H.-y. Chiu, and W. Zhu, "Graphene-Side-Gate Engineering," *IEEE Electron Device Letters*, vol. 33, pp. 330–332, Mar. 2012.

[194] B. Hahnlein, B. Handel, J. Pezoldt, H. Topfer, R. Granzner, and F. Schwierz, "Side-gate graphene field-effect transistors with high transconductance," *Applied Physics Letters*, vol. 101, no. 9, p. 093504, 2012.

[195] E. V. Castro, K. S. Novoselov, S. V. Morozov, N. M. R. Peres, J. M. B. Lopes dos Santos, J. Nilsson, F. Guinea, a. K. Geim, and a. H. Castro Neto, "Electronic properties of a biased graphene bilayer," *Journal of Physics: Condensed Matter*, vol. 22, p. 175503, May 2010.

[196] L. Folks, A. S. Troup, T. D. Boone, J. A. Katine, M. Nishioka, M. Grobis, G. J. Sullivan, A. Ikhlassi, M. Field, and B. A. Gurney, "Near-surface nanoscale InAs Hall cross sensitivity to localized magnetic and electric fields," *Journal of physics. Condensed matter : an Institute of Physics journal*, vol. 21, p. 255802, June 2009.

[197] S. Liu, H. Guillou, A. D. Kent, G. W. Stupian, and M. S. Leung, "Effect of probe geometry on the Hall response in an inhomogeneous magnetic field: A numerical study," *Journal of Applied Physics*, vol. 83, no. 11, p. 6161, 1998.

[198] R. Yakimova, T. Iakimova, and M. Syväjärvi, "Process for growth of graphene: Patent PCT/SE2011/050328," 2012.

[199] G. Mihajlovic, K. Aledealat, P. Xiong, S. von Molnar, M. Field, and G. J. Sullivan, "Magnetic characterization of a single superparamagnetic bead by phase-sensitive micro-Hall magnetometry," *Applied Physics Letters*, vol. 91, no. 17, p. 172518, 2007.

[200] A. M. Goossens, V. E. Calado, A. Barreiro, K. Watanabe, T. Taniguchi, and L. M. K. Vandersypen, "Mechanical cleaning of graphene," *Applied Physics Letters*, vol. 100, no. 7, p. 073110, 2012.

A role model is someone you look up to and hope to someday be just like. As the first person in my family to achieve this high accolade, Vishy, you are my role model. You have made me so proud to be known as your little sister and melon. I hope I can walk in your footsteps and achieve something this great. Congratulations on your Ph.D. I love you.

- Janki Mistry